Multiple scales modeling of solidification grain structures and segregation in metallic alloys

Salem Mosbah

Ecole Doctorale 364 : Sciences Fondamentales et Appliquées

N° attribué par la bibliothèque
|__|__|__|__|__|__|__|__|__|__|

T H E S E

pour obtenir le grade de

DOCTEUR DE L'ECOLE NATIONALE SUPERIEURE DES MINES DE PARIS

Spécialité «Sciences et Génie des Matériaux»

Présentée et soutenue publiquement par

Salem MOSBAH

le 17 Décembre 2008

MULTIPLE SCALES MODELING OF SOLIDIFICATION GRAIN STRUCTURES AND SEGREGATION IN METALLIC ALLOYS

Jury :

Prof.	Eric ARQUIS	Rapporteur
Prof.	Yves FAUTRELLE	Rapporteur
Prof.	Dieter HERLACH	Examinateur
Prof.	Gérard LESOULT	Examinateur
Dr	Daniela VOSS	Examinatrice
Dr	Charles-André GANDIN	Examinateur Directeur de thèse
Dr	Michel BELLET	Examinateur Co-Directeur de thèse

IN THE MEMORY OF MY GRAND PARENTS,
TO MY PARENTS,
TO MY SISTERS AND BROTHERS,
AND TO MY LOVELY WIFE

Acknowledgments

Firstly, I would like to express my gratitude to my PhD supervisors, Dr Charles-André Gandin and Dr Michel Bellet for their support and guidance during the three years of my thesis. Their availabilities, experiences and deep knowledge of the solidification and numerical modeling fields were of great help for the achievements that have been made.

I am also very grateful to Prof. Yves Fautrelle and Prof. Eric Arquis for reviewing this manuscript, as well as for Prof. Dieter Herlach and Prof. Gérard Lesoult who have accepted to be part of board of examiner.

I express a lot of thanks to all the CEMEF technical staff, especially Mrs. Suzanne Jacomet, Mrs. Monique Repoux and Mr Bernard Triger for their valuable help to process and realize all the EBSD and SEM measurements. Many thanks also to the CEMEF administrative staff and especially to Mr Patrick Coels for his support and help.

I would like to thank the SP2 and TMP research teams, Damien Tourret, Jérôme Blaizot, Steven Chang, Brendan Crozier, and especially Dr Boussad Amarouchene for his important help.

Contents

General Introduction

Most industrial material processing routes involve a liquid to solid phase transformation step. During this transformation, all components are melted and the liquid system is then cooled with a controlled or non controlled cooling rate to obtain the final solid structure. Casting and continuous casting are the most used techniques due to their low-cost and high-volume production of metals and alloys. When the melt solidifies, it freezes unstably due to the deviation from the equilibrium conditions, resulting in a branched structure. These forms are known as dendritic structures and form solid grains with given orientations. The grain sizes, shapes, and how they interact with each other are controlled by the solidification conditions. Elongated grains are usually observed near the mould wall where heat is extracted through the wall, this structure is known as columnar structure. Contrarily, finest grains structures are observed in the internal volume of a typical casting ingot. This structure, characterized by homogenous shape mainly due to a free growth in the all possible directions, is known as equiaxed structure. In addition, deviations from the nominal composition of the system are usually measured in the final as-cast product. The segregation patterns as well as the grains characteristics largely determine the properties of the material. Additionally, thermal or mechanical steps are usually applied to obtain the final products. However, the grain structures are mainly controlled during the solidification step and are highly coupled with the solute distribution field.

Important researches have been conducted in the recent years to increase our knowledge of the metallurgical aspects of the solidification in metallic alloys [Soh97]. Experimental models have been developed to study solidification of metallic alloys at different length scales. Currently, it is well established that the growth of the dendritic structure in metallic alloys is highly dependent on the solute and thermal fields ahead the solid-liquid interface [Kur98]. In addition, the solid-liquid interface deviates from the equilibrium regular planar interface due to the surface tension as well as the solute and thermal variations. These aspects occurring at the scale of the dendritic branches distances are also coupled with the heat and fluid flow described at the cast product scale, referred to as the macro-scale. The final structure and segregation in the solid materials are highly dependent on the deviation magnitude from the equilibrium during the phase transformation. Jointly, due to the complexity of the solidification phenomena, numerical modeling of the solidification in metallic alloys has received great interest [Beck02, Rap89].

This work is part of project entitled the Non-Equilibrium Solidification, Modeling for Microstructure Engineering of Industrial Alloys (NEQUISOL), funded by the European Space Agency, ESA, in the framework of the activity Human Spaceflight. The aim of this research project is to understand the solidification in aluminum (Al) and/or nickel (Ni) based metallic alloys systems under non equilibrium conditions. The considered systems are of the order of magnitude of atomized droplets processed by typical industrial atomization processes, i.e. with typical radius from 200 to 2000 μm. These researches involve experimental and numerical modeling of physical phenomena at the micro (solid-liquid interface), the meso (grain scale) and the macro scales

(several grains). It also includes the study of the micro- and macro-segregation and phases volume fraction in the as-cast state as function of the deviation magnitude from the equilibrium solidification conditions. In this works, we focus on the aluminum copper, Al-Cu, spherical droplets produced upon ElectroMagnetic Levitation condition using the EML facility developed by the German Aerospace Center, DLR, [Herl04, Herl93]. Three copper compositions have been selected, 4, 14 and 24 wt%. For each composition, spontaneous and initiated nucleation have been achieved, with a given undercooling, leading to a total of six samples. We have conducted chemical characterization and SEM images processing of the Al–Cu samples solidified upon EML conditions to form a complete set of data. These data consist in maps of the copper and eutectic fraction together with dendrite arm spacing. *In-situ* temperature measurements during the solidification of the levitated droplets have also been integrated to give access to the key parameter for further modeling.

This report presents a summary of the main thesis achievements divided in four chapters. The first chapter is published in Acta Materialia, and chapters III and IV are being submitted to journals. In addition, a bibliography overview chapter and appendixes are supplied respectively to introduce the physical phenomena and to give more details about the key formulations presented in each article. The following describes the purpose and the contents of each chapter:

In the first part, a review of the main physical phenomena describing the solidification in metallic alloys is presented. Important effects occurring at the ingot scale, known as the macro-scale, are first analyzed. Similarly, thermodynamic aspects of the metallic alloys solidification are presented as well as observed final structure in as-solidified state. Subsequently, nucleation, growth, solute redistribution and the solid structures species interactions with the surrounding bulk are analyzed based on the available work in the literature. In the last part of this first section, we give a brief overview of previous experimental and numerical models dealing with the solidification microstructures, solute redistribution (segregation) and phase's evolution. In addition, a review of the available containerless experimental techniques is presented and we focus on the EML technique developed by Herlach et al. [Herl93] used in this contribution. Different approaches to predict the solidification grain structure, its interaction as well as coupling schemes between the macro and the micro scales have been investigated. Advantages and limitations of each model are presented together with the objectives of the present work with a focus on the coupled Cellular Automaton–Finite Element (CAFE) model.

The second chapter presents the experimental and numerical results that were obtained for the spherical Al–4, 14, and 24wt%Cu alloy systems solidified with spontaneous nucleation. The used EML experimental model to process the samples and the experimental measurements over the solidified samples are presented. Detailed description of a new developed multiphase multiscale model involving the nucleation undercooling of the primary dendritic, the eutectic structures and the growth kinetics are then given. *In-situ* measurements are also presented and analyzed. In addition, a summary of the results consisting of the temperature curves, the undercooling measured prior to the

nucleation of the primary and the eutectic structures, the copper average composition, the eutectic volume fraction and the dendrite arm spacing maps (as well as their averaged values over a cutting plane of the sample) are discussed. A parametric study of the model predictions as function of the primary, the secondary eutectic structure nucleation undercooling and solute back diffusion in the solid phase is given leading to the conclusion on the important effect of the eutectic structure growth and recalescence on the final phase's volume fractions.

The third part is dedicated to the experimental results obtained using the EML technique over the Al–4, 14 and 24 wt%Cu droplets when the nucleation of the primary phase has been initiated using an alumina plate. The experimental setup is briefly presented as well as the measurement procedure. Then a development of a new Cellular Automaton (CA) – Finite Element (FE) model together with a new coupling scheme between are presented in details. Next, extensive comparisons are achieved between the new CAFE model together with the analytical model developed by Wang and Beckermann [Wang93.1, Wang93.2] and the Heringer et al. [Her06] models. These works are chosen to show the model capabilities and as a validation of the achieved developments. Moreover, detailed descriptions of the experimental data consisting in the average, over a cutting diametric plane for each sample, of the copper composition, the eutectic volume fraction and the dendrite arm spacing are given. In addition, the measured temperature curves and the copper composition, the eutectic volume fraction and the dendrite arm spacing maps are presented and discussed. In the same result sections, the presented new CAFE model is applied to simulate the solidification of the Al-Cu samples. The model predictions are analyzed and compared to the experimental results for the temperature curves, the copper average composition and the eutectic volume fraction maps.

In chapter four, we firstly give an overview of the horizontal solidification setup developed by Wang et al. [Wang06] and the experimental procedure used to process a rectangular Sn-10wt%Pb sample is explained. Detailed description of the Finite Element, FE, model is then presented taking into account the thermal and the solutal buoyancy forces. The model solves the energy and the solute conservation equations with a refined triangular mesh. Complete description of the used mesh adaptation technique is presented. The FE model is then coupled with the Cellular Automaton model presented earlier in chapter III and the new coupled CAFE model is applied for the Sn-10wt%Pb solidification experiment. In the results section, both the experimental and numerical data are presented and compared.

Finally, after a summary of the achievements, directions are given for further improvements of the Cellular Automaton–Finite Element model with the objective to simulate grains structures and segregation in casting.

Résumé en Français :

Chapitre I Bibliography review

Ce travail a été mené dans le cadre du projet européen 'Non-Equilibrium Solidification, Modeling for Microstructure Engineering of Industrial Alloys' (Nequisol) financé par l'agence spatiale européenne (ESA). Les motivations ainsi que les objectifs de ce travail sont exposés dans l'introduction générale ci dessus.

Ce premier chapitre présente les principes fondamentaux de la solidification pour les alliages métalliques. Les paramètres thermodynamiques contrôlant la solidification à l'échelle du procédé de fonderie sont d'abord présentés. La structure dendritique des grains ainsi que les transferts thermiques et chimiques devant l'interface solide/liquide sont ensuite exposés. La germination, la croissance, la redistribution du soluté et l'interaction entre les structures de grains et le liquide extra-dendritique sont aussi brièvement décrits.

D'autre part, un aperçu des récents modèles expérimentaux et numériques pour l'étude des structures de grains de solidification, redistribution du soluté (ségrégation) et l'évolution des fractions de phases est exposé. Ensuite, les récents modèles expérimentaux de solidification sans contact pour l'étude de la germination et la croissance des structures équiaxes sont rapportés. En particulier, le procèdé de solidification par lévitation électromagnétique (utilisé comme modèle expérimental dans le cadre de cette étude) est décrit.

Enfin, différentes approches de modélisation à l'échelle des structures de grains et à l'échelle du procédé sont présentées. Leurs limitations et leurs avantages sont détaillés et en particulier les modèles couplant élément fini–automate cellulaire.

Chapter I Bibliography review

I.1 Liquid to solid phase transformations in metallic alloys

As the main step (such as casting, continuous casting, etc.), or part of an industrial process, solidification plays an important role on the final product structure as well as on its mechanical and chemical properties. Understanding the solidification of metallic alloys is required to optimize and build industrial solidification processes. In this chapter, we give an overview of the main steps describing the phase transformation in metallic alloy from the liquid state to the solid state. We will focus on binary alloy system which is from the physical point of view most suitable for further modeling. A linear phase diagram will be assumed to avoid any complexity arising from the change of the liquidus slope, m_L , and the solute partition ratio, k, as a function of the melt composition [Kur98]. Thermodynamic aspects of the solidification at typical casting scale will be first analyzed and observed final microstructure in as–solidified state will be also presented. In addition, nucleation, growth, solute redistribution and the primary and the eutectic structures species interaction with the surrounding melt will be presented based on the available work in the literature. In the last part of this section, we present a brief overview of previous experimental and numerical work dealing with the solidification microstructure and solute redistribution.

I.1.1 Thermodynamics aspects of solidification in metallic alloys

The decrease of the free energy is the driving force of the transformation of a given metallic system from the melt to the solid state. The free energy changes mainly due the heat extraction (i.e. cooling of the system) and the transformation from the liquid to the solid phase (i.e. latent heat release). The phase diagram, for a given constant pressure, shows the equilibrium conditions between the thermodynamically distinct liquid and solid phases. It gives a simple way to understand liquid to solid phase transformation. A typical binary alloy phase diagram is illustrated in Figure 1 where a linearized diagram is superimposed and used in the following analysis. The *liquidus* $T_L(w)$ red lines, give for a given composition the temperature at which no solid phase remains and the liquid phase is most stable than the coexistence of the two solid and liquid phases. In reality, a metallic alloy system, with a composition w_0, might remains at the melt state for several degrees below the equilibrium temperature, $T_L(w_0)$, given by the phase diagram [Kur98]. This is called the *undercooling* and calculated as $\Delta T_n^{\alpha} = T_L - T$. The *solidus* $T_S(w)$, blue lines, define the range of temperature and composition where only the solid phase is thermodynamically stable. For binary metallic alloys, it is generally observed (for a given composition at the last stage of the solidification) that the last liquid phase solidifies by forming the *eutectic structure* composed by two solid phases, $\alpha + \theta$. This is defined as the *eutectic transformation*. The temperature at which this transformation occurs is known as the *eutectic temperature*, T_E, and similarly the composition is denoted the *eutectic composition*, w_E. The phase diagram predicts that this transformation occurs at a constant temperature equal to the eutectic temperature. However, several experiments and models show that this transformation occurs below the equilibrium temperature [Kur98, Herl93]. As a consequence, both the primary, α, and the eutectic, $\alpha + \theta$, structures start to form at non

equilibrium conditions and the phase diagram becomes incoherent with regard to such transformation.

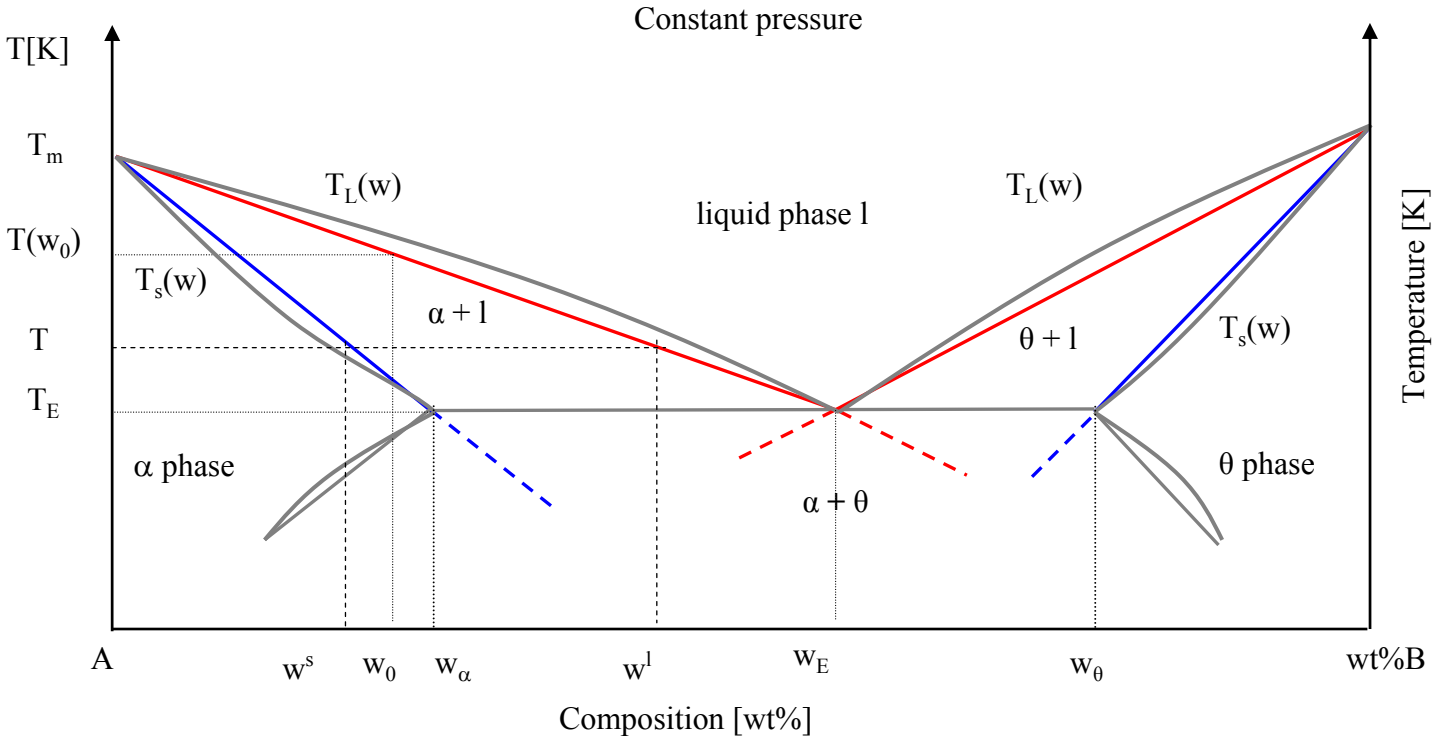

Figure 1: Phase diagram of a typical binary alloy A-B system, grey lines, and the corresponding linearized theoretical phase diagram, red and blues lines. For a given temperature below the liquidus temperature, T_L , for an alloy with composition, w_0, two distinct phases coexist where the liquid phase composition, at the solid-liquid interface, is given by the liquidus line and equal to $w^{l/s}$ and the solid phase composition, at the s/l interface, is equal to $w^{s/l}$. The dashed lines correspond to the liquidus and solidus lines interpolated and used to study the transformation of the liquid phase a solid phase below the equilibrium eutectic temperature, T_E

Figure 2 is a schematic view through a typical casting process, with a total surface A and volume V. The system is initially filled with a binary metallic alloy in the melt state with a composition, w_0, at a given temperature, T_0, greater than the melting temperature identified as the liquidus temperature, T_L, on the phase diagram. Due to heat extraction from the mould walls, the average temperature of the system decreases and solidification starts with a given undercooling. Three zones could be identified, the solid zone, s, the mushy zone composed of a mixture of liquid and solid phases, s+l, and finally a fully liquid zone, l. In addition, as highlighted in the top of the system, figure 1, due to the difference between the liquid and the solid phase densities, shrinkage is observed (which is measured in most casting processes of metallic alloys system).

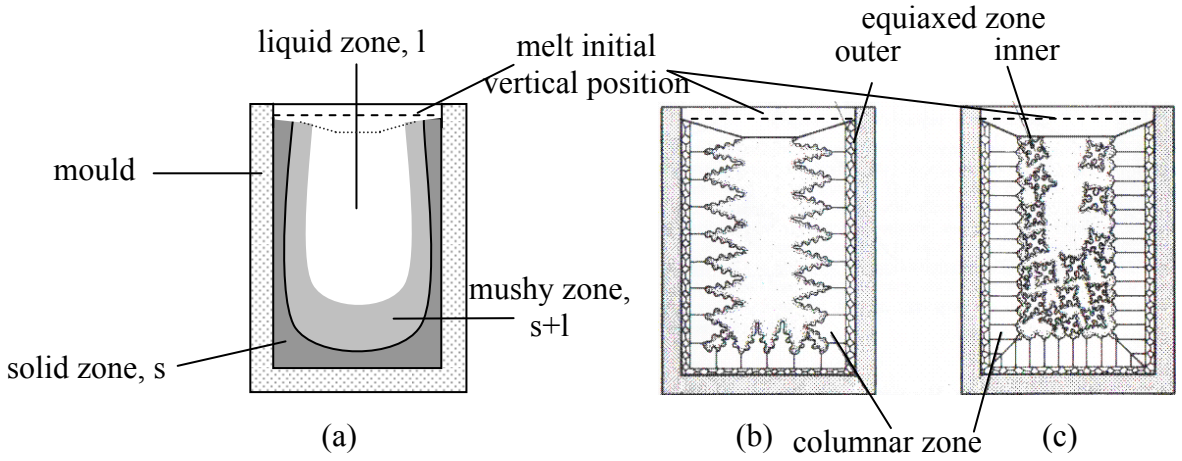

Figure 2: a) Macro view of a transverse section of a typical casting process where the mould and the ingot are drawn. Three zones could be defined, the fully liquid zone, l, the mixed solid and liquid zone, the mushy zone l+s, and finally the solid zone, s. b) The upper dashed lines designate the initial vertical melt position to identify the shrinkage of the ingot/air interface due to the difference between the liquid and solid densities. At the beginning of the solidification, nuclei appear in liquid zone in contact with the mould wall and increase in size to define the outer zone that is generally a very fine structure. The dendritic structures that are most parallel to the temperature gradient will continue to grow inward from the mould wall to form the columnar grains. c) After a certain period of time, due to some branch detachments from the elongated dendritic structure and/or some nucleating particles, solid crystals will grow in the undercooled melt in front of the growing columnar structure. The solidification region containing these equiaxed structures is noted as the inner zone. The transition from the elongated to the isotropic dendritic structure is known as the Columnar to Equiaxed Transition, CET [Kur98, Spi06, Gan00.1 and Gan00.2]

For a given elementary closed reference volume, VER (A^{VER},V^{VER}), the heat balance can be written as follows:

$$q_e \frac{A^{VER}}{V^{VER}} = -\rho c_p \frac{dT}{dt} + \rho \Delta H_f \frac{dg^s}{dt} \quad (1)$$

where q_e [wm^{-2}] is the external heat flux (<0), g^s [–] is the volume fraction of solid phase, $\rho\Delta H_f$ [Jm^{-3}] is the latent heat of fusion per unit volume and ρCp [Jm^{-3}] is the heat capacity per unit volume. During solidification, i.e. dg^s/dt is greater than zero, heating of the system occurs if the released latent heat compensate the extracted energy upon the system geometry, $-q_e(A^{VER}/V^{VER})$, leading to $\dot{T} \geq 0$. This is known as the recalescence and usually observed upon the formation of the equiaxed zone, figure 2.

As indicated by the phase diagram, the creation of a solid crystal from an alloy melt causes a local change in the composition, which is due to the equilibrium condition between two phases (equal chemical potential between the solid and liquid phases). This difference between the solute contents between the liquid and solid phases is known as *solute redistribution* or *segregation*, [Bro66, Fle67], which has an important role on the final structure morphology as well as phases volume fraction. Solute redistribution at the liquid solid interface is available trough the *partition ratio*, k. This parameter describes the difference in composition at a growing solid–liquid interface (when local equilibrium is established and under normal solidification conditions) as follow:

$$k = \frac{w^s}{w^l} \quad (2)$$

Segregation is generally measured in as-solidified state for an initially homogenous binary alloy system. It is designed as *macrosegregation* when it is measured at the scale of the final system. In addition segregation can be measured between dendritic grains (or at the dendrite arms scale) and designed as *microsegregation*. Micro–segregation is generally settled due to the solute redistribution with phase change by diffusion. On the other hand, the macro–segregation is mostly function of the fluid flow and grain movement.

As shown on the phase diagram, Figure 1, the *liquidus slope* m_L link the temperature to the melt composition under equilibrium condition as follow:

$$m_L = \frac{\partial T}{\partial w} \quad (3)$$

The correlation between the temperature and the solid volume fraction depends on the solidification conditions and different physical phenomena at different length scales.

Different models have been developed to calculate what is called *the solidification path*. The most basic relations are known as the Lever Rule and the Gulliver-Scheil models [Kur98] given respectively by equations 4 and 5.

$$g^s = \frac{1}{1-k}\left(1 - \frac{T_M - T_L}{T_M - T}\right) \quad (4)$$

$$g^s = 1 - \left(\frac{T_M - T_L}{T_M - T}\right)^{\frac{1}{1-k}} \quad (5)$$

T_M is the melting temperature of the pure substance A shown in the phase diagram, Figure 1.

For a certain range of the nominal alloy composition, the phase diagram of a binary alloy system (Figure 2) predicts that at the last stage of the solidification two solid phases should be formed jointly: the α and the θ phase. This structure is known as the eutectic structure and can exhibit a wide variety of geometrical arrangement [Kur98]. This structure can also be formed from an initially non-eutectic system (system with a composition below the limit of solubility of solute in the solid phase). In such case, the effect of solute redistribution coupled with a limited back–diffusion in the solid phase, lead at the last stage of solidification to a volume fraction of liquid with a composition equal to the eutectic structure. For binary alloy system, the eutectic structure can be fibrous or lamellar, regular or irregular as function of the entropy of fusion of the two solid phases growing together.

I.1.2 Nucleation

At a given temperature, T_n, below to the liquidus temperature, T_L, with a given undercooling, $\Delta T_n = T_L - T_n$, driving forces for the formation of metastable solids can occur [Herl04]. For the binary alloy system of composition w_0 in figure 1, this is identified by the formation of the primary solid phase, α. This is defined as the "nucleation" of the solid phase. The nucleation might be spontaneous, which is defined as the homogenous nucleation, or "heterogeneous"; i.e. catalyzed using specific particles depending on the melt system.

I.1.2.1 Homogenous nucleation

The first solid to forms in a homogenous melt system defines the nucleation event. This nucleation is referred to as *homogenous nucleation* because it transforms an initially homogenous system (consisting only of atoms in the liquid state) to a heterogeneous system formed by the crystal and the remaining liquid. Lets consider an elementary reference volume of a pure element in the melt state with a given temperature, $T = T_M - \Delta T_r$, below the melting temperature, T_M. To form the first solid grain with radius r, the derivative over the radius r, $\partial/\partial r$, of the difference between the Gibbs free energy of the solid and the liquid phases have to be smaller or equal to zero. This difference can be derived by summing up the volumic, ΔG_v, and the interfacial terms, ΔG_i, of the Gibbs free energy:

$$\Delta G = \Delta G_v + \Delta G_i = \Delta g \cdot v + \sigma A \qquad (6)$$

where σ is the solid-liquid interface energy and Δg is the Gibbs free energy difference between the liquid and the solid per unit volume. By assuming a spherical form of the nucleus and further assuming that the free energy per unit of volume is proportional to the undercooling, ΔT_r, the value of the critical size, r_0, of the crystal which allows equilibrium between the curved solid phase and the melt is given by the following equation:

$$r_0 = \frac{2\Gamma}{\Delta T_r} \text{ with } \Gamma = \frac{\sigma}{\Delta S_F} \qquad (7)$$

The curvature, $K = 2/r_0$, and the Gibbs-Thomson coefficient, $\Gamma = \sigma/\Delta S_F$, are defined so that positive undercooling is associated with a portion of solid–liquid interface which is convex towards the liquid phase. ΔS_F is the entropy of fusion per mole [$Jmol^{-1}K^{-1}$]. Equation 7 indicates that, the smaller the undercooling, the larger will be the size of the first equilibrium solid crystal to form. However, the occurring probability of this is very small. The same approach can be used to define homogenous nucleation in metallic alloy where the Gibbs free energy is function of the nucleus size and the melt composition [Kur98]. Based on this approach, the following quantities could be defined for homogenous nucleation in metallic alloys:

a. The required interfacial energy for a spherical solid grain to remain in the solid state is function of the number of atoms in the crystal and can be written as:

$$\Delta G_n^{hom} = \frac{16\,\pi\,\sigma^3\,T_m^2}{3\,\Delta H_f^2 T^2} \tag{8}$$

b. The densities of the nuclei, that are in equilibrium with radius r, is function of the Gibbs critical energy, and as consequence is also function of the undercooling:

$$n_r^* = n_r \cdot \exp\left(\frac{-\Delta G_n^{hom}}{k_B T}\right) \tag{9}$$

where n_r is the densities of atoms in the melt and k_B is the Boltzmann constant.

c. Additional important parameter in most solidification process is the nucleation rate. This parameter is defined as the number of solid grains appearing within a given melt volume and time. We note N_n as the number of nucleus grain in equilibrium with N_l atoms in the liquid state ($N_l >> N_n$). The steady state nucleation rate can be rewritten as follow [Kur98]:

$$I = I_0 \exp\left(-\frac{\Delta G_n^{hom} + \Delta G_d}{k_B T}\right) \tag{10}$$

I_0 is a pre-exponential factor and ΔG_d is the activation energy required for the transfer through the liquid/solid interface.

I.1.2.2 Heterogeneous nucleation

Nucleation is referred to be *heterogeneous* when it occurs on a heterogeneous system formed by atoms in liquid state together with external particles which is the case of most industrial casting processes. When the melt contains solid particles, or in contact with a crystalline crucible or oxide layer, the probability of the nucleation of small nuclei increases since the number of atoms, or activation energy required for their formation, are decreased. Figure 3 is a schematic view of simplified heterogeneous nucleation event. An elementary volume consisting of atoms in solid phase defining a nucleus in contact with a substrate surface is shown. The equilibrium between the solid, the liquid and the substrate writes:

ΔG = (interface energy creation due to nucleation)

- interface energy gained due to the substrate

$$\Delta G_n^{het} = \Delta G_n^{hom} \cdot f(\theta) \tag{11}$$

$$\text{where } f(\theta) = \frac{[2 + \cos(\theta)]\,[1 - \cos(\theta)]^2}{4} \tag{12}$$

θ is the contact angle between the substrate surface and the grain. For $0 \leq \theta \leq \pi/2$ we can easily found that $f(\theta) < 0.5$ and hence the required interfacial energy to create nuclei is less important when the melt is in contact with a solid surface compared to the case of the creation of nuclei in a fully liquid zone.

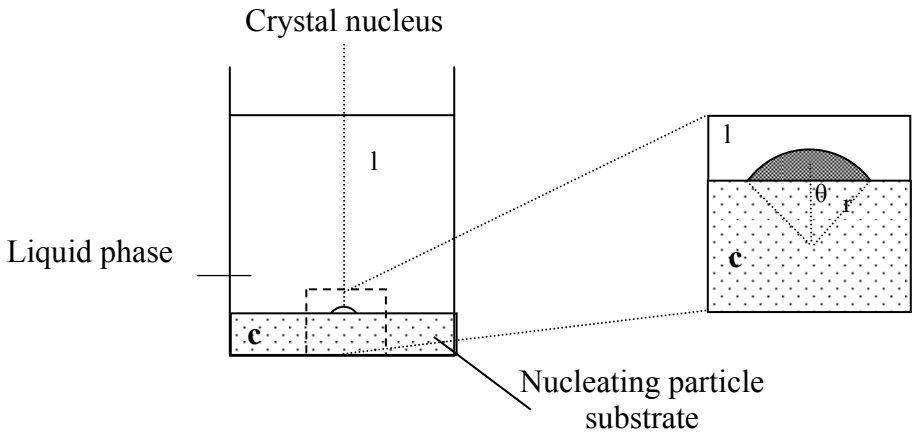

Figure 3: A theoretical model for heterogeneous nucleation. The initial melt system contains several external particles, a single particle assumed to be a planar surface is drawn and designed as the substrate c. The required energy for the nucleation is lower in contact with the substrate. Atoms transfers from the liquid state to the solid state are modeled such as to form a spherical cap of radius, r, with θ the contact angle with the substrate surface.

I.1.3 Morphology of the primary crystal

Once nucleation is achieved and first solids form, for pure metals as well as for metallic alloy system, the solid phase generally exhibits a dendritic morphology. A single dendritic solid grain is defined by all the interconnected parts with the same crystallographic orientation. When a grain grows isotropic in the six orthogonal <100> directions of the space, it is defined as equiaxed. The growth regime is known as columnar when a single growth direction predominates compared to all other directions leading to an elongated dendritic structure. As shown in figure 4, this morphology is commonly characterized by the distance between two primary dendrite trunks, λ_1, and by the spacing between tow secondary arms, λ_2. The first one is commonly used to characterize columnar growth and several correlations, confirmed with experimental measurements, show that it is highly dependent on the gradient in the front of the elongated dendritic structure together with the tip velocity [Kur98]. This parameter can also be defined for equiaxed structure corresponding to the spacing between the primary and the tertiary branches that lie on the envelope of the grains cf. Figure 5 c). The secondary dendrite arm spacing, λ_2, is of one order of magnitude less than λ_1. For a fixed solid structure, λ_2 is function of the solidification time and increases due to species gradient and curvature [Kar98]. Parameters λ_1 and λ_2 are important since they determine the spacing of interdendritic precipitates or porosity and thus have considerable effects upon mechanical properties at as–cast state [Kur98].

The atomics transfer from the liquid to the solid crystal per unit time define the growth rate of the solid-liquid interface which is limited by the capillarity effect, the kinetics of atom attachment to interface, diffusion of heat (pure material and alloy) and solute (in alloys) rejected at the tip.

I.1.3.1 Capillarity effect

An initial planar solid-liquid interface has an excess interface energy and therefore unstable with respect to a system of a lower surface area volume ratio. The relative stability can be expressed by the equilibrium temperature between the liquid and the solid phases and a change in the melting point is expected due to the curvature effect which is called the Gibbs-Thomson undercooling given by:

$$\Delta T_r = \Gamma\left(\frac{1}{R_1} + \frac{1}{R_2}\right) \tag{13}$$

R_1 and R_2 are the principal curvature radiuses at a given point of the interface.

I.1.3.2 Atom attachment kinetics

In the case of a planar interface (pure element) the curvature radiuses are infinite and hence the growth doesn't introduce any undercooling. An additional driven force is responsible of the atoms attachment to the crystal solid interface [Les86]. This term designed as the interfacial kinetic supercooling can be approximated for pure material by:

$$\Delta T_{i\_r} = \frac{v_f}{\mu_0} \tag{14}$$

where v_f is the velocity of the solid-liquid interface and μ_0 can be approximated by :

$$\mu_0 \approx \frac{D^l \Delta_s^l S_f V_m^s}{a R_g T_M} \tag{15}$$

D^l is the species diffusion in the liquid,$\Delta_s^l S_f$ is the volumetric entropy of melting, V_m^s, is the molar volume of the solid phase, a , gap distance which is of the order of magnitude of the intra–atomic distance and finally, R_g, is the ideal gas constant. T_M is the metling temperature.

In most solidification analyses of metallic alloys at low growth rates, the interfacial kinetic undercooling is ignored. However, it becomes significant during rapid solidification as well as for faceted materials solidifying at any cooling rate [Kur98, Sar86].

I.1.3.3 Solute and thermal undercooling

Ahead of a moving solid–liquid interface, in a binary metallic alloy system, a solute field is setting up due the solute rejected and diffused, and also possibly convected, into the liquid phase. In the steady state, we can define a solute diffusion layer, l_c^l, at which the composition of the liquid is equal to the liquid composition at relatively infinite distance from the interface, $w^l = w^{l\infty}$, figure 4 (c and d). In the case of an infinite domain, where solute enrichment of the liquid is neglected, this is equal to the initial composition of the melt, $w^{l\infty} = w_0$. Similarly, a thermal diffusion layer, l_{th}^l, can also be defined with respect to the liquid temperature when $T = T^{l\infty}$. In pure diffusion regime, these two diffusion layer are proportional to the solute, D_c^l, and thermal, D_l^{th}, diffusion coefficients and to the inverse of the velocity of the solid-liquid interface, $v^{s/l}$, and are respectively equal to $l_c^l = D_c^l/v^{s/l}$ and $l_{th}^l = D_{th}^l/v^{s/l}$. Typical value of the solute and thermal diffusion coefficients are respectively of the order of 10^{-13} and 10^{-9} m^2s^{-1} for an Al–Cu system [Kur98]. Hence for a moving interface with typically 100 μms^{-1} we have a solute diffusion length of the order of 10 μm. The thermal diffusion length is much larger, as is the for most metallic alloy systems.

As a consequence, in addition to the curvature and the kinetics undercooling, the growth of the solid-liquid interface is driven by the solute, ΔT_c, and thermal , ΔT_{th}, undercooling defined as:

$$\Delta T_c = m_L\left(w^{l\,s/l} - w^{l\infty}\right) \tag{16}$$

$$\Delta T_{th} = T^{s/l} - T^{\infty} \tag{17}$$

The thermal undercooling is negative in the case of columnar growth, indeed the temperature field increases as we move inward from the solid-liquid interface. This is not the case of equiaxed growth where the released latent heat due to phase transformation is diffused in front of the grain and hence temperature decreases in the surrounding melt with distance from the s/l interface. The solute undercooling is always greater than zero since solute diffusion is much larger in the front of moving s/l interface in the melt rather than in the dendritic patterns. The total undercooling is given by the sum of the curvature, kinetics, solute and thermal contribution as:

$$\Delta T = \Delta T_r + \Delta T_{i\_r} + \Delta T_c + \Delta T_{th} \quad (18)$$

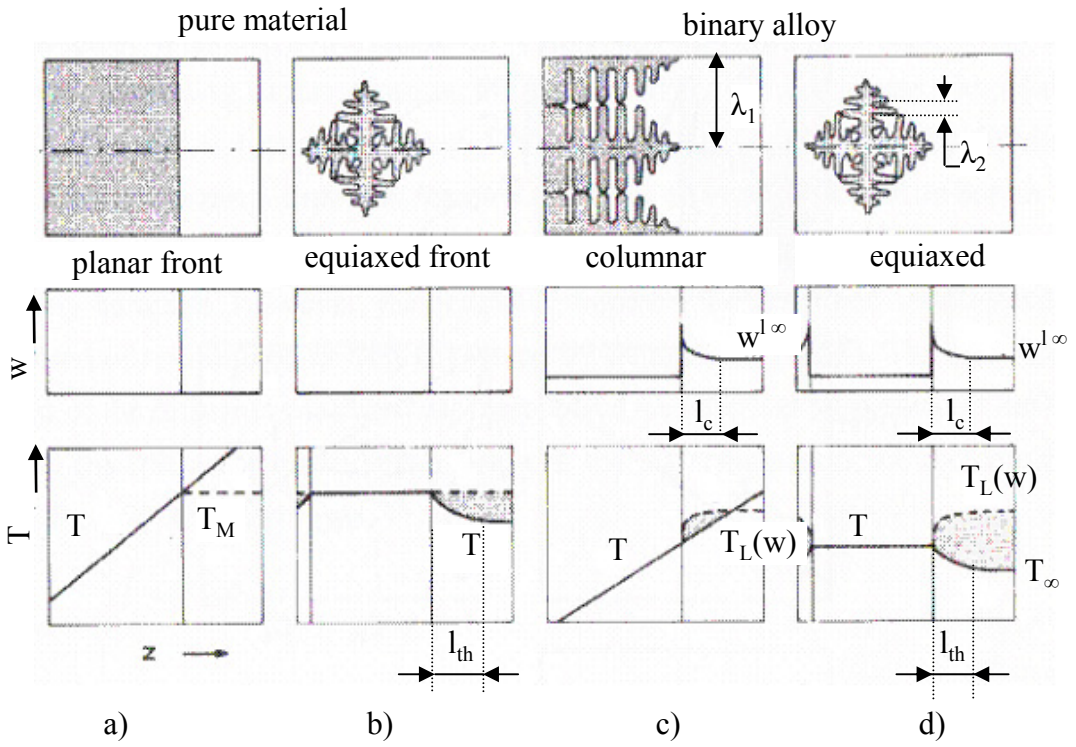

Figure 4: Morphology of the solid structure, the temperature field in the case of pure material, (a and b) together with the concentration field in a binary alloy system, (c and d). The primary dendrite spacing, λ_1, measured between primary dendrite trunks as well as the distance between two secondary arms, λ_2 [Kur98] are drawn (upper figures in the c and d columns). Columnar growth is characterized by a positive temperature gradient at the front of the growing structure, temperature increase as the distance decrease from the solid-liquid interface, while a negative gradient sets up at the front of the equiaxed structure. The solutal and thermal undercooling lead to the instability of the structure resulting in dendritic structure.

I.1.4 Growth kinetics of the dendrite tip

Many research work have been carried out to study the growth of the dendritic structure in metallic alloys, [Herl04, Kur98], as well as in transparent material, [Mik69]. The common objective of these works is to calculate the growth rate as a function of the ratio of the change in concentration (or temperature) of the dendritic interface at the tip, $w^{l/s} - w^{l\infty}$, to the equilibrium concentration (or temperature) difference, $w^{l\,s/l}[1-k]$. The ratio of these quantities is known as the solutal (thermal) supersaturation noted Ω and equal to:

$$\Omega_c = (w^{l/s} - w^{\infty})/([1-k]\cdot w^{l/s}) \quad (19)$$

$$\Omega_{th} = \frac{\Delta T_{th}}{L/c_p} \quad (20)$$

I.1.4.1 Dendrite tip growth in pure diffusion regime

The growth rate of the solid phase increases with the increase of the supersaturation. The heat and mass rejection rate, and therefore the growth rate, is influenced by the shape of the tip. At the same time, the form of the tip is affected by the distribution of solute and temperature fields. All these interactions make the development of exact theory for the dendrite growth velocity extremely complex [Kur98]. In order to overcome the complexity arising from the dendritic structure geometry, the dendritic shape is commonly described as a paraboloid of revolution as originally proposed by Papapetrou [Pap35]. Two steadily growth regimes could be defined; pure diffusion regime and the growth in the presence of fluid flow. Under steady state and in pure diffusion regime, the resolution of the temperature field ahead of the moving paraboloid of revolution interface leads to a relation between the supersaturation, the tip radius, r_p, and the tip velocity, v_p, as follows:

$$\Omega_{th} = Iv(Pe_{th}) \tag{21}$$

where, Iv, is the Ivantsov function and, Pe_{th}, is the thermal Peclet number defined respectively as:

$$Iv(u) = u \exp(u) \int_u^{\infty} \frac{\exp(-t)}{t} dt \tag{22}$$

$$Pe_{th} = \frac{r_p v_p}{2D_{th}^l} \tag{23}$$

The resolution of the solute layer in steady state pure diffusion growth gives a similar relation between the chemical supersaturation, Ω_c, the tip radius, r_p, and the tip velocity, v_p, as follows:

$$\Omega_c = Iv(Pe_c) \tag{24}$$

where Pe_c is the solute Peclet number defined as:

$$Pe_c = \frac{r_p v_p}{2D_c^l} \tag{25}$$

For a given supersaturation, equation 21 and 24 establish the relation between the tip velocity and radius in pure diffusion regime. Hence for a constant undercooling, the product $r_p V_p$, is then constant and means that either a dendrite with small radius will grow rapidly or one with a large radius will grow slowly. In order to calculate the resulting velocity or the tip radius, additional equation is then required. Several experiments indicate that the radius of curvature of the dendrite is approximately equal to the lowest wavelength perturbation of the tip. As proposed by Langer and Muller-Krumbhaar [Lan77], the dendrite tip grows with a tip radius equal at the limit of stability which is known as the marginal stability criteria [Kur98]. Based on this criterion, Kurz and Fisher

derive the following equation which is valid in the case of thermal dendrite of a pure material under steady state approximation:

$$\sigma^* = \frac{2D_{th}^{l} l_{cap}^{th}}{r_p v_p^2} \tag{26}$$

where σ^* is a constant value known as the stability constant. It exact value is not function of the thermal undercooling and approximately equal to 0.025 ± 0.007 [Gui04]. l_{cap}^{th} is the capillarity length at the tip, function of the material and equal to:

$$l_{cap}^{th} = \frac{\Gamma}{L/c_p^l} \tag{27}$$

where c_p^l is the specific heat for the liquid phase.

For metallic alloy systems, the solute gradient is predominant compared to the thermal one, indeed the ratio D_{th}^{l}/D_c^{l} is typically in the range of $[10^2 , 10^4]$. The solutal capillarity length, l_{cap}^{sol}, is equal to

$$l_{cap}^{sol} = \frac{\Gamma}{m_L[w^{l/s} - w^{s/l}]} \tag{28}$$

It has been established that equation 26 is also valid for a solutal dendrite and gives additional equation to calculate the tip velocity as a function of the solute supersaturation.

I.1.4.2 Dendrite tip growth in the presence of fluid flow

In most industrial casting process, pure diffusion regime has a minor effect and thermal and/or solute fluid flows are present. The melt movement in front of a moving solid-liquid interface is found to have a great consequence on the growth velocity as on the preferential growth directions of the dendritic structure [Bec96, Bad07.1], as well on the solid fraction inside the dendritic grain [Bad07.1]. Depending on the fluid velocity direction with respect to the solid-liquid interface growth direction; heat and mass might be rejected or accumulated in the front of the dendritic interface. When the crystallographic orientation of the dendritic structure is parallel and in the opposite direction to the melt flux, the supersaturation calculated at the front of the interface will increase (since the solute and heat are easily transported away form the interface) and the velocity of the interface will be higher than in pure diffusion regime. Figure 5, gives a simplified view of a single dendrite growing in the presence of relative fluid flux due to the grain sedimentation. Several models as well as experiments have been done to quantitatively calculate the relation between the growth kinetic, the tip radius and the supersaturation in the presence of convection [Gui04, Badi07.1, and Badi07.2]. Gandin et al. [Gan03] developed a correlation based on a fitting of the thermal or the solutal supersaturation versus the Reynolds, Prandtl and Schmidt numbers to the analytical solution developed for the Stokes flow approximation of Ananth and Gill [Ana91] as follows:

$$l_{th} = \frac{2R}{0.5773\ R_e^{0.6996} P_r^{0.5249}} \tag{29.1}$$

$$l_c = \frac{2R}{0.5773\ R_e^{0.6996} S_c^{0.5249}} \tag{30.2}$$

This result has been obtained based on the calculation of the size of a stagnant film, under steady state approximation, located in front of a paraboloidal dendrite growing steadily into an undercooled melt in the presence of fluid flow.

Gérardin have recently proposed a new experimental apparatus to study the fluid flow effect on isolated equiaxed grains [Ger02]. The experimental setup was applied to track the NH_4Cl equiaxed grains sedimentation in a tube containing an undercooled solution of $NH_4Cl–H_2O$[Ger02]. The evolution of the equiaxed structures has been recorded during their fall in two orthogonal plans. This gives access to in-situ measurements of the orientation and the tips velocity of the equiaxed structures. Quantitative measurements of the effect of the fluid flow on the morphology of the dendritic structure have been achieved. On of the major effect is that the equiaxed grains exhibit a called “delta” morphology characterized by a preferential growth in the opposite direction of the fluid flow, cf. Figure 5 a and b.

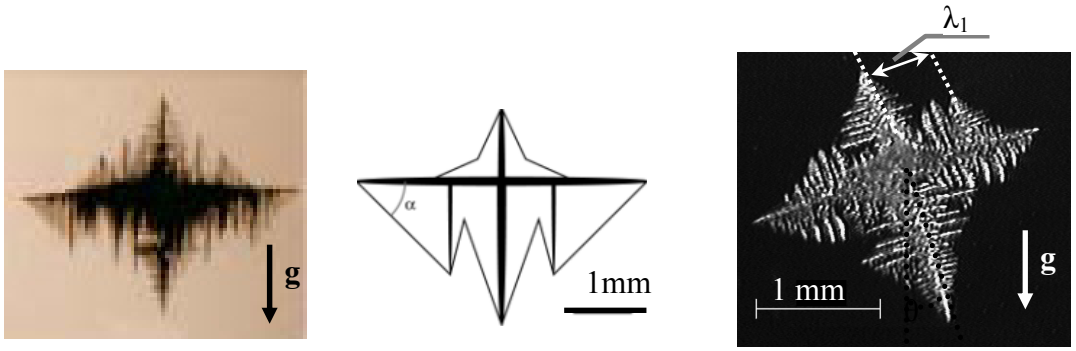

a) b) c)

Figure 5: a) Photograph of an NH_4Cl equiaxed grains falling in a tube containing an undercooled solution of $NH_4Cl–H_2O$[Ger02]. b) a simplified scheme of the “delta” grain asymmetric morphology settled due to the relative fluid flow. c) Typical image of an SCN-acetone equiaxed grain settling in undercooled melt obtained by Badillo and Beckermann [Badi2007.1]. The equiaxed tips at the bottom grow faster than the tips at the top due to the relatively strong flow relative to the crystal.

Similarly, Badillo and Beckermann published experiments of equiaxed grains sedimentation [Badi2007.1]. They measured the dendrite tip growth velocities of equiaxed dendritic crystals settling in an undercooled succinonitrile (SCN)-acetone melt as a function of the falling speed of the crystal and the angle between the dendrite arms and the flow direction. They used the Gandin el al. [Gan03] correlation for the boundary layer together with additional terms in order to account for

the flow angle dependence defined between the dendrite tip and the flow velocity vector. The thermal or solutal supersaturation is written as:

$$\Omega = P_e \exp(P_e)\{E_1(P_e) - f(\theta) E_1[P_e(1+2l/r_p)]\} \quad (31)$$

where, l, is the boundary layer correlation given by Equation 29.2 and $f(\theta)$ is added by Badillo and Beckermann to account for the fluid flow angle and given by:

$$f(\theta) = 1 + \sum_{i=1}^{5} a_i \theta^i \quad (32)$$

where $a_1 = -6.11\ 10^{-2}$, $a_2 = 1.67\ 10^{-3}$, $a_3 = -2.0.2\ 10^{-5}$, $a_4 = 1.065\ 10^{-7}$ and $a_5 = -2.08\ 10^{-10}$.

Badillo and Beckermann compare the average equiaxed tips velocity to the prediction of the standard theory for the growth of a paraboloid of revolution tip in pure diffusion regime. They found that the average tip growth velocity of the six primary dendrite arms of an equiaxed crystal, with a relatively strong flow during the grain sedimentation, is in excellent agreement with the standard diffusion theory result [Badi07.1].

I.1.5 Growth of the eutectic structure

As given by the phase diagram, for a binary alloy system A–B, the two solid phases are at a very different composition, while the melt composition, w_E, is intermediate in value. Under the steady state assumption, the mean composition of the solid must be equal to the composition of the melt [Kur98]. The two eutectic structure solid phases, α and θ, adopt a growth behavior guided by bidirectional solute diffusion from and to each phases due to the jump in composition at the α/θ interface. In the following, we will focus on regular lamellar eutectic structure and the eutectic interface will be defined by the α and the θ interfaces in contact with the bulk. At steady state, very limited solute layer is settled in the liquid with a thickness of the order of magnitude of the phase separation, λ, figure 6. The proximity of the lamellae increases the diffusion between the two phases and also causes departure from the equilibrium described by the phase diagram due to the capillarity effect. As the solute diffusion boundary layer in the liquid is very small, the temperature of the growing interface is close to the equilibrium eutectic temperature. The characteristic eutectic structure spacing, λ, chosen by the eutectic structure, is the one which makes the minimum undercooling at the eutectic interface and hence is a compromise between the capillarity effect and the solute diffusion effect. We suppose that the species diffusion in the liquid is constant for the alloy composition denoted, D^l. Jackson and Hunt derive a kinetics model for the growth of the eutectic structure that could be written as follow [Kur98]:

$$\overline{v_n^e} = \Delta T^2 / (4\ K_r\ K_c) \quad (33)$$

$$\lambda^2\ \overline{v_n^e} = K_r / K_c \quad (34)$$

$$\lambda\ \Delta T = 2\ K_r \quad (35)$$

$\Delta T = T_E - T$ is the settled undercooling ahead the eutectic structure interface with the melt. K_r and K_c are two constants describing respectively the capillarity and the constitutional effects. They can be written as:

$$K_r = \left[2(1-f) \left| m_L' \right| \Gamma^{\alpha} \sin(\theta_1) + 2f \left| m_L \right| \Gamma^{\theta} \sin(\theta_2) \right] / \left[-f(1-f) \left[\left| m_L \right| + \left| m_L' \right| \right] \right] \quad (36)$$

$$K_c = \left[C' / (2 \pi D^l) \right] \left| m_L \right| \left| m_L' \right| / \left[\left| m_L \right| + \left| m_L' \right| \right] \quad (37)$$

where m_L and m_L' are respectively defined by the α and the θ phases liquidus slope. C' is equal to the difference between the two solid phases concentration forming the eutectic structure, i.e. $C' = w^{\theta} - w^{\alpha}$, in Figure 1. f is the fraction of the primary solid phase α in the eutectic structure, Γ^{α} and Γ^{θ} are the Gibbs-Thomson coefficients defined with respect to the α and the θ solid phases, and θ_1 and θ_2 are the contact angle between the α and the θ solid phases and the liquid, respectively.

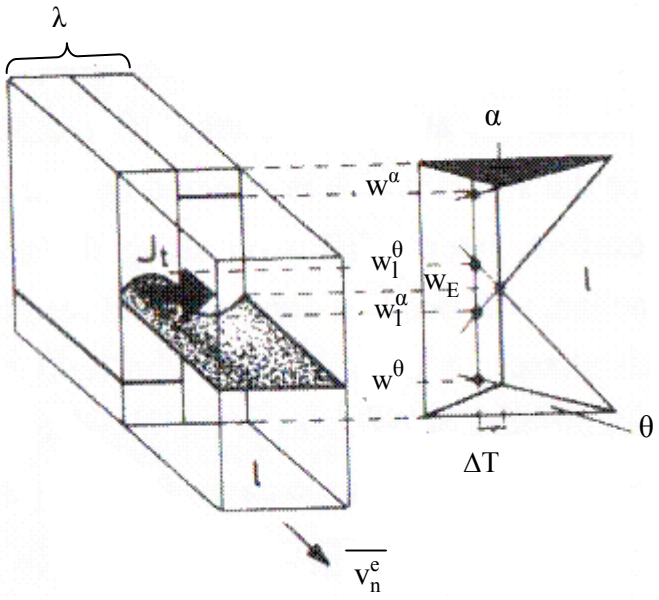

Figure 6: A Schematic view of eutectic diffusion field. The eutectic interface grows with a given undercooling, $\Delta T = T_E - T$, in an infinite melt. Diffusion field is created between the two solid phases due to the concentration jump at the α/θ interface. Diffusion between the two solid phases increases as the distance between the two lamella decreases. The settled characteristic spacing, λ, of the eutectic structure is the one which makes the minimum undercooling at the eutectic interface and hence is a compromise between the capillarity effects and the solute diffusion effects. The boundary diffusion layer in the liquid is very small and approximately equal to the lamellae thickness, λ.

I.2 Containerless solidification technique

Different experimental techniques have been developed to study the solidification in metallic alloys. In the recent past, containerless processing techniques have received great interest and had become one of the most advanced technique for undercooling metals and metallic alloys [Herl93]. The reason is that heterogeneous nucleation, induced by the container wall in conventional process, is avoided and a large degree of undercooling could be achieved. There is a variety of containerless processing technologies, such as atomization process, where small particles are dropped down in tubes, with a given frequency, producing a spray of droplets of various sizes. This technique has been recently proposed as an experimental model to study segregation in equiaxed solidification by Heringer et al. [Her06] and Prasad et al. [Pra05, Pra]. In this process, every single droplet solidifies under reduced-gravity condition during its free-fall. Samples solidified using the atomization processes are then grouped into size classes and X-ray diffraction and/or electron microscopy are used to extract information about segregation and phase's volume fraction. Extensive work has been done by Prasad et al. [Pra05, Pra] to calculate the heat transfer coefficient between the droplet and the surrounding gas as function of the experiment parameters; gas, droplet size, initial velocity, etc. This information is then integrated in numerical model and allows calculating the temperature curves of the droplet. The main limitation of the drop tube and atomization experiments is that the droplet temperature could not be measured as it falls. Therefore, direct measurement of the phase's nucleation temperatures, recalescence as well as the exact solidification time could not be measured limiting further modeling work. In addition, only a range of droplet size could be processed due the limited experiment time, which is a maximum of 0.5 s for 3 m height atomization tower.

In the recent past, ElectroMagnetic Levitation technique, EML, has been developed by Herlach el al., [Herl93], where a metallic alloy sample is freely suspended by levitation forces avoiding any difficulties arising from chemical reactions of the molten metal with the crucible material. In such conditions, real time measurement could be achieved. Figure 7 shows schematic view of the EML technique designed by Herlach et al. This apparatus is mainly designed to investigate the undercooling and primary solidification behavior of metal drops and alloys. As schematized in figure 7 (right image), the sample is placed within a conical levitation coil consisting of typically 5-7 water cooled copper windings and one or one counter windings at its top. The coil is connected to a high frequency generator of variable power and frequency. The vacuum chamber is backfilled with purified gas such as He maintained under a given pressure. An additional DC magnetic field is used to limit the instabilities such as rotations and/or oscillations of the sample [Herl93]. At the top of the sample, temperature is recorded using a one-color pyrometer with an absolute accuracy of ±3 K and with sampling rate of 100Hz. In addition, a fast temperature sensing device is installed to track the solidification front. Important undercooling has been achieved using the EML technique. The EML experiment can be used to track the mushy zone front and hence calculating the growth velocity as well as its shape morphology as a function of the primary phase nucleation undercooling as illustrated in Figure 8 where the two techniques are presented [Herl04]. In addition to a simple measurement of the spontaneous nucleation in the levitated sample,

heterogeneous nucleation could be initiated with the EML technique. Indeed, for a given temperature below the liquidus temperature, a needle is designed to trigger the nucleation of the solid phase at the bottom of the sample. Both homogenous and heterogeneous nucleation have been achieved using EML technique and temperature curves, phases distribution as well as volume fraction has been calculated for Al-Cu alloys for a wide range of undercooling and composition [Kas08, Gan08].

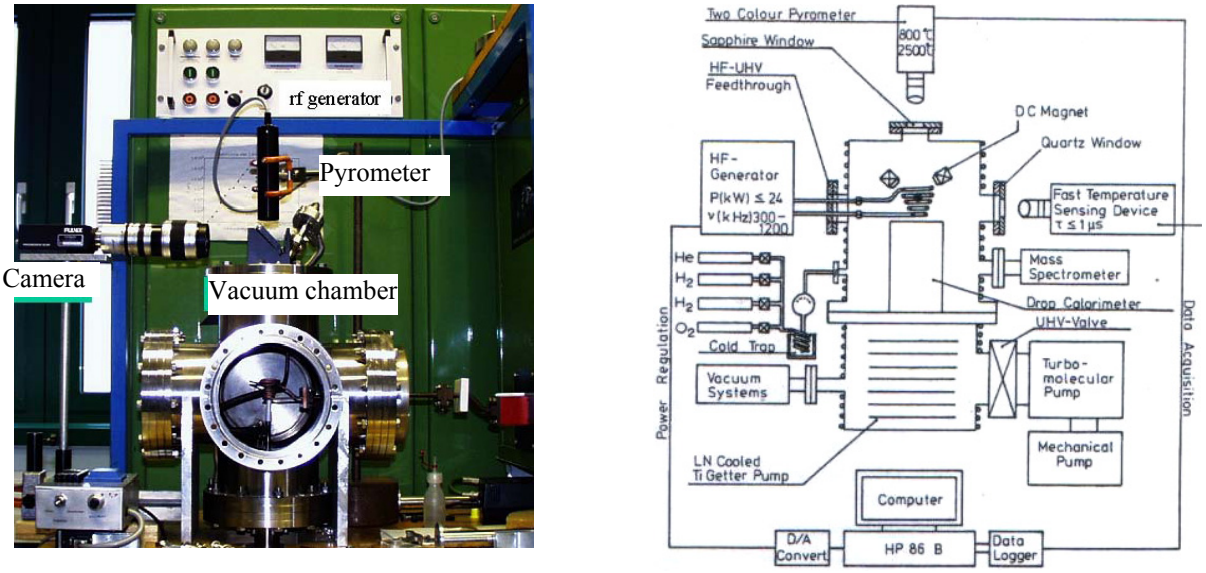

Figure 7: On the left, photograph of the EML experimental set-up and on the right schematic view of the connection of the main parts. The metallic sample is maintained in levitation in the vacuum chamber inside a coil connected to a high frequency generator of variable power and frequency. The intensity of the alternative current flowing through the coil is adjustable allowing the control of the intensity of the induced electromagnetic field. An optical pyrometer is installed to permit direct measurement of the sample temperature. In addition, a high speed camera is installed to record the advancement of the solidification front in particular at small and medium undercoolings [Herl93].

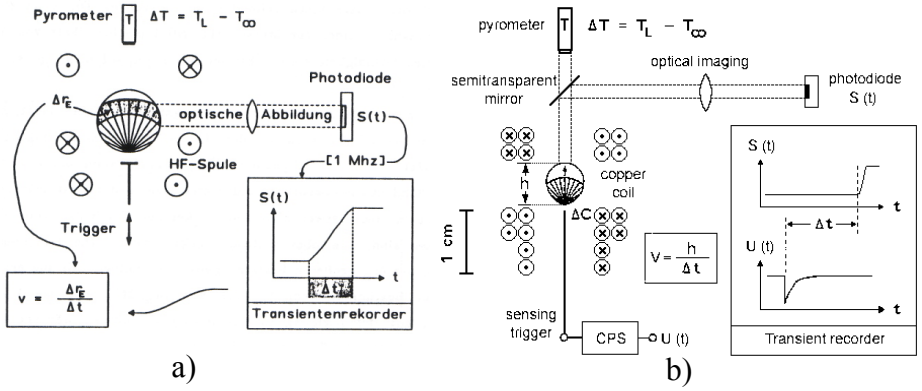

Figure 8: Principles of measurements of dendrite growth velocities in levitation undercooled droplet, a) by using a capacitance proximity sensor, and b) by photo sensors. In both cases solidification is triggered externally by a stimulus needle so that mushy zone front is well known.

I.3 Modeling of segregation and grain structure

Numerical modeling of the solidification in metallic alloy ceaselessly receives a great interest with the development of computer tools and since the work of Oldfield [Old66]. Solidification phenomena, as presented earlier in this chapter, involve many physical phenomena such as heat and mass diffusion, dendritic morphology, capillarity effect, etc. These phenomena interact with each other and predominate at different length scales. Indeed, heat transfer during casting process can be studied at the called macro scale, i.e. scale of the solidified part, using finite element formulation with a reasonably discretization of the simulation domain. However at the solid-liquid interface heat and mass interaction require a finest discretization of the space. Moreover, accurate modeling of the solid-liquid interface requires accounting for the capillarity effect and hence decreasing of the scale at which the mathematical equations of physics laws are valid. Phase field modeling is mostly then used for the prediction the solid-liquid interface morphology as well as heat and mass diffusion. However, the required computer resources as well as the simulation time dramatically increase with finest time and spatial discreatizations. Up to now and for a near future, phase field model remains unsuitable for the industrial solidification processes. In this section, we will give a non-exhaustive overview of modeling work of solidification of undercooled melt at macro and/or microscopic scales.

I.3.1 Modeling of equiaxed solidification

Based on experimental observations on submicron aluminum alloy powders produced by electro–hydrodynamic process, [Levi 82.1], Levi and Mehrabian developed a numerical model for the solidification of a spherical pure aluminum sample where a dendritic growth is assumed from the surface of sample [Levi 82.2]. They first assumed a uniform temperature in the sample and solve the energy equation of the system in a bispherical coordinate system. The shape of the grain is assumed to be spherical and a growth of a fully solid spherical interface is modeled. No solute

interaction is considered as well as any back diffusion in the solid. Despite the fact that they extend their work by taking into account possible thermal gradient in the droplet, based on the calculation of the Biot number, their model remains a simple thermal analysis and the dendritic morphology of the grain is not considered. The main result of their work is the effect of the undercooling on the cooling history of the sample, i.e. latent heat release and solid front growth rate.

Rappaz and Thévoz, [Rap87.1] developed a numerical model for equiaxed solidification where solute diffusion, ahead of the growing grain interface, is considered as the main driving force for the grain growth. Equiaxed grain is assumed to grow until it reach a final radius, denoted, R^f. The temperature of the final volume is supposed to be uniform and equal to the solid-liquid interface (primary dendrite tips) temperature. Back diffusion in the solid phase is neglected and the shape of the grain is again assumed to be spherical. However, important conceptual notions have been introduced by Rappaz and Thévoz. Firstly, two distinguished liquid phase are defined; the intra, d, and extra, l, dendritic liquid phase with two different compositions. The Secondly, An internal solid fraction, g^i, is introduced. This quantity is equal to the ratio of the solid volume fraction, g^s, to the grain (supposed to be a mixed volume of solid and liquid phase) volume fraction, g^m as $g^i = g^s/g^m$. The liquid inside the grain boundary, d; is supposed to be in equilibrium with the solid phase and its composition is given by the phase diagram, $w^d = [T-T_M]/m_L$. Rappaz and Thévoz linked the solute balance equation describing the solute diffusion in the extra-dendritic liquid, outside the mushy zone defined by the spherical grain interface, with the heat and the mass conservation equation of the system, consisting of the volume initially liquid delimited by the expected final grain radius, R^f. In the analytical derivation of their model, [Rap87.2], an analytical formulation of the solute boundary layer correlation is given to calculate the solute profile in the front of the growing mushy zone. However, back diffusion in the solid phase is neglected and the model is only valid for equiaxed solidification.

Wang and Beckermann, [Wang93.1, Wang93.2] developed a similar model based on volume averaging of the conservation equations written for the solute, the mass and the heat at the scale of each single phase. Both back diffusion of the solute in the solid phase as well as in the extradendritic liquid phase are modeled. Typical dendritic spacing, such as the primary λ_1 and the secondary λ_2 dendrite arm spacing have been integrated in the formulation of the diffusion boundary layers in the solid phase and the final grain radius. Although the morphology of the grain is oversimplified, a shape factor is introduced to account for the real dendritic morphology of the grain. Martorano et al. [Mar03] applied this model for the Columnar to Equiaxed Transition, CET, observed by Gandin [Gan00.1]. Beckermann and co-author extend their work to take into account fluid flow and macroscopic thermal and solute gradients [Wan96.1, Wang96.2].

Similarly, Heringer et al. has applied the averaging theorems to derive a solidification model for equiaxed solidification in atomized droplet [Her02, Her04, Her06] solved using finite volume method. A single nucleation event is assumed at the center of the droplet exchanging heat by convection with the surrounding gas during its fall in the atomization tower. The model predicts

systematic remelting of the supersaturated solid structures and a spherical segregation pattern. However application of the model is limited to nucleation and growth of a single grain from the center of a spherical domain. In addition, back diffusion in the solid phase is neglected.

Recently, Appolaire et al. proposed a new multi-component multiphase model for equiaxed solidification [App07]. Lagrangian formulation is used to describe the movement an equiaxed grain in an undercooled bulk. Solidification and possible remelting of the solid phase are integrated in the model for the prediction of the mushy zone evolution. In addition, their model takes into account the coarsening of the secondary arms, i.e. the increase of the secondary dendrite arm spacing λ_2 with time, using the Mortensen model [App07]. Two growth regime have been distinguished, the globular and the dendritic regime, based on a critical value of the size of the equiaxed grain. However, the fluid flow effect on the evolution of λ_2 has been neglected.

I.3.2 Modeling of the grain structures interactions, heat and mass transfer

Extensive works have been achieved in the last two decades to develop new models capable to predict solidification grain structures in as-solidified state. Gandin and Rappaz [Gan94, Gan95] have proposed a new model based on coupling between a classical Finite Element, FE, formulation and a grid of cubic cells. The approach is based on an individual description of the dendritic grain by spatial discretization into a cell grid, where each cell is an automaton characterized by finite numbers of state indices. Transition rules for each cell state indices are based on deterministic rules and the status of the surrounding cells. In 2D, the cellular automaton model could be schematized as in Figure 9. Two discretization spaces are defined, the finite element mesh and the cellular automaton grid. A coupling scheme is defined so that for each finite element, F, cells having their center contained in the element area are assigned to the element F. Interpolation coefficients, $c_v^{n_i^F}$, are defined to calculate the cell enthalpy variation from the three nodes, N_n^F, of the triangular element F. Interpolated enthalpy are then converted in solid volume fraction using the Gulliver-Scheil model. Random nucleation has been implemented in order to model heterogeneous nucleation with a random crystallographic orientation of the grains. Gandin and Rappaz successfully predict solidification microstructure as well as grain competition [Gan94, Gan95].

Recently, Guillemot et al. extended the Gandin and Rappaz approach [Gui04]. Firstly, they integrate an important physical notion which is the grain volume fraction by using an advanced coupling scheme between the CA model and the FE model [Gui03]. For each CA cell partially recovered by a dendritic grain, mushy zone volume fraction is calculated, leading to a more accurate agreement between the CAFE model prediction and a one-dimensional front tracking thermal method [Gan00.2] in term of the predicted cooling curves. Secondly, in addition to interpolation from the FE model as proposed by Gandin and Rappaz, Guillemot et al. proposed to use the same approach for solute balance at the macro-scale, i.e. FE model. Grain structure interaction with the fluid flow (calculated at the FE) is modeled by the CA model. While the proposed Guillemot et al. modified CAFE model integrates advanced solidification phenomena,

however the calculation of the internal solid volume fraction at the CA model is oversimplified using lever rule model.

The main purpose of this contribution is to jointly achieve experimental and numerical modeling of equiaxed solidification. An experimental EML set-up will be used to process Aluminum-Copper alloy spherical systems. Extensive experimental data will be extracted from the EML solidified samples. In addition, the approach proposed by Wang and Beckermann [Wan93.1] will be used as a primary modeling tool for the study of the experimental results. Then, the CAFE model developed by Guillemot et al. [Gui04] will be considered. Development on the CAFE model will mainly be focused on the integration of advanced segregation model to calculate the internal solid volume fraction at the scale of the CA model. Additional improvements will concerns the coupling between the FE and the CA models. The coupled CA and FE model will be then applied for the simulation of recently available experimental model for the study of macrosegregation and macrostructure in typical cavity casting process [Dav83].

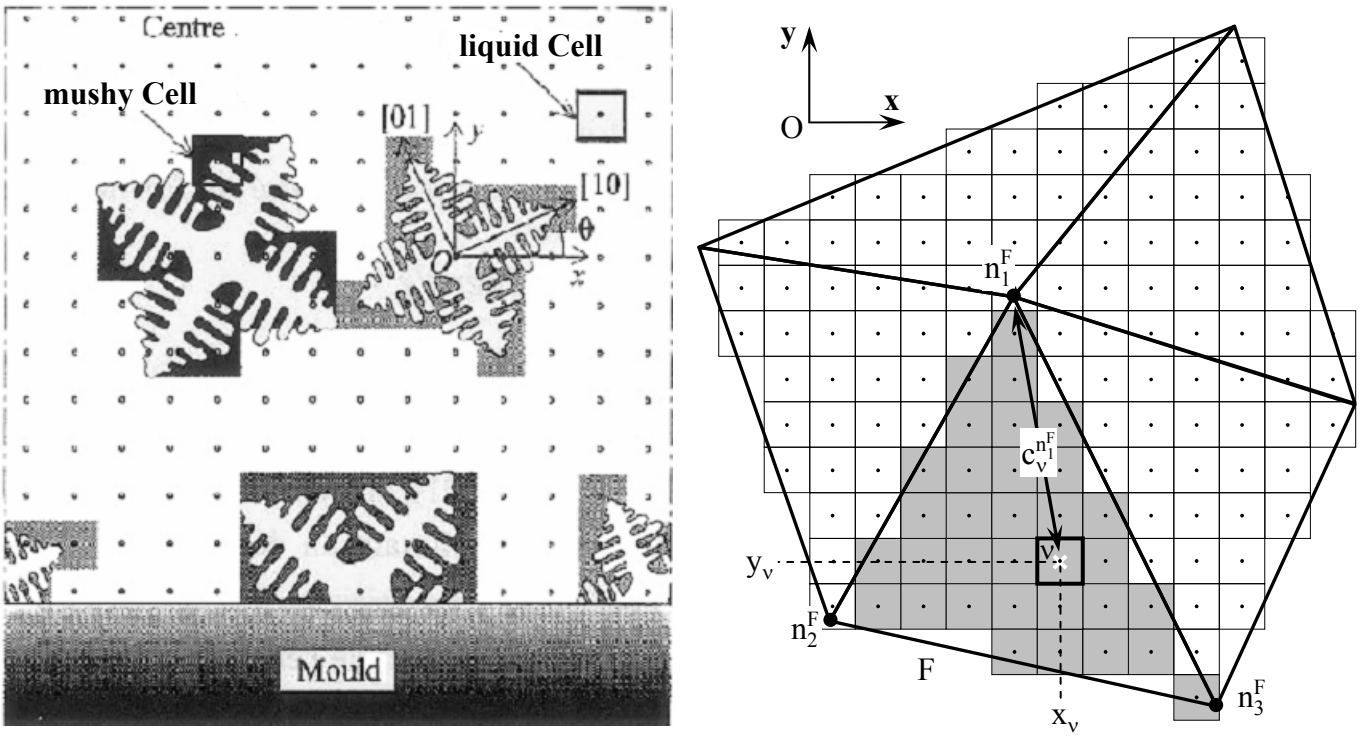

a b

Figure 9: a) 2D schematic view of the CAFE model concept developed by Gandin and Rappaz [Gan94] where several dendritic grains growing in an initially liquid domain are shown. Cells are represented only by their center located at the (x_ν, y_ν) position. Cells located in a fully liquid zone are considered as 'liquid cell' and those which are totally or partially covered by the mushy zone are denoted as 'mushy cell' [Gan94]. b) The coupled concept of the cellular automaton-finite element model is illustrated where a portion of the cellular automaton grid superimposed to a finite element mesh is drawn together with the topological links between a given triangular finite element, F, and a square cell of the cellular automaton grid, ν are defined. Interpolation coefficients, $c_\nu^{n_i^F}$, are defined between each cell and the N_n^F nodes of the finite element mesh, n_i^F, with i=[1, N_n^F] and N_n^F=3 [Gui06].

Résumé en Français :

Chapitre II Experimental and numerical modeling of equiaxed solidification in metallic alloys

Dans ce chapitre, la technique de solidification par lévitation électromagnétique est considérée comme modèle expérimental pour l'étude de la solidification équiaxe. Cette technique est utilisée pour élaborer des échantillons d'alliage aluminium cuivre avec trois compositions de cuivre; 4, 14, 24pds%. Une description du modèle expérimental est donnée ainsi que les investigations expérimentales durant et après la solidification des échantillons.

La température mesurée pour chaque échantillon durant sa solidification est rapportée permettant d'accéder aux surfusions de germination et recalescences des structures primaires et eutectiques. D'autre part, des investigations chimiques et des analyses d'images de la surface centrale pour chaque échantillon sont décrites. Ces investigations post-solidification donnent accès aux cartes de composition chimiques, de fraction d'eutectique et d'espacement inter−dendritiques secondaires. Ces mesures révèlent des corrélations entre les trois cartes ainsi que des ségrégations à l'échelle de l'échantillon.

Un modèle multiphasique est développé basé sur la méthode de prise de moyenne volumique. Ce modèle prend en compte la surfusion et germination de la phase primaire ainsi que celle de la structure eutectique. L'application du modèle aux gouttes solidifiées en lévitation électromagnétique montre l'effet de la surfusion, la recalescence et la croissance de la structure eutectique sur les fractions finales de phases.

Chapter II Experimental and numerical modeling of equiaxed solidification in metallic alloys

Abstract

Nucleation undercoolings are measured for the primary dendritic structure and for the eutectic structure in aluminum-copper samples solidified during electromagnetic levitation. The recorded cooling curves are also used to determine the heat extraction rate and the solidification times. Additional characterizations consist of composition measurements using a scanning electron microscope (SEM) equipped with energy dispersive x-ray spectrometry and analyses of SEM images. The distribution maps drawn for the composition, the volume fraction of the eutectic structure and the dendrite arm spacing reveal strong correlations. An equiaxed solidification model based on mass and heat balances is developed for the interpretation of the measurements. The model predicts the effect of diffusion in the liquid and in the solid, as well as the consequences of the recalescences occurring immediately after the nucleation of the primary dendritic structure and the eutectic structure. The nucleation undercooling of the eutectic structure is shown to be a key parameter for a quantitative prediction of the fraction of phases in the solidified samples.

Keywords

Equiaxed dendritic growth, Eutectic structure, Modeling, Segregation, Solidification

II.1 Introduction

Modeling of equiaxed dendritic solidification in casting [1-5] is rarely compared with segregation measurements. One of the difficulties to carry out such measurements is to define a volume associated with equiaxed growth as a closed system with respect to mass transfer. Recently, Heringer el al. proposed that an individual droplet produced by atomization could be used as a model for equiaxed growth [6]. Indeed, this system includes several features characterizing equiaxed growth: representative size, spherical shape, limited temperature gradient, single nucleation event as well as little variation of the heat extraction rate throughout the entire surface of the droplet within the solidification interval. The main drawback is the difficulty to measure the thermal history of an individual droplet during its flight in the atomization tower. This data is yet required for calibration of model parameters such as the cooling rate prior to solidification and the nucleation undercooling of the dendritic and eutectic structures.

Electromagnetic levitation is a powerful technique to study the dynamics of the solidification of undercooled liquid [7]. In conjunction with *in situ* measurement techniques, it can be used to determine the kinetics of crystal growth at tailored nucleation undercooling, the competition for the nucleation of phases in an undercooled liquid and the nature of the successive phases formed upon solidification of complex alloys [8, 9]. Measurement of thermophysical properties is also possible thanks to this technique [10].

In the present contribution electromagnetic levitation is proposed as an experimental technique to study segregation taking place upon equiaxed solidification. Because the volume of the liquid is a few cubic millimeters and is fixed in space, it is possible to use a pyrometer to record its temperature evolution during solidification. Measurements are conducted on aluminum-copper (Al-Cu) alloys. For each sample, metallurgical characterizations are performed to produce distribution maps of the average composition of copper, the volume fraction of the eutectic structure and the dendrite arm spacing. Predictions of a model developed for equiaxed solidification are then compared with the measurements mainly considering the temperature evolution and the volume fraction of the eutectic structure.

II.2 Experimental

An alternating radio-frequency electromagnetic field generated in a conically shaped coil was used to levitate and to melt metallic samples [7]. Samples with typically 0.2 g in mass were prepared from pure Al (99.9999 %) and Cu (99.999 %). Compositions were selected as 4, 14 and 24 wt% Cu. A low gas pressure of 40-50 mbar He was maintained during levitation in order to dissolve oxides from the surface of the sample. Once melted, the metal consisted of an approximately spherical liquid volume with a diameter close to 5.3 mm. The levitated sample was then cooled and undercooled by reducing the radio-frequency power. Solidification set in spontaneously when a certain degree of undercooling was achieved. The nucleation temperature was thus uncontrolled, oppositely to the method consisting of touching part of the sample with a triggering device once the desired undercooling is reached. Although a map of the grain structure was not produced, the number of activated nuclei is expected to be very limited based on previous observations. A single grain was indeed found in an atomized Al-Cu droplet [6] as well as in a levitated droplet [11]. Explanation involves both the size of the system as well as the recalescence taking place immediately after nucleation due to the growth of the dendritic mushy zone, thus preventing the system to further cool down and new nucleation events to take place.

II.2.1 Temperature history

The temperature was continuously recorded at the top of each sample during the solidification experiment using a one-color pyrometer with a constant emissivity of 0.2 [7]. The accuracy of the pyrometer is approximately ± 3 K when measuring an ideal flat and smooth surface. However the samples consist of almost spherical droplets with a non-ideal surface. A calibration was thus required to calculate the actual temperature, T, using equation $1/T = (1/T^{pyr}) + (1/T_L) - (1/T_L^{pyr})$, where T^{pyr} is the temperature recorded by the pyrometer, T_L^{pyr} is the liquidus temperature measured by the pyrometer, and T_L is the liquidus temperature read on the phase diagram.

II.2.2 Distribution maps of the volume fraction of the eutectic structure

Each spherical sample was cut throughout a central meridian cross section to investigate the solidification structure. The back scattered electron detector of a Scanning Electron Microscope (SEM) was used to acquire grey scale digital images with a magnification of 452 and a resolution of $1.024 \cdot 10^{-6}$ m per pixel. The images were then assembled without altering the resolution in order to obtain a whole view of the structure of the sample cross section. Additional filters involving improvement of the contrast and then a grey level threshold were required to create a binary black and white image distinguishing between the dendritic and the eutectic structures. This procedure was found to generate a maximum error estimated to 7%. The area fraction of the black pixels directly gave access to the average eutectic volume fraction, g_D^e.

II.2.3 Distribution maps of the dendrite arms spacing

The average dendrite arms spacing (DAS) of the primary dendritic phase was also computed for the entire sample cross section. For that purpose, evenly spaced horizontal lines drawn through the same binary black and white images were analyzed sequentially. The algorithm identified the number of phase boundaries along the lines. This information was then used to determine the average size of the dendrites along the measurement axis by dividing the total length of the lines by the number of phase boundaries. The DAS is thus directly given as a mean intercept with no attempt to correlate it to a three dimensional morphology of the dendritic structure. Estimation of the maximum error was found to be of the order of 1%. Note that the use of horizontal lines is justified by the apparent isotropic distribution of the structure at the scale of the entire cross section. For the measurement of the distribution maps, the digital image of the whole cross section was divided in several square zones on which similar measurements were carried out. The size of the square zone was chosen equal to $150 \cdot 10^{-6}$ m $\times$ $150 \cdot 10^{-6}$ m in order to contain several dendrite arm spacings. All manipulations and measurements on images were carried out with the help of the software ImageJ [12].

II.2.4 Distribution map of the average copper composition

Measurements of the average copper composition were conducted by energy dispersive x-ray spectroscopy (EDS) using the secondary electron detector of the SEM at a magnification of 4520 and a beam strength of 20 kV. This magnification was selected in order to divide the scan of the sample surface into a cubic array of $40 \cdot 10^{-6}$ m $\times$ $50 \cdot 10^{-6}$ m zones. The elemental composition of each zone, measured with an error of the order of 0.5 wt%, was recorded with its spatial coordinates. It should be noted that the samples were mounted in a carbon-based resin containing small quantities of copper. Since no carbon was detected in the Al-Cu alloys, the recorded composition data were filtered based on the carbon content, thus differentiating between measurements conducted in the resin from those in the samples. The distribution map of the copper composition was reconstructed by assembling the individual zones. For a better representation of the average composition using a distribution map, a volume averaging procedure was used. It simply consisted on the application of a filter that averaged neighboring values and represent it on a larger rectangle. The size of the rectangle was chosen equal to $120 \cdot 10^{-6}$ m $\times$ $150 \cdot 10^{-6}$ m so as to encompass several times the dendrite arms spacing, thus also permitting explorations of possible correlations between the distribution maps for the Cu content, the DAS and the fraction of eutectic.

II.3 Modeling

The model is based on an extension of the segregation analysis proposed by Beckermann and co-workers for equiaxed solidification in casting [2-3, 13], refereeing solely to the formation of a primary dendritic structure into an undercooled liquid. It is extended to consider the formation of a secondary eutectic structure first formed in the interdendritic liquid of the mushy zone and finally developing into the remaining undercooled liquid outside the mushy zone up to the completion of solidification.

II.3.1 Mass conservations

Considering a multiphase multicomponent system of volume V with fixed phases and no mass exchange with its surrounding environment, the conservation of the total mass of α-phase and the conservation of the mass fraction of i-species in the α-phase, w_i^α, respectively write:

$$\frac{\partial \rho^\alpha}{\partial t} = 0 \tag{1}$$

$$\frac{\partial (\rho^\alpha w_i^\alpha)}{\partial t} + \nabla \cdot \mathbf{j}_i^\alpha = 0 \tag{2}$$

where ρ^α is the density of the α-phase and $\mathbf{j}_i^\alpha$ is the diffusive flux of the i-specie in the α-phase.

II.3.2 Averaging theorems

Averaging theorems for the derivative over time and space of the mean over a reference volume, V, of quantity, ψ, in the α-phase, ψ^α, write:

$$\left\langle \frac{\partial \psi^\alpha}{\partial t} \right\rangle = \frac{\partial \langle \psi^\alpha \rangle}{\partial t} - \frac{1}{V} \sum_{\beta(\beta \neq \alpha)} \left(\int_{A^{\alpha\beta}} \psi^\alpha \, \mathbf{v}^{\alpha\beta} \cdot \mathbf{n}^{\alpha\beta} \, dA \right) \tag{3}$$

$$\langle \nabla \psi^\alpha \rangle = \nabla \langle \psi^\alpha \rangle + \frac{1}{V} \sum_{\beta(\beta \neq \alpha)} \left(\int_{A^{\alpha\beta}} \psi^\alpha \, \mathbf{n}^{\alpha\beta} \, dA \right) \tag{4}$$

where $A^{\alpha\beta}$ is the α-β interfacial area, $\mathbf{n}^{\alpha\beta}$ is the normal unit vector of the α-β interface, directed from the α-phase toward the β-phase and $\mathbf{v}^{\alpha\beta}$ is the velocity of the α-β interface. The averaging operator and the intrinsic volume average are defined using the phase presence function, γ^α, equal to 1 in the α-phase and 0 elsewhere:

$$\langle \psi^\alpha \rangle = \frac{1}{V} \int_V \gamma^\alpha \, \psi^\alpha \, dV \tag{5}$$

$$\langle \psi^\alpha \rangle^\alpha = \frac{1}{V^\alpha} \int_{V^\alpha} \gamma^\alpha \, \psi^\alpha \, dV = \langle \psi^\alpha \rangle \; / \, g^\alpha \tag{6}$$

where g^α stands for the volume fraction of the α-phase.

II.3.3 Average mass conservations

Application of theorems and definitions (3-6) to equations (1-2) leads to the averaged conservation equations:

$$\frac{\partial \langle \rho^\alpha \rangle}{\partial t} = \sum_{\beta\,(\beta\neq\alpha)} \left(\frac{1}{V} \int_{A^{\alpha\beta}} \rho^\alpha \mathbf{v}^{\alpha\beta} \cdot \mathbf{n}^{\alpha\beta}\, dA \right) \tag{7}$$

$$\frac{\partial \langle \rho^\alpha w_i^\alpha \rangle}{\partial t} + \nabla \cdot \langle \mathbf{j}_i^\alpha \rangle = \sum_{\beta\,(\beta\neq\alpha)} \left(\frac{1}{V} \int_{A^{\alpha\beta}} \rho^\alpha w_i^\alpha \mathbf{v}^{\alpha\beta} \cdot \mathbf{n}^{\alpha\beta}\, dA \right) + \sum_{\beta\,(\beta\neq\alpha)} \left(\frac{1}{V} \int_{A^{\alpha\beta}} \mathbf{j}_i^\alpha \cdot \mathbf{n}^{\alpha\beta}\, dA \right) \tag{8}$$

where the right-hand-side term of Equation (7) defines the exchange rate of the total mass of the α-phase due to the velocity of the α-β interface, the first right-hand-side term of Equation (8) defines the exchange rate of the mass of each i-specie in the α-phase also due to the velocity of the α-β interface and the second right-hand-side term of Equation (8) stands for the exchange rate of the mass of each i-specie in the α-phase due to diffusion. Evaluation of these interfacial transfers terms are conducted using the simplifications:

$$\frac{1}{V} \int_{A^{\alpha\beta}} \mathbf{j}_i^\alpha \cdot \mathbf{n}^{\alpha\beta}\, dA = S^{\alpha\beta} \frac{D_i^\alpha}{l^{\alpha\beta}} \left(\overline{\rho^\alpha}\ \ \overline{w_i^{\alpha\beta}} - \langle \rho^\alpha w_i^\alpha \rangle^\alpha \right) \tag{9}$$

$$\frac{1}{V} \int_{A^{\alpha\beta}} \rho^\alpha w_i^\alpha \mathbf{v}^{\alpha\beta} \cdot \mathbf{n}^{\alpha\beta}\, dA = S^{\alpha\beta}\ \overline{\rho^\alpha}\ \ \overline{w_i^{\alpha\beta}}\ \ \overline{v_n^{\alpha\beta}} \tag{10}$$

$$\frac{1}{V} \int_{A^{\alpha\beta}} \rho^\alpha \mathbf{v}^{\alpha\beta} \cdot \mathbf{n}^{\alpha\beta}\, dA = S^{\alpha\beta}\ \overline{\rho^\alpha}\ \ \overline{v_n^{\alpha\beta}} \tag{11}$$

where $\overline{\rho^\alpha}$ and $\overline{w_i^{\alpha\beta}}$ are averaged quantities in the α-phase at the αβ-interface over surface $A^{\alpha\beta}$ and $\overline{v_n^{\alpha\beta}}$ stands for the average normal velocity of the αβ-interface. The solute diffusion length, $l^{\alpha\beta}$, characterizes diffusion of the species in the α-phase from the αβ-interface based on geometrical considerations and boundary conditions. Finally, D_i^α denotes the diffusion coefficient of each i-specie in the α-phase and $S^{\alpha\beta} = A^{\alpha\beta}/V$ stands for the interfacial area concentration.

II.3.4 Assumptions

While only one thermodynamic liquid phase is present in the system, it is split into two liquid "phases" in the construction of the model as was first proposed by Rappaz and Thévoz [1] and extended by Wang and Beckermann [2-3]. This was justified by the need to consider different properties for the extradendritic liquid, $l^{(0)}$, and the interdendritic liquid, $l^{(1)}$, as sketched in Figure 1 step S1. Similarly, different regions are defined hereafter in order to distinguish between the various structures. The dendritic structure is located in regions (1) and (2) while the eutectic structure is located in regions (2) and (3). Note that the eutectic structure is generally of multiphase nature. However, it is assimilated hereafter as a homogeneous structure with an average composition and the details of its internal distribution of phases is not considered by the model.

The following approximations are considered:

i- *Geometry*. The system is a one-dimensional spherical domain of radius R, with an external surface and a volume denoted A and V, respectively.

ii- *Sequence.* The following solidification sequence is modeled, as schematized in Figure 1:

- (S0). Cooling of the liquid, $l^{(0)}$ (step not shown in Figure 1).
- (S1). Growth of the mushy zone, (1), into the undercooled extradendritic liquid, $l^{(0)}$. The mushy zone is made of the dendritic structure, $s^{(1)}$, plus the interdendritic liquid, $l^{(1)}$. This is the main step described in References [1-3].
- (S2). Growth of an interdendritic eutectic structure, $e^{(2)}$, into the interdendritic liquid of the mushy zone, $l^{(1)}$. The central core of the domain is fully solid. It is made of the interdendritic eutectic structure, $e^{(2)}$, plus the dendritic structure, $s^{(2)}$, formed during (S1) as $s^{(1)}$ and retained within the solid core of the domain delimited by the growth of the eutectic structure.
- (S3). Growth of the extradendritic eutectic structure, $e^{(3)}$, into the remaining extradendritic liquid, $l^{(0)}$.
- (S4). Cooling of all solid phases, $s^{(2)}+e^{(2)}+e^{(3)}$ (step not shown in Figure 1).

iii- *Heat transfer*. The system is uniform in temperature over space. Its time evolution follows a global heat balance defined by a heat extraction rate at the limit of the domain with the external environment, $\dot{q}_{ext}$. A Fourier boundary condition is assumed, defined by constant values of the heat transfer coefficient, h_{ext}, and temperature, T_{ext}, such that $\dot{q}_{ext} = h_{ext} (T - T_{ext})$ (illustrated in Figure 1S1). A simplified global heat balance can thus be derived considering constant values for the volumetric enthalpy of fusion, L, and the volumetric heat capacity, C_p :

$$C_p \frac{dT}{dt} - L \left(\frac{d}{dt}(g^s+g^e) \right) = \frac{A}{V} h_{ext} (T - T_{ext}) \qquad (12)$$

where T is the time-dependent temperature of the system, and $g^s=g^{s^{(1)}}+g^{s^{(2)}}$ and $g^e=g^{e^{(2)}}+g^{e^{(3)}}$ are the volume fractions of the dendritic and eutectic structures ($g^s+g^e=1-g^l$ with $g^l=g^{l^{(0)}}+g^{l^{(1)}}$).

iv- *Alloy.* The model is applied to binary alloys. Subscript "i" in equations (2) and (8)-(10) can thus be omitted. A linear monovariant line of the phase diagram is assumed, that separates the fully liquid region from its mixture with the primary solid s. The value of its slope, m_L, is computed for each alloy considering the value of the eutectic temperature, T_E, the eutectic composition, w_E, the liquidus temperature of the alloy read on the phase diagram, T_L, and the nominal composition of the alloy, w_0, using $m_L=(T_E-T_L)/(w_E-w_0)$. A constant segregation coefficient, k, is also used, that links the equilibrium liquid and solid compositions within the mixture. A similar linear monovariant line approximation is used to separate the fully liquid region from its mixture with the primary hypereutectic solid, s', with slope denoted m'_L.

v- *Nucleation.* The nucleation temperature of the dendritic structure, $T_N^s = T_L - \Delta T_N^s$, is defined with respect to the liquidus temperature of the alloy, T_L, by a prescribed nucleation undercooling, ΔT_N^s. The same is done for the eutectic structure using the eutectic temperature, T_E, thus defining $T_N^e = T_E - \Delta T_N^e$. Nucleation of all structures takes place at the center of the domain.

vi- *Growth.* The dendritic structure propagates as $s^{(1)}$ into the extradendritic liquid $l^{(0)}$ by radial growth. The position of the dendrite tips, $R^{s^{(1)}l^{(0)}}$, defines the envelope of the mushy zone. It is calculated by integration over time of the velocity of the dendrite tips, $\overline{v_n^s} = \overline{v_n^{s^{(1)}l^{(0)}}}$, that relates to the supersaturation, Ω, via the Kurz et al. model [14]:

$$\overline{v_n^s} = \frac{D^l m_L (k-1) \overline{w^{l^{(1)}s^{(1)}}}}{\pi^2 \Gamma} \left(Iv^{-1}(\Omega) \right)^2 \tag{13a}$$

$$\Omega = [\overline{w^{l^{(1)}s^{(1)}}} - \langle w^{l^{(0)}} \rangle^{l^{(0)}}] / [\overline{w^{l^{(1)}s^{(1)}}} (1-k)] \tag{13b}$$

where Γ is the Gibbs-Thomson coefficient defined with respect to the primary solid phase s and Iv is the Ivantsov function. Radial propagation is also assumed to take place for the interdendritic and extradendritic eutectic structures at velocity $\overline{v_n^e} = \overline{v_n^{e^{(2)}l^{(1)}}} = \overline{v_n^{e^{(3)}l^{(0)}}}$. The position of the interfaces between the eutectic and the liquid, labeled $R^{e^{(2)}l^{(1)}}$ and $R^{e^{(3)}l^{(0)}}$ during steps (S2) and (S3) of Figure 1 is deduced from the integration over time of the Jackson and Hunt kinetics model [15]:

$$\overline{v_n^e} = \Delta T^2 / (4 K_r K_c) \tag{14a}$$

$$\lambda^2 \overline{v_n^e} = K_r / K_c \tag{14b}$$

$$\lambda \Delta T = 2 K_r \tag{14c}$$

$$K_c = \left[C' / (2 \pi D^l) \right] \left| m_L \right| \left| m_L' \right| / \left[\left| m_L \right| + \left| m_L' \right| \right] \tag{14d}$$

$$K_r = \left[2(1-f) \left| m_L' \right| \Gamma \sin(\theta) + 2f \left| m_L \right| \Gamma' \sin(\theta') \right] / \left[f(1-f) \left[\left| m_L \right| + \left| m_L' \right| \right] \right] \tag{14e}$$

where C' is the difference in composition between the ends of the eutectic tie-line, f is the fraction of the primary solid phase s in the eutectic structure (e is made of a mixture of the s and s' phases), Γ' is the Gibbs-Thomson coefficient defined with respect to the solid phase s', and θ and θ' are the contact angle between the s and s' solid phases and the liquid, respectively.

vii- *Mass transfers*. No mass exchange takes place with the external environment at the limit of the domain. The last term in the left-hand-side of Equation (8), $\nabla \cdot \langle \mathbf{j}_i^\alpha \rangle$, describes a macroscopic diffusion. It is neglected because its magnitude is much smaller than the mass transfer of solute due to diffusion fluxes created at interface between phases, i.e. the last term on the right-hand-side of Equation (8). Only a few interfaces are active for interfacial mass transfers, as listed hereafter and summarized in Table 1.

- During (S1) and (S2), the interdendritic liquid, $l^{(1)}$, exchanges solute with both the dendritic structure, $s^{(1)}$, and the extradendritic liquid, $l^{(0)}$. The interdendritic liquid composition, $\langle w^{l^{(1)}} \rangle^{l^{(1)}}$, is uniform and equal to the interfacial liquid composition $w^{l^{(1)}s^{(1)}}$.
- The eutectic structure exchanges mass upon its growth in the interdendritic liquid $l^{(1)}$ during (S2) and in the extradendritic liquid $l^{(0)}$ during (S3). The average interface composition at which the eutectic structure forms is equal to the average liquid composition in which it grows, $w^{e^{(2)}l^{(1)}} = \langle w^{l^{(1)}} \rangle^{l^{(1)}}$ and $w^{e^{(3)}l^{(0)}} = \langle w^{l^{(0)}} \rangle^{l^{(0)}}$. No diffusion fluxes are considered with the eutectic structures.
- All other exchanges either due to diffusion and/or movement are neglected for interfaces $s^{(1)}l^{(0)}$, $s^{(2)}e^{(3)}$, $s^{(2)}e^{(2)}$, $s^{(1)}s^{(2)}$ and $e^{(2)}e^{(3)}$ for all steps. Note that interfaces $e^{(2)}l^{(0)}$, $s^{(2)}l^{(0)}$, $s^{(2)}l^{(1)}$, $e^{(3)}l^{(1)}$, $e^{(2)}s^{(1)}$, $e^{(3)}s^{(1)}$ have no meaning in the various steps defined (Figure 1).

viii- *Equilibrium.* Thermodynamic equilibrium is assumed at the $s^{(1)}l^{(1)}$ interface. Interface compositions in the solid and in the liquid, respectively $w^{s^{(1)}l^{(1)}}$ and $w^{l^{(1)}s^{(1)}}$, are linked by the segregation coefficient, $w^{s^{(1)}l^{(1)}} = k\, w^{l^{(1)}s^{(1)}}$.

ix- *Properties*. The densities are assumed to be equal and constant. Similarly, the volumetric enthalpy of fusion, L, and the volumetric heat capacity, C_p.

II.3.5 Numerical solution

Mathematical expressions for the mass conservations, Equations (7)-(11), together with the global heat balance, Equation (12), and the growth kinetics, Equations (13) and (14), are to be completed by the geometrical definitions of the interfacial area concentrations and by the diffusion lengths. The expressions used are listed in Table 1 and 2. Note that the interfacial area concentrations are dependent on steps (S0)-(S4), thus permitting a general writing of the equations valid for the entire solidification sequence. With the introduction of all other assumptions listed above, the system of equation is solved using the Gear method and an iterative algorithm.

II.4 Result

II.4.1 Experimental

The grey dots in Figure 2 present the recorded temperature history for the three samples solidified under electromagnetic levitation. Despite the noise that is inherent to the pyrometer technology used at low temperature as well as to the translations and rotations of the levitated samples, two reheatings are clearly observed on each cooling curve, referred to as recalescences. Considering the phase diagram and micrographic cross sections, these recalescences are interpreted as the signal for the formation of a primary dendritic structure, s, and a secondary eutectic structure, e. They are due to sudden partial releases of the enthalpy of fusion. The samples temperature increases because of the limited heat extraction rate throughout the surface of the droplet. The times for the beginning of these recalescences are labeled t_N^s and t_N^e in Figure 2. Because of the abrupt change of sign and high heating rate shortly after these times, fast growth of the structures is expected. Indeed, in case of nucleation at the equilibrium temperature, growth is slow and the cooling curve exhibits a more progressive change of the curve slope [4]. It is thus concluded that the temperatures read at times t_N^s and t_N^e, respectively T_N^s and T_N^e, also correspond to the nucleation temperature of the structures. They are respectively identified in Figure 2 with a red crossed square symbol and a red crossed circle symbol corresponding to the undercoolings $\Delta T_N^s = T_L - T_N^s$ and $\Delta T_N^e = T_E - T_N^e$ with respect to the liquidus temperature of the alloy, T_L, and the eutectic temperature, T_E. The end of solidification, t_{end}, is read in Figure 2 as the last characteristic time at which a significant slope change is observed in the cooling curve. All these measured data are listed in Table 3 as undercooling and solidification times from the nucleation events of the dendritic and eutectic structures.

Other measurements on each curve are the cooling rates just before and after solidification, respectively $\dot{T}(t<t_N^s)$ and $\dot{T}(t>t_{end})$. The cooling history, also listed in Table 3, is indeed required for the adjustment of the heat extraction rate due to energy transfer with the external environment. The procedure consists of determining the best fit for the heat transfer coefficient, h_{ext}, entering Equation (12), the solution of which is simply $[T(t) - T_{ext}] = [T_0 - T_{ext}] \exp [- h_{ext} (C_p R/3)^{-1} (t - t_0)]$ in the approximation of no phase transformation. In the later expression, T_0 is the initial temperature at the beginning of the time interval considered for adjustment of the heat transfer coefficient, t_0. Values for the heat transfer coefficient prior and after solidification, respectively $h(t<t_N^s)$ and $h(t>t_{end})$, are thus determined using the cooling history extracted in a small time interval (typically one second) before and after solidification.

Figure 3.c1 presents measurements of Cu composition conducted on the meridian cross section of three droplets. Results are drawn as distribution maps of a normalized Cu content using local values averaged over $120 \cdot 10^{-6}$ m × $150 \cdot 10^{-6}$ m rectangles, thus encompassing several times the dendrite arm spacing. Global averaging over the entire measurements for each sample leads to the values listed in Table 4 as w_D. It shows a deviation from the nominal composition, $\left|(w_D - w_0)/w_0\right|$, that varies from +3.5% for the 4 wt% Cu to -13.75% for the 24 wt% Cu. The main possible reason for these deviations is the fact that the development of the structures associated with the formation

of segregation does not take place within a symmetry plane or with a symmetry axis defined with respect to the central meridian cross sections analyzed. Indeed no indication could be given to decide for a particular cut throughout the droplets and it is even not clear if symmetry could have been defined due to the anisotropic growth morphology associated with the dendritic structure. The normalization applied in the representation of the average composition map, $(w-w_0)/w_0$, identifies the regions with negative and positive deviations with respect to the nominal composition, revealing a macrosegregation taking place at the scale of the samples. Note that because of the deviation of the average composition measured with respect to the nominal composition for alloys 14 wt% Cu and 24 wt% Cu, a general negative segregation is observed in Figure 3.c1.l2 and 3.c1.l3.

The distribution maps of the volume fraction of the eutectic structure deduced from image analyses are shown in Figure 3.c2. Representations include a normalization using the value of the volume fraction of the eutectic structure predicted by the Gulliver-Scheil solidification path of each alloy, g^e_{GS}. These values are taken equal to the volume fraction of liquid remaining at the eutectic temperature, $g^l_{GS}(T_E)=(w_E/w_0)^{-1/(1-k)}$, when considering a mass balance with no diffusion in the solid and complete diffusion in the liquid [17]. Results of calculations listed in Table 4 are deduced from phase diagram data given in Table 5. Justification for this normalization is given by earlier work on segregation [18]. Values for the average eutectic fraction over the entire domain, g^e_D, are also listed in Table 4. Note that the representation in Figure 3.c2, $(g^e-g^e_{GS})/g^e_{GS}$, permits a direct visualization of the deviation with respect to the Gulliver-Scheil prediction. In order to check the validity of the distribution maps for the eutectic fraction, X-ray tomography was conducted at the European Synchrotron Radiation Facility. This method offers the possibility to access a three-dimensional view of the structure by the assembly of a stack of two-dimensional images acquired every 0.3 μm [19]. Using a representative elementary cubic volume moved in the three-dimensional representation of the dendritic structure below the actual cross sections, a distribution map was also deduced for the volume fraction of the interdendritic area, i.e. the eutectic structure. Very similar distributions of the eutectic structure were obtained, thus validating the two-dimensional analysis within the central meridian cross sections presented in Figure 3.c2.

The ratio g^e_D/g^e_{GS} is calculated in Table 6. It is observed that the ratio decreases and thus deviation from the Gulliver-Scheil prediction increases when decreasing the nominal composition of the alloy. This is indeed retrieved in the distribution maps since Figure 3.c2.l1 presents more surface areas with negative normalized eutectic fraction. This result will be discussed later in light of simulation results using the new model developed.

The DAS is shown in Figure 3.c3 with a global average value given in Table 4. While the same scale is used for all alloys, no simple normalization can be applied. It is clearly seen that the variation of the size distribution is narrower when increasing the alloy composition.

An interesting observation to point out when considering all maps drawn on a single line in Figure 3.l1 to 3.l3 (i.e., for a given alloy composition) is a systematic correlation between the

distributions of copper, the eutectic fraction and the dendrite arm spacing. For instance, locations where the average composition is higher in Figure 3.c1.l2 correspond to a higher fraction of eutectic in Figure 3.c2.l2. While this was already mentioned by Heringer et al. [6], no systematic measurements were clearly presented. Similarly, locations with higher average composition in Figure 3.c1.l2 correspond to smaller dendrite arm spacing in Figure 3.c3.l2. A simple composition dependent coarsening model is able to predict the later observation [17]. These observations are also supported by the global averages presented in Table 4.

II.4.2 Prediction

All data needed for simulations are given in Table 5 and 6 (measured nucleation undercooling). Additional information is the dendrite arm spacing entering in the expression of the diffusion length $l^{s^{(1)}l^{(1)}}$ given in Table 2. Its value is taken constant using the average value measured over the entire surface analyzed, DAS_D (Table 4). Typical results of a simulation are shown in Figure 2b and in Figure 4 for the Al-14wt%Cu alloy. The predicted solidification time in Figure 2b shows an excellent agreement with the measurements. This is the result of the adjustment of the heat transfer coefficient to fit the measured cooling rate prior to nucleation of the primary dendritic structure, $h(t<t_N^s)$.

Time evolutions of the volume fractions of all structures and liquid phases are given in Figure 4. The five steps illustrated in Figure 1 are identified as S0-S4 in Figure 4. The prediction during steps S0 and S1 are common to previous models [1-3]. All other curves represent the predicted evolution of additional features, such as the primary dendritic solid retained within the fully solid envelope of the grain, $s^{(2)}$, and the inter- and extradendritic eutectics, respectively $e^{(2)}$ and $e^{(3)}$. Figure 4.c also presents the time evolution of the average compositions of the liquids and of the dendritic and eutectic structures. Step S1 starts after the nucleation of the primary dendritic structure at temperature $T_N^s = T_L$ - 15 K with the development of the mushy zone. As a result, the volume fraction of the extradendritic liquid, $g^{l^{(0)}}$, decreases rapidly (Figure 4.a). It is replaced by the volume fraction of the liquid located in the mushy zone, i.e. the interdendritic liquid, $g^{l^{(1)}}$. The global volume fraction of the liquid, $g^l=g^{l^{(0)}}+g^{l^{(1)}}$, is also represented. It naturally decreases with time since it is replaced by the formation of the primary dendritic solid formed in the mushy zone as can be seen in Figure 4.b by the increase of $g^{s^{(1)}}$. Note that the curves in Figure 4.a and 4.b are complementary during step S1 with $g^{s^{(1)}}+g^{l^{(1)}}+g^{l^{(0)}}=1$. The growth kinetics of the mushy zone envelop is given by Equation (13a). It is proportional to the supersaturation given by Equation (13b) where $w^{l^{(1)}s^{(1)}} - \langle w^{l^{(0)}} \rangle^{l^{(0)}} = \langle w^{l^{(1)}} \rangle^{l^{(1)}} - \langle w^{l^{(0)}} \rangle^{l^{(0)}}$ according to the first assumption *vii-* of the model. The difference between the two compositions is easily visualized in Figure 4.c. It rapidly decreases after the nucleation to vanish at around 15 s. At the same time, $g^{l^{(0)}}$ almost stops to decrease as shown in Figure 4.a since the volume fraction of the extradendritic liquid is complementary to that of the mushy zone. Figure 2b shows that this time also corresponds to the maximum temperature reached upon recalescence. The temperature then decreasing, the liquid composition increases and solidification proceeds further.

Step S2 starts upon nucleation of the eutectic structure at temperature $T_N^e = T_E - 20$ K. The volume fraction of both the dendritic structure inside the solid envelop defined by the eutectic front, $g^{s^{(2)}}$, and the eutectic structure, $g^{e^{(2)}}$, increase, while the volume fraction of the dendritic structure inside the mushy zone, $g^{s^{(1)}}$, decreases. The later effect is due firstly to the transfer of structure s^1 to s^2 due to the geometrical development of the solid core, but also to remelting taking place inside the mushy zone. It is interesting to note that upon the development of the eutectic structure, the recalescence modeled that is visible in Figure 2b leads to a decrease of the interdendritic liquid composition. Not only this phenomenon explains remelting observed in the mushy zone, but also it leads to a transfer of solute from outside the mushy zone, $\langle w^{l(0)} \rangle^{l(0)}$ becoming larger than $\langle w^{l(1)} \rangle^{l(1)}$ as shown in Figure 4c. It has been chosen that the resultant negative supersaturation predicted by Equation (13b) should be used to calculate a negative velocity of the growth front. This is done using the absolute value of the supersaturation introduced in Equation (13a) and changing the sign of the calculated velocity. While this is probably a crude approximation for the remelting kinetics of a mushy zone growth front, it is compatible with the general remelting situation observed. Consequence is visible in Figure 4a where the extradendritic liquid increases slightly during Step S2. The eutectic structure e^2 having reached the position of the mushy zone growth front, it then propagates in the extradendritic liquid as e^3 upon Step S3. This is visible in Figure 2b with the increase of $g^{e^{(3)}}$ while all other solid structures are blocked since no solid phase transformation is activated. One can observe in Figure 4c that the average composition of the primary dendritic structure averaged using the volume fraction s^2 and s^3 systematically decreases upon recalescences. This is mainly piloted by equilibrium at interfaces. Similarly, since the eutectic structures are formed with an average composition taken equal to the liquid composition in which it develops, the recalescence following eutectic growth leads to a decrease of the its composition.

II.5 Discussion

As mentioned in the captions of Figure 2b and 4, the simulation results presented into details for the Al-14wt%Cu alloy correspond to the case for which diffusion in the solid phase is accounted for ($D^s \neq 0$) as well as the nucleation undercooling measured for both the dendritic and the eutectic structures, i.e. $\Delta T_N^s = 15$ K and $\Delta T_N^e = 20$ K, together with recalescences due to the growth of both the dendritic and eutectic structures. The resulting normalized volume fraction of eutectic, g^e/g^e_{GS}, reaches 0.91 as is reported in bold in Table 6. Comparisons with the results for other calculations presented in Table 6 put more light on the individual role of the parameters of the model.

When nil values for the undercoolings of both the primary dendritic and the eutectic structures are used ($\Delta T_N^s = 0$ K and $\Delta T_N^e = 0$ K), together with no diffusion in the solid ($D^s = 0$), an isothermal eutectic transformation at $T_N^e = T_E$ retrieves the prediction of the Gulliver-Scheil equation ($g^l(T_N^e)/g^e_{GS} = 1.00$ in Table 6 c1.l5 for the Al-14 wt% Cu alloy). The effect of diffusion in the solid phase alone is isolated by reading the next line of the same column ($\Delta T_N^s = 0$ K, $\Delta T_N^e = 0$ K, $D^s \neq 0$, Table 6 c1.l6) leading to $g^l(T_N^e)/g^e_{GS} = 0.97$. This analysis is comparable with classical solid diffusion models common in the literature [17]. The effect of accounting for the primary nucleation undercooling measured is accessible in the next column ($\Delta T_N^s = 15$ K, $\Delta T_N^e = 0$ K, Table 6 c2.l5-6). Effect is so weak that it is hidden by the two digits format of the numbers chosen for Table 6, thus retrieving the results of the previous column (compare Table 6 c1.l5-6 with Table 6 c2.l5-6). The effect of shifting the eutectic transformation to the measured nucleation undercooling prior to the second recalescence measured while keeping an isothermal treatment of the eutectic transformation is also isolated in the next column ($\Delta T_N^s = 0$ K, $\Delta T_N^e = 20$ K, Table 6 c3.l5-6). Value for the predicted normalized fraction significantly decreases to 0.84 when neglecting solid state diffusion ($D^s = 0$, Table 6 c3.l5) and 0.81 otherwise ($D^s \neq 0$, Table 6 c3.l6). This is due to a longer time to solidify the dendritic mushy zone up to a lower temperature, leaving less liquid available for the eutectic transformation. Again, adding the effect of the primary undercooling ($\Delta T_N^s = 15$ K, $\Delta T_N^e = 20$ K, Table 6 c4.l5-6) almost does not affect the remaining liquid fraction at the isothermal eutectic temperature (compare Table 6 c3.l5-6 with Table 6 c4.l5-6).

Predictions with the new model are shown in the next two lines as g^e/g^e_{GS} (Table 6 l7-8). Nucleation and growth of the eutectic structure is then considered. Upon growth of the secondary phase e^2, as explained above by the detailed presentation of the curves in Figure 4, remelting of the primary solid phase located in the mushy zone, s^1, takes place. This is mainly due to the recalescence and the adjustment of the interdendritic liquid composition, l^1, to the actual temperature. As a result, more liquid is available for the formation of eutectic, leading to a higher value of the ratio g^e/g^e_{GS} for similar other parameters. For instance, by isolating the sole effect of the nucleation undercooling of the eutectic structure, g^e/g^e_{GS} reaches 0.95 ($\Delta T_N^s = 0$ K, $\Delta T_N^e = 20$ K, $D^s = 0$, Table 6 c3.l7) compared to 0.84 with an isothermal eutectic transformation ($\Delta T_N^s = 0$ K, $\Delta T_N^e = 20$ K, $D^s = 0$, Table 6 c3.l5). The effect of the growth of the eutectic structure when no undercooling is considered is also of interest. The ratio increases to $g^e/g^e_{GS} = 0.97$ ($\Delta T_N^s = 0$ K,

$\Delta T_N^e = 0$ K, $D^s = 0$, Table 6 c1.l7), showing a global effect of the same order of magnitude as the diffusion alone ($\Delta T_N^s = 0$ K, $\Delta T_N^e = 0$ K, $D^s \neq 0$, Table 6 c1.l6). Addition of solid diffusion plus the growth of the eutectic leads to $g^e/g^e_{GS} = 0.93$ when no nucleation undercooling is considered ($\Delta T_N^s = 0$ K, $\Delta T_N^e = 0$ K and $D^s \neq 0$, Table 6 c1.l8), to be compared with $g^e/g^e_{GS} = 0.91$ when using the measured nucleation undercooling ($\Delta T_N^s = 0$ K, $\Delta T_N^e = 20$ K and $D^s \neq 0$, Table 6 c3.l8). Effect of the primary nucleation undercooling is again found very limited (compare Table 6 c2.l7-8 with c1.l7-8 and c4.l7-8 with c3.l7-8).

Table 6 gathers the predictions of the normalized volume fractions of eutectic for the three Al-Cu alloys considering the same type of variations of the parameters presented above. Please note that using the constant value $h_{ext} = h(t<t_N^s)$ given in Table 6 for the 4 wt% Cu sample leads to the dashed cooling curve shown in Figure 2a. Discrepancy was interpreted by a strong evolution of the heat transfer coefficient during solidification as shown by the cooling rates $\dot{T}(t<t_N^s)$ and $\dot{T}(t>t_{end})$ reported in Table 3. Using the adjusted value at $h(t>t_{end})$ and averaging h_{ext} with the volume fraction of liquid, $h_{ext} = g^l\, h(t<t_N^s) + (1-g^l)\, h(t>t_{end})$, reaches a better agreement with the recorded cooling curve as is shown by the plain curve in Figure 2a. Explanation could invoke the role of electromagnetic levitation on the heat extraction rate as a function of the fraction of the liquid phase.

The same procedure tempted on the two other samples was not successful and a constant heat transfer coefficient was consequently kept. Since the main objective of the model is not to retrieve the exact heat boundary condition between the metal and the atmosphere, this difference of the procedure to evaluate the heat extraction rate is of minor importance. The predicted cooling curve in Figure 2c also shows a longer solidification time than the measurement for the 24 wt% Cu sample. Additional duration with respect to the measurement corresponds to the formation of structure $e^{(3)}$ into liquid $l^{(0)}$. Indeed, propagation of eutectic $e^{(2)}$ ends soon after its nucleation for this alloy. This can be tracked by the small hook visible when the predicted cooling curve almost reaches the eutectic temperature. Attempt to improve the simulation by adjusting the heat extraction rate during the propagation of $e^{(3)}$ could have been carried out. However, since the final eutectic structure is modeled to develop with no effect on the volume fraction of all other phases, this would have had no effect on the final prediction of the volume fraction of phases.

The role of diffusion in the solid is of minor effect when increasing the alloy composition. For instance, its isolated effect leads to a remaining liquid at $T_N^e=T_E$ equal to $g^l(T_N^e)/g^e_{GS} = 0.88$ for the 4 wt% Cu alloy ($\Delta T_N^s = 0$ K, $\Delta T_N^e = 0$ K and $D^s \neq 0$, Table 6 c1.l2), compared to $g^l(T_N^e)/g^e_{GS} = 0.99$ for the 24 wt% Cu alloy ($\Delta T_N^s = 0$ K, $\Delta T_N^e = 0$ K and $D^s \neq 0$, Table 6 c1.l10). Similarly, taking into account the effect of the nucleation and growth of the eutectic structure alone with $T_N^e=T_E$ has a more pronounced effect for the low composition alloy. While $g^e/g^e_{GS} = 0.90$ for the 4 wt% Cu alloy ($\Delta T_N^s = 0$ K, $\Delta T_N^e = 0$ K and $D^s = 0$, Table 6 c1.l3), it increases to $g^e/g^e_{GS} = 0.98$ for the 24 wt% Cu alloy ($\Delta T_N^s = 0$ K, $\Delta T_N^e = 0$ K and $D^s = 0$, Table 6 c1.l11). Accumulation of the solid diffusion together with the nucleation and growth of the eutectic structure nucleation at $T_N^e=T_E$ is observed,

leading to $g^e/g^e_{GS} = 0.77$ for the 4 wt% Cu alloy ($\Delta T^s_N = 0$ K, $\Delta T^e_N = 0$ K and $D^s \neq 0$, Table 6 c1.l4) and $g^e/g^e_{GS} = 0.97$ for the 24 wt% Cu ($\Delta T^s_N = 0$ K, $\Delta T^e_N = 0$ K and $D^s \neq 0$, Table 6 c1.l12). It is interesting at this point to point out the fact that, considering no nucleation undercoolings, the effect of solid diffusion is systematically of the same order of magnitude as the effect of the eutectic nucleation and growth, while almost no effect is seen due to the nucleation and growth of the primary structure. This result is of prime interest when put into perspective with a literature review. Indeed, segregation studies have mainly focused on the effect of solid diffusion and have been developed to account for recalescence due to primary solidification, while no model accounts for the effect of eutectic recalescence on the final distribution of structures. The later effect is yet believed to be of prime importance according to the predictions of Table 6 when studying the solidification path of equiaxed grain structures.

Considering the measured value of the primary nucleation undercoolings confirms an insignificant role (compare Table 6 c2.l1-12 with Table 6 c1.l1-12 as well as compare Table 6 c4.l1-12 with Table 6 c3.l1-12, i.e. for all alloys, with and without diffusion on the primary solid phase, with and without eutectic recalescence). While accounting for the measured value of the nucleation undercooling of the eutectic is found to be the most effective way to decrease the eutectic fraction for all alloys, a distinction can be made when increasing the alloy composition. The duration of the eutectic transformation increases with the amount of eutectic and thus with the alloy composition. This is clearly seen by comparing Figure 2a and c. In Figure 2a the eutectic transformation is very rapid since little liquid remains in the mushy zone. As a consequence, the eutectic recalescence is limited and almost no remelting of the primary solidified dendritic structure takes place. The consequence is a ratio g^e/g^e_{GS} equal to $g^l(T^e_N)/g^e_{GS}$ in Table 6 (compare c4.l4 with c4.l2). The situation is different for higher composition as seen in Figure 2c and when comparing predictions in Table 6 c4.l12 with Table 6 c4.l10). The observation detailled for the 14 wt% Cu alloy in Figure 4 is retrieved, leading to $g^l(T^e_N)/g^e_{GS} < g^e/g^e_{GS} < g^l(T_E)/g^e_{GS}$ (in Table 6, c4.l6 < c4.l8 < c2.l6).

Comparison of the predicted values, g^e/g^e_{GS}, with the measurements, g^e_D/g^e_{GS}, is also possible owing to the numerical values given in Table 6. Predictions for the Al-4wt%Cu alloy and the Al-24wt%Cu are very good (compare Table 6 c4.l4 with $g^e_D/g^e_{GS} = 0.72$ and Table 6 c4.l12 with $g^e_D/g^e_{GS} = 0.85$). In the case of the Al-24wt%Cu, the eutectic recalescence following the undercooling of the interdendritic liquid below the eutectic temperature is found to be the most important parameter in modeling of segregation during solidification. For the Al - 4 wt% Cu alloy, recalescence has little effect. The reason is the very short duration of the eutectic transformation. The model then simply converges toward the prediction of a standard segregation analysis that is extended up to the nucleation temperature of the eutectic structure. The largest deviation between experiment and modeling is found for the Al-14wt%Cu sample since the simulation reaches to $g^e/g^e_{GS} = 0.91$ (Table 6 c4.l8) while the measurement gives $g^e_D/g^e_{GS} = 0.82$. This is yet a satisfactory result when considering the several approximations made and the sources of errors in the measurement.

II.6 Conclusion

The following list of achievements and findings summarizes the work presented:

- Droplets with $5.3 \cdot 10^{-3}$ m diameter made of aluminum - copper (Al-Cu) alloys with compositions 4, 14 and 24 wt% Cu were solidified using electromagnetic levitation. *In-situ* measurement of the temperature evolution was measured during processing (Figure 2 and Table 3). Characterization also includes distribution maps of the average local Cu content, the dendrite arm spacing and the fraction of the eutectic structure drawn in a central meridian cross section (Figure 3). Averaging over the entire cross section leads to global average values (Table 4). EML processing of metallic alloys coupled with detailed characterization is found to be a suitable experimental technique to study segregation and solidification paths. In particular it permits to isolate a small sample that could be seen as a uniform system in temperature and it gives a direct access to the measurement of nucleation temperatures and recalescences that are important parameters for the comparison with simulations. While the distribution map can be used to quantify macrosegregation in the system, averaging over the entire cross section gives information on an average volume fraction of the eutectic structure. The latter information can be used together with the measured average dendrite arm spacing and temperature history to compare with the prediction of a microsegregation model.

- A one-dimensional isothermal microsegregation model was developed for the prediction of the evolution of volume fraction and average composition of the extradendritic liquid, $l^{(0)}$, the interdendritic liquid, $l^{(1)}$, the dendritic structure formed in the mushy zone, $s^{(1)}$, the dendritic structure retained in the solid zone, $s^{(2)}$, the interdendritic eutectic structure, $e^{(2)}$, and the extradendritic eutectic structure, $e^{(3)}$. The model takes into account the nucleation undercooling of the dendritic and eutectic structures, as well as for diffusion in the solid and liquid phases. It can be seen as an extension of previously developed models [2] where cooling of the liquid and solidification of the mushy zone is only one of the sequences considered. The three additional sequences include nucleation and growth of the interdendritic and extradendritic eutectic structures and cooling of the solid.

- The nucleation undercooling and recalescence upon growth of the eutectic structure plays a main role on the final volume fraction of phases present in the as-cast state. This main finding is of major relevance for casting processes of equiaxed structures.

Extension of the present microsegregation model is foreseen to model peritectic reaction and transformation as well as for integration in a non-isothermal numerical model including diffusion

and convection. Such a model should be able to predict the measured distributions of the average composition of copper (i.e. macrosegregation) in the presence of recalescences due to the nucleation and growth of several microstructures.

II.7 Acknowledgment

This work was conducted within a European Space Agency project of the Microgravity Applications Promotion program (contract 15236/02/NL/SH). Contributions from J. Brogly, B. Crozier, Y. C. Chung, S. Jacomet, B. Triger and M. Repoux are acknowledged.

II.8 Reference

[1] Rappaz M., Thévoz Ph. Acta Metallurgica 1987; 35:2929.

[2] Wang C. Y., Beckermann C. Metallurgical Transactions A 1993; 24:2787.

[3] Wang C. Y., Beckermann C. Materials Science and Engineering A 1993; 171:199.

[4] Grong Ø., Dahle A. K., Onsøien M. I., Arnberg L. Acta Materialia 1998; 46:5045.

[5] Nielsen O., Appolaire B., Combeau H., Mo A. Metallurgical and Materials Transactions A 2001; 32:2049.

[6] Heringer R., Gandin Ch.-A., Lesoult G., Henein H. Acta Materialia 2006; 54:4427.

[7] Herlach D. M., Annual Review of Materials 1991; 21:23.

[8] Volkmann T., Herlach D. M.. Steel Research Int. 2007; 78:426.

[9] Löser W., Shuleshova O., Lindenkreuz H.-G., Büchner B. Proceedings of the 5th Decennial International Conference on Solidification Processing 2007; 277. Ed. H. Jones. The University of Sheffield, U. K.

[10] Wunderlich R. K., Battezzati L., Baldissin D., Egry I., Etay J., Schmidt-Hohagen F., Novakovic R., Ricci E., Seetharaman S., Matsushita T., Fecht H.-J. Proceedings of the 5th Decennial International Conference on Solidification Processing 2007; 383. Ed. H. Jones. The University of Sheffield, U. K.

[11] Volkmann T., Herlach D. M., Lengsdorf R., Gandin Ch.-A. Chill Cooling for the Electromagnetic Levitator in Relation with Continuous Casting of Steel. Köln (D): internal DLR report, 2007.

[12] Abramoff M. D., Magelhaes P. J., Ram S. J. Biophotonics Inter. 2004; 11:36.

[13] Martorano M. A., Beckermann C., Gandin Ch.-A. Metallurgical and Materials Transactions A 2003; 34:1657, 2004; 35:1915.

[14] Kurz W., Giovanola B., Trivedi R. Acta Metallurgica 1986; 34:823.

[15] Jackson K. A., Hunt J. D. Transactions of the Metallurgical Society of the AIME 1966; 236:1129.

[16] Zimmermann M. Ph. D. Thesis 1990, Ecole Polytechnique Fédérale de Lausanne, CH.

[17] Kurz W., Fisher D. J. Fundamentals of Solidification. Aedermannsdorf (CH): Trans Tech Pub., 1998.

[18] Sarreal J. A., Abbaschian G. J. Metallurgical Transactions A 1986; 17:2063.

[19] Mosbah S., Gandin Ch.-A., Brogly J., Crozier B., Volkmann Th., Herlach D. Proceedings of the 5th Decennial International Conference on Solidification Processing 2007; 80. Ed. H. Jones. The University of Sheffield, U. K.

II.9 Figure

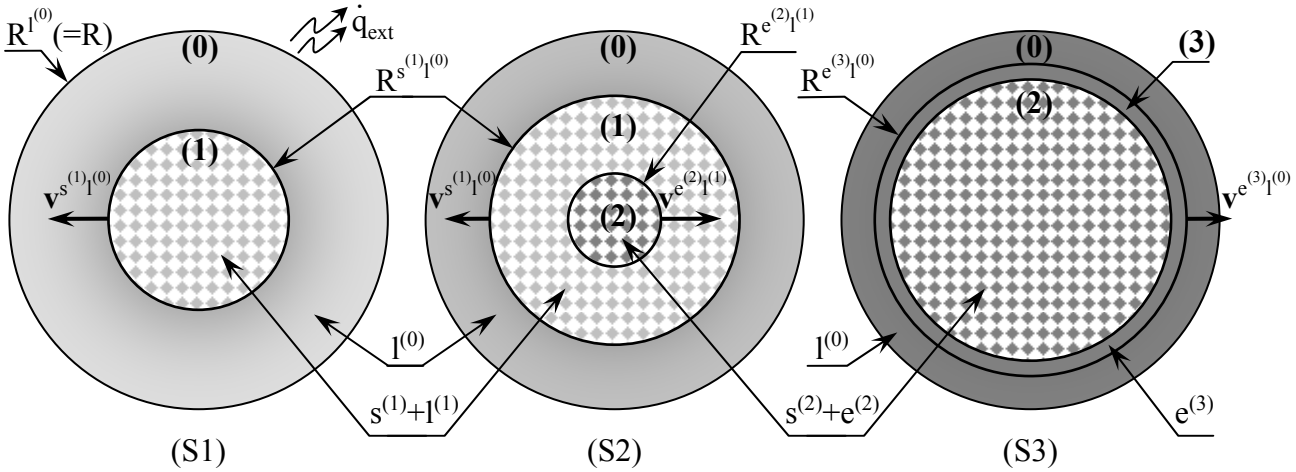

Figure 1: Schematized solidification sequence of a binary alloy in five steps denoted (S0) to (S4). (S0): cooling of the liquid, $l^{(0)}$ (not shown). (S1): growth of a mushy zone, (1), into the undercooled extradendritic liquid, $l^{(0)}$. The mushy zone is made of the dendritic structure, $s^{(1)}$ (white diamond-shaped pattern inside the central disk), plus the interdendritic liquid, $l^{(1)}$ (light grey diamond-shaped pattern inside the central disk). (S2): growth of an interdendritic eutectic structure, $e^{(2)}$ (dark grey diamond-shaped pattern inside the central disk), into the interdendritic liquid of the mushy zone, $l^{(1)}$. (S3): growth of the extradendritic eutectic structure, $e^{(3)}$ (dark grey layer surrounding the mixture $s^{(2)}+e^{(2)}$), into the remaining extradendritic liquid, $l^{(0)}$. (S4): cooling of the solid, $s^{(2)}+e^{(2)}+e^{(3)}$ (not shown). The outer boundary of regions (1) to (3) are delimited by its radius, $R^{s^{(1)}l^{(0)}}$, $R^{e^{(2)}l^{(1)}}$, $R^{e^{(3)}l^{(0)}}$, growing at velocity, $\mathbf{v}^{s^{(1)}l^{(0)}}$, $\mathbf{v}^{e^{(2)}l^{(1)}}$, $\mathbf{v}^{e^{(3)}l^{(0)}}$, respectively. The grey scale is proportional to the solute composition of the different structures.

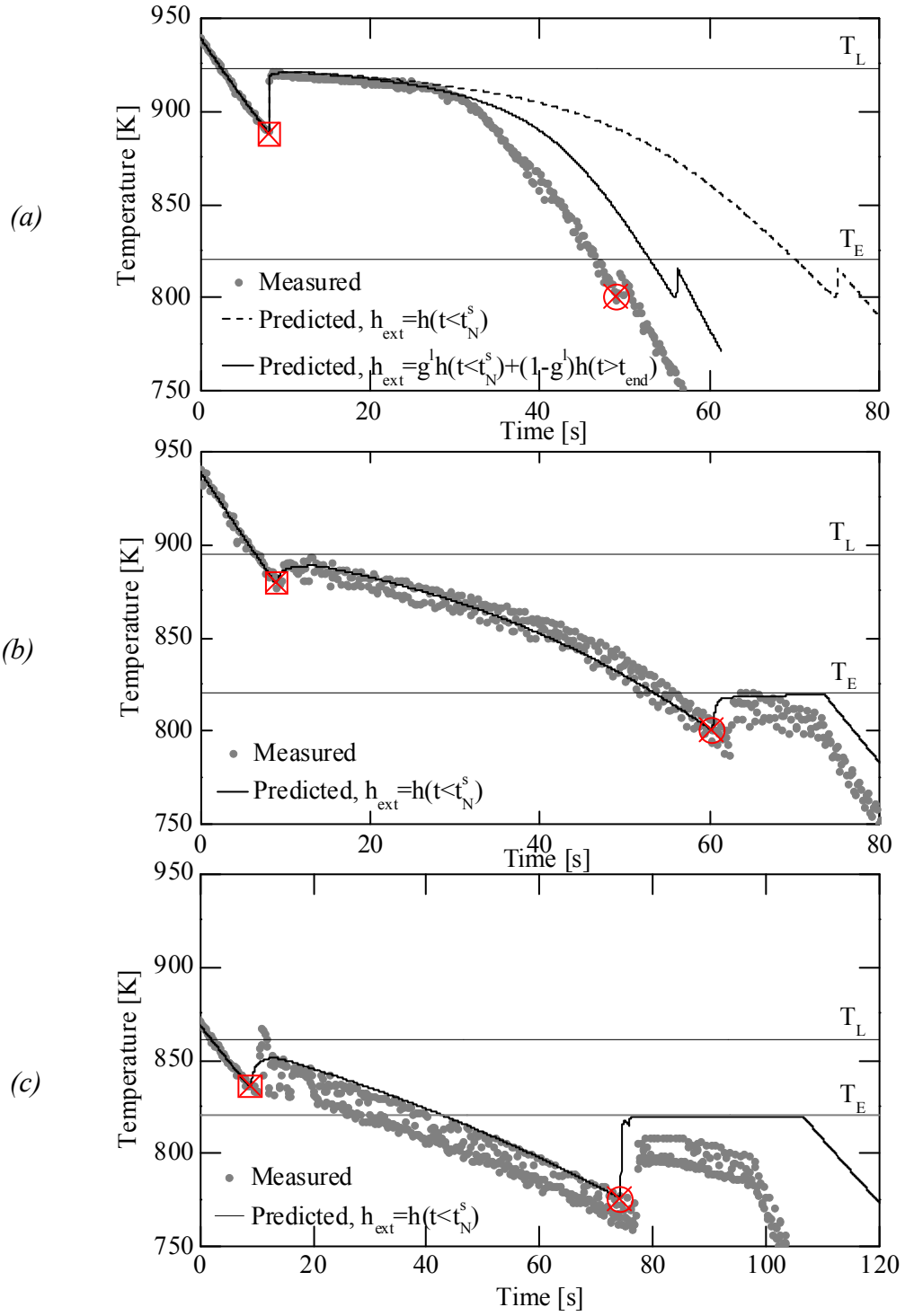

Figure 2: Simulated and measured cooling histories for the aluminum-copper samples processed by electromagnetic levitation. Nominal composition of the samples: (a) 4 wt% Cu, (b) 14 wt% Cu, (c) 24 wt% Cu. Calculations correspond to simulations with the new model using $\Delta T_N^s \neq 0$, $\Delta T_N^e \neq 0$ and $D^s \neq 0$. They lead to the normalized volume fraction of eutectic, g^e/g^e_{GS}, listed in bold in Table 6. Data for the simulations are given in Table 3, 4 and 5. Simulated curves correspond to heat transfer coefficients, h_{ext}, deduced from the cooling rate prior to nucleation, $h(t<t_N^s)$, and after completion of solidification, $h(t>t_{end})$, as explained in the text and in the caption of Table 5.

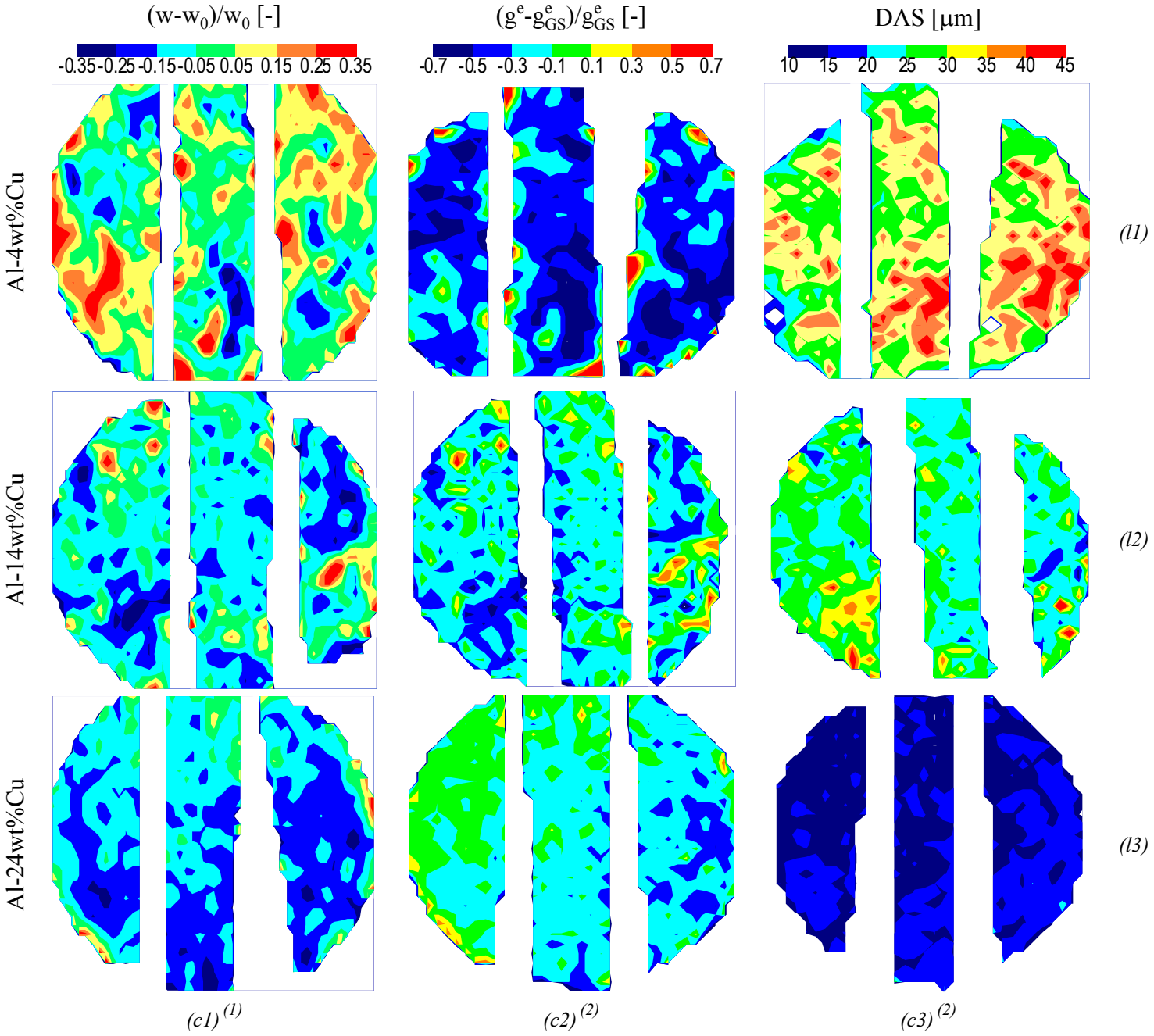

Figure 3: Characterization of a central meridian cross section of aluminum-copper samples processed by electromagnetic levitation. Distribution of (c1) the normalized average copper content, $(w-w_0)/w_0$ [-], (c2) the normalized average eutectic fraction, $(g^e-g^e_{GS})/g^e_{GS}$ [-] and (c3) the average dendrite arm spacing, DAS [µm]. Nominal composition of the samples: (l1) 4 wt% Cu, (l2) 14 wt% Cu, (l3) 24 wt% Cu. (1) Measurements of the average copper content, w, is average over $120\cdot10^{-6}$ m × $150\cdot10^{-6}$ m surface areas. (2) Measurements of the volume fraction of the eutectic structure, g^e, is average over $150\cdot10^{-6}$ m × $150\cdot10^{-6}$ m surface areas.

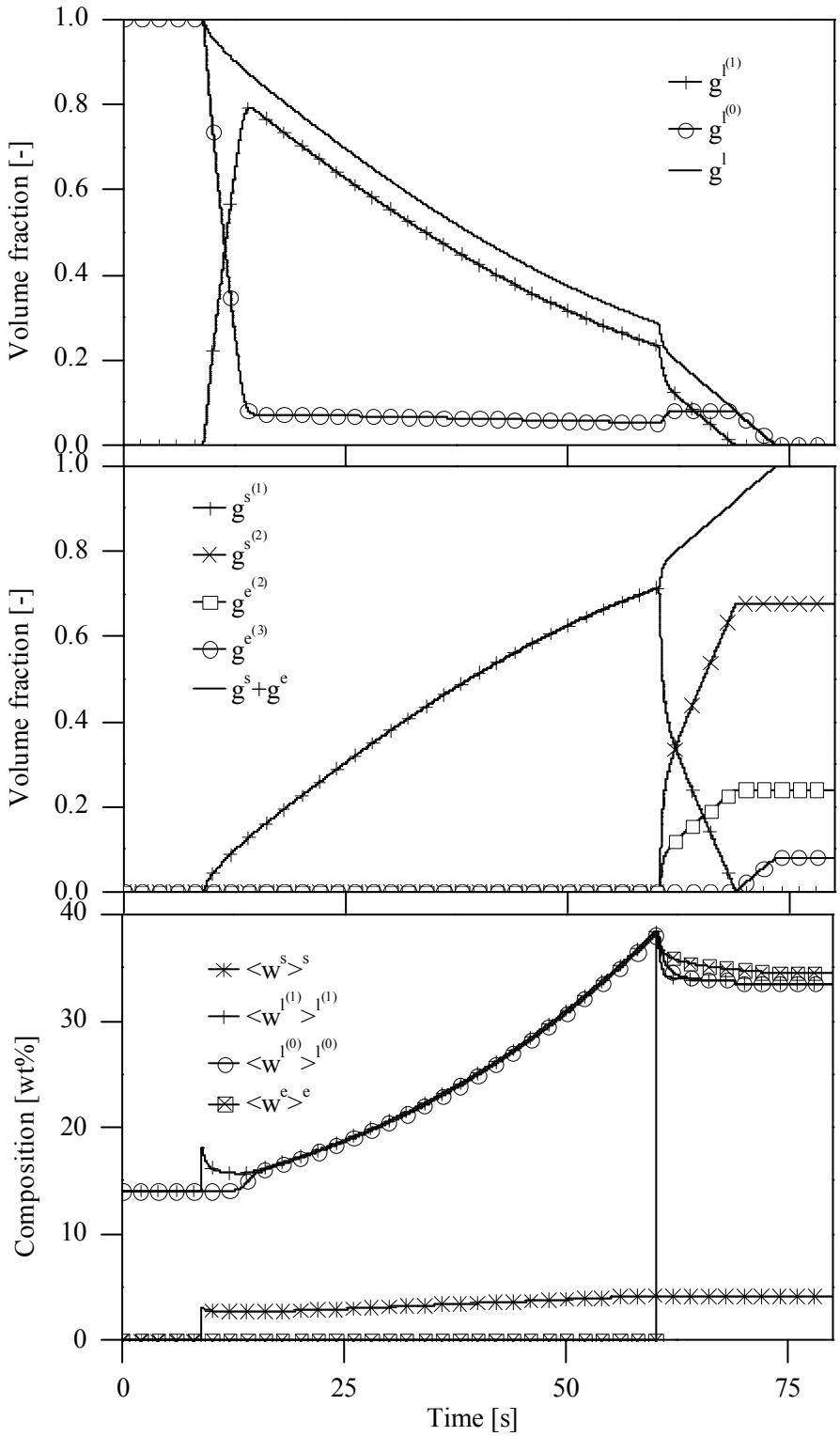

Figure 4: Detailed predictions for the Al-14wt%Cu droplet showing the time evolution of (a) the volume fractions of the extra- and interdendritic liquids, $g^{l^{(0)}}$ and $g^{l^{(1)}}$, as well as the sum of all liquids, $g^{l}=g^{l^{(0)}}+g^{l^{(1)}}$, (b) the volume fractions of the dendritic structure in the mushy zone, $g^{s^{(1)}}$, and in the solid zone, $g^{s^{(2)}}$, the inter- and extradendritic eutectic structures, $g^{e^{(2)}}$ and $g^{e^{(3)}}$, as well as the sum of all solids, $g^{s}+g^{e}=g^{s^{(1)}}+g^{s^{(2)}}+g^{e^{(2)}}+g^{e^{(3)}}$, (c) the average compositions of the extra- and interdendritic liquids, $\langle w^{l^{(0)}}\rangle^{l^{(0)}}$ and $\langle w^{l^{(1)}}\rangle^{l^{(1)}}$, the dendritic structures, $\langle w^{s}\rangle^{s}=g^{s^{(1)}}\langle w^{s^{(1)}}\rangle^{s^{(1)}}+g^{s^{(2)}}\langle w^{s^{(2)}}\rangle^{s^{(2)}}$, and the eutectic structures, $\langle w^{e}\rangle^{e}=g^{e^{(2)}}\langle w^{e^{(2)}}\rangle^{e^{(2)}}+g^{e^{(3)}}\langle w^{e^{(3)}}\rangle^{e^{(3)}}$. The temperature history of the simulation is shown in Figure 2b, corresponding to a final normalized eutectic fraction g^{e}/g^{e}_{GS} equal to 0.91 (bold value in Table 6 for the Al-14wt%Cu alloy).

II.10 Table

(Step) / Interface	(S1)	(S2)	(S3)
$s^{(1)}l^{(1)}$	$S^{s^{(1)}l^{(1)}}_{(S1)} = \frac{2}{\lambda_2}$	$S^{s^{(1)}l^{(1)}}_{(S2)} = \left(1 - \frac{g^{e^{(2)}}}{g^{l^{(1)}}}\right) S^{s^{(1)}l^{(1)}}_{(S1)}$	-
$l^{(1)}l^{(0)}$	$S^{l^{(1)}l^{(0)}}_{(S1)} = 3\,\frac{R^{s^{(1)}l^{(0)}\,2}}{R^{l^{(0)}\,3}}$	$S^{l^{(1)}l^{(0)}}_{(S2)} = S^{l^{(1)}l^{(0)}}_{(S1)}$	-
$e^{(2)}l^{(1)}$	-	$S^{e^{(2)}l^{(1)}}_{(S2)} = \left(1 - \frac{g^{s^{(1)}}}{g^{l^{(1)}}}\right) 3\,\frac{R^{e^{(2)}l^{(1)}\,2}}{R^{l^{(0)}\,3}}$	-
$e^{(3)}l^{(0)}$	-	-	$S^{e^{(3)}l^{(0)}}_{(S3)} = 3\,\frac{R^{e^{(3)}l^{(0)}\,2}}{R^{l^{(0)}\,3}}$

Table 1: Interfacial area concentration between structures and liquids formed upon the solidification sequence defined in Figure 1. Symbol "-" stands for a non defined interface. It is equivalent to considering a nil value of the interfacial area concentration. All other interfaces defined by the various liquids and structures do not exchange mass. No mass exchange takes place during steps (S0) and (S4).

$l^{s^{(1)}l^{(1)}}$	$\left(\frac{g^{s^{(1)}}}{g^{s^{(1)}} + g^{l^{(1)}}}\right)\frac{\lambda_2}{6}$
$l^{l^{(0)}l^{(1)}}$	$\frac{R^{s^{(1)}l^{(0)}\,2}}{R^{l^{(0)}\,3} - R^{s^{(1)}l^{(0)}\,3}} \cdot$ $\left[\exp\left(-Pe^{l^{(0)}l^{(1)}}\left(\frac{R^{l^{(0)}}}{R^{s^{(1)}l^{(0)}}} - 1\right)\right)\left(\left(\frac{R^{s^{(1)}l^{(0)}}}{Pe^{l^{(0)}l^{(1)}}}\right)^2 + \frac{R^{l^{(0)}}R^{s^{(1)}l^{(0)}}}{Pe^{l^{(0)}l^{(1)}}} - R^{l^{(0)}\,2}\right) - \left(\left(\frac{R^{s^{(1)}l^{(0)}}}{Pe^{l^{(0)}l^{(1)}}}\right)^2 + \frac{R^{s^{(1)}l^{(0)}\,2}}{Pe^{l^{(0)}l^{(1)}}} - \frac{R^{l^{(0)}\,3}}{R^{s^{(1)}l^{(0)}\,2}}\right) + \frac{Pe^{l^{(0)}l^{(1)}}}{R^{s^{(1)}l^{(0)}}}R^{l^{(0)}\,3}\left(\frac{Iv\left(\frac{Pe^{l^{(0)}l^{(1)}}R^{l^{(0)}}}{R^{s^{(1)}l^{(0)}}}\right)\exp\left(-Pe^{l^{(0)}l^{(1)}}\left(\frac{R^{l^{(0)}}}{R^{s^{(1)}l^{(0)}}} - 1\right)\right)}{\frac{Pe^{l^{(0)}l^{(1)}}R^{l^{(0)}}}{R^{s^{(1)}l^{(0)}}}} - \frac{Iv(Pe^{l^{(0)}l^{(1)}})}{Pe^{l^{(0)}l^{(1)}}}\right)\right]$

Table 2: Mathematical expressions used for the diffusion lengths entering Equation (9) [13].

w_0 [wt%]	ΔT_N^s [K]	ΔT_N^e [K]	t_{end}-t_N^s [s]	t_{end}-t_N^e [s]	$\dot{T}(t<t_N^s)$ [K s^{-1}]	$\dot{T}(t>t_{end})$ [K s^{-1}]
4	35.	20.	41.5	0.37	-6.6	-8.1
14	15.	20.	63.7	10.43	-6.9	-6.5
24	25.	45.	88.2	21.53	-4.5	-6.4

Table 3: Summary of the measurements deduced from the recorded cooling curves for the three Al-Cu samples processed using electromagnetic levitation. Composition, w_0, nucleation undercooling of the dendritic and eutectic structures, ΔT_N^s and ΔT_N^e, solidification times measured from nucleation of the dendritic and eutectic structures, t_N^s and t_N^e, up to completion of the solidification, t_{end}, and cooling rates prior nucleation and after completion of solidification, $\dot{T}(t<t_N^s)$ and $\dot{T}(t>t_{end})$.

w_0 [wt%]	w_D [wt%]	DAS_D [µm]	g_D^e [%]	$g_{GS}^{e\ (1)}$ [%]
4	4.14	30.	5.6	7.81
14	12.74	25.	29.0	35.33
24	20.70	15.	57.2	67.64

Table 4: Summary of measurements deduced from composition measurements (SEM-EDS) and image analyses. (1) Calculated with w_0 and the phase diagram data given in Table 5).

Volumetric enthalpy of fusion, L [J m^{-3}]	[17]	10^9
Volumetric heat capacity, C_p [J m^{-3} K^{-1}]	[17]	$3.\cdot10^6$
Eutectic temperature, T_E [K]	[3]	821.
Eutectic composition, w_E [wt%]	[3]	33.2
Segregation coefficient, k [-]	[3]	0.17
Length of the eutectic tie line, C' [wt%]	[17]	46.5
Fraction of phase s in the eutectic structure, f [-]	[17]	0.54
Liquidus slope (s'/l), m'_L [K wt%$^{-1}$]	[17]	3.5
Gibbs-Thomson coefficient (s/l), Γ [Km]	[17]	$2.41\cdot10^{-7}$
Gibbs-Thomson coefficient (s'/l), Γ' [Km]	[17]	$0.55\cdot10^{-7}$
Contact angle (s/l), θ [°]	[16]	60
Contact angle (s'/l), θ'[°]	[16]	65
Diffusion of Cu in solid Al, D^s [m^2 s^{-1}]	[6]	$6.47\cdot10^{-5}$ exp(-134911./(R_gT))
Diffusion of Cu in liquid Al, D^l [m^2 s^{-1}]	[6]	$1.05\cdot10^{-7}$ exp(-23804./(R_gT))
Liquidus temperature, T_L [K]	Sample 4wt%Cu	923.
	14wt%Cu	895.
	24wt%Cu	861.
Initial temperature, T(t=0s) [K] (1)	Sample 4wt%Cu	939.
	14wt%Cu	939.
	24wt%Cu	869.
Domain radius, R [m]		$2.65\cdot10^{-3}$
External temperature, T_{ext} [K]		293.
Heat transfer coefficient, h($t<t^s_N$) [W m^{-2} K^{-1}]	Sample 4wt%Cu	27.
	14wt%Cu	29.
	24wt%Cu	18.
Heat transfer coefficient, h($t>t_{end}$) (2) [W m^{-2} K^{-1}]	Sample 4wt%Cu	45.

Table 5: Values for the properties for the Al-Cu alloys, sample size and initial and boundary conditions for the simulations. (1) Adjusted to fit the measured nucleation temperature, T^s_N, at time, t^s_N (Table 3 and Figure 2). (2) For the Al-4wt%Cu alloy, $h_{ext} = g^l\, h(t<t^s_N) + (1-g^l)\, h(t>t_{end})$ while $h_{ext} = h(t<t^s_N)$ for the two other alloys.

			c1	*c2*	*c3*	*c4*		
w_0 [wt%]	g^e_D/g^e_{GS} [-]	D^s [m^2 s^{-1}]	0.0, 0.0	35, 0.0	0.0, 20	35, 20	ΔT^s_N, ΔT^e_N [K, K]	
4	0.72	0	1.00	0.98	0.82	0.81	$g^l(T^e_N)/g^e_{GS}$	*l1*
		≠ 0	0.88	0.88	0.72	0.72		*l2*
		0	0.90	0.88	0.83	0.81	$\mathbf{g^e/g^e_{GS}}$	*l3*
		≠ 0	0.77	0.77	0.72	**0.72**		*l4*
w_0 [wt%]	g^e_D/g^e_{GS} [-]	D^s [m^2 s^{-1}]	0.0, 0.0	15, 0.0	0.0, 20	15, 20	ΔT^s_N, ΔT^e_N [K, K]	
14	0.82	0	1.00	1.00	0.84	0.84	$g^l(T^e_N)/g^e_{GS}$	*l5*
		≠ 0	0.97	0.97	0.81	0.81		*l6*
		0	0.97	0.97	0.95	0.95	$\mathbf{g^e/g^e_{GS}}$	*l7*
		≠ 0	0.93	0.93	0.91	**0.91**		*l8*
w_0 [wt%]	g^e_D/g^e_{GS} [-]	D^s [m^2 s^{-1}]	0.0, 0.0	25, 0.0	0.0, 45	25, 45	ΔT^s_N, ΔT^e_N [K, K]	
24	0.85	0	1.00	1.00	0.72	0.72	$g^l(T^e_N)/g^e_{GS}$	*l9*
		≠ 0	0.99	0.99	0.71	0.71		*l10*
		0	0.98	0.98	0.87	0.87	$\mathbf{g^e/g^e_{GS}}$	*l11*
		≠ 0	0.97	0.97	0.85	**0.85**		*l12*

Table 6: Predicted normalized volume fractions of eutectic, g^e/g^e_{GS}, and liquid, $g^l(T^e_N)/g^e_{GS}$, as a function of the nucleation undercooling of the dendritic and eutectic structures, ΔT^s_N and ΔT^e_N, and diffusion in the solid using the measured dendrite arm spacing given in Table 4. Normalization is carried out using the method proposed by Sarreal and Abbaschian [18], i.e. the value reached under Gulliver-Scheil approximations, g^e_{GS} (Table 4) The predicted liquid fraction is taken at the nucleation temperature of the eutectic structure, $T^e_N = T_E - \Delta T^e_N$.

Résumé en Français :

Chapitre III Experimental and numerical modeling of segregation in metallic alloys

Le modèle expérimental de solidification par lévitation électromagnétique présenté dans le chapitre II est considéré pour étudier l'effet de la germination déclenchée. Des échantillons d'alliages aluminium cuivre sont solidifiés en lévitation électromagnétique dont la germination de la phase primaire est déclenchée par une plaque d'alumine. Les compositions en cuivre étudiées sont de 4, 14 et 24wt%.

La température au cours de la solidification a été mesurée pour chaque échantillon. Ces mesures donnent accès aux surfusions de germination des phases primaires et eutectiques. La procédure expérimentale présentée dans le chapitre II a été appliquée. Les cartes de compositions chimiques révèlent une ségrégation à l'échelle des échantillons. Les cartes de fractions eutectiques révèlent une structure fine et plus particulièrement en bas des échantillons autour de la zone où la germination a été déclenchée.

Un modèle couplant automate cellulaire et élément fini est développé pour l'interprétation des résultats. Le modèle intègre un modèle de microségrégation à l'échelle de chaque cellule. Cette démarche permet de prendre en compte la surfusion de germination de la phase primaire ainsi que la diffusion de la phase solide dans le calcul du chemin de solidification à l'échelle des structures de grains. Un nouveau critère de remaillage a été intégré pour une adaptation du maillage éléments finis. Ce critère se base sur un estimateur d'erreur géométrique calculé a partir des dérivées secondes d'un champ scalaire à l'échelle du maillage élément fini.

L'application du modèle permet de prédire l'histoire thermique des échantillons ainsi que les cartes de composition chimiques. Le modèle permet d'expliquer les variations de fraction eutectiques mesurées à l'échelle des échantillons.

Chapter III Experimental and numerical modeling of segregation in metallic alloys

Abstract

Electromagnetic levitation is used as an experimental technique to study initiated nucleation and cooling rate effects on segregation, phase's volume fraction as well as on grain structure in metallic alloys. This technique is applied to spherical aluminum-copper alloy droplets with three different copper compositions Al-4, 14 and 24wt%Cu. For all samples, the primary phase nucleation has been triggered using an alumina plate at the bottom of the spherical domain with a given undercooling. Based on the recorded temperature curves, the heat extraction rate has been determined in addition to the nucleation undercooling for the eutectic structure. Additional characterizations consist of composition measurements using a scanning electron microscope (SEM) equipped with energy dispersive X-ray spectrometry and analysis of SEM images. The distribution maps drawn for the composition, the volume fraction of the eutectic structure and the dendrite arm spacing for the Al-4wt%Cu sample reveal strong correlations which is not the case for the Al-14 and 24wt%Cu samples. A 2D Cellular Automaton (CA) - Finite Element (FE) model is developed for the interpretation of the measurements. The model involves a new coupling scheme between the CA and the FE models together with a microsegregation model at the scale of the dendrite arms. Extensive validation of the model has been carried out demonstrating its capability to deal with mass exchange inside and outside the grains envelopes. The model has been applied to predict the temperature curves, the segregation and the eutectic volume fraction obtained upon a single grain nucleation and growth from the bottom of the spherical domain with and without triggering of the nucleation of the primary solid phase. Predicted temperature curves, final eutectic structure volume fraction as well as the eutectic map distribution are found to be in good agreement with the experimental data.

Keywords

Solidification, Segregation, EML, Grain Structure, Heterogeneous Nucleation, Cooling Rate, Modeling, CAFE, Mesh Adaptation.

III.1 Introduction

III.1.1 Experiments on segregation in binary alloys

In the last two decades, modeling and experiments of the solidification of binary metallic alloys have received jointly great interest [1, 2]. One of the main objective commonly fixed, is to achieve maximum control of the solidification process. Containerless techniques offer advanced control since heterogeneous nucleation, induced by the container wall in conventional processes, is completely avoided. Thus, large degree of undercooling can be achieved [3, 4, 5]. In addition, the cooling rate, the system geometry and shape (which is generally spherical), the limited temperature gradient, and the low variation of the heat extraction rate throughout the entire surface of the system within the solidification interval define a suitable experimental model for equiaxed solidification. In the recent past, impulsed atomization process has been proposed by Heringer el al. as an experimental model for the study of the segregation induced by equiaxed grain growth [6]. Prasad et al [7], has applied the same approach to achieve several impulse atomization experiments for different cooling rates on Al-Cu binary alloy system. A data set has been extracted from the atomized Al-Cu droplets consisting of X-ray tomography, segregation maps and average eutectic volume fraction over the atomized droplet. In addition, a correlation for the heat transfer coefficient during atomization process have been developed and integrated into on an isothermal segregation model [7]. However, measurement of the non-equilibrium temperature and undercooling prior to the nucleation of the primary and secondary phases was not available through the considered atomization process. Hence, the predicted temperature curves as well as the final eutectic volume fraction were not quantitatively validated.

Recently, ElectroMagnetic Levitation (EML) technique together with *in situ* temperature measurements have been used by Gandin et al [8] to study the solidification of undercooled Al-Cu droplet. Important information has been collected such as the cooling rate prior to the solidification and the nucleation undercooling of the dendritic and eutectic structures. In addition, an analytical model for the prediction of the temperature, the primary and the secondary (eutectic) recalescence as well as the final amount of the eutectic structure has been developed. Good agreement has been achieved between the measurements and the model prediction [8]. Results demonstrate that individual droplet processed by EML can be used as a model for equiaxed growth. However, only a one dimensional segregation profile can be extracted from the presented model. As a consequence, important experimental data such as solute and eutectic distribution map haven't been quantitatively utilized.

Similarly, Kasperovich et al [5] has applied different solidification techniques to study the segregation in Al-4wt%Cu binary alloy spherical system for a range of cooling rates from 0.01 to 20,000 K/s. The EML technique has been applied and high undercooling prior to the nucleation of the primary phase has been measured. Again, this work successfully demonstrates the reliability of atomization and electromagnetic technique as powerful experimental tools for the study and modeling of segregation in metallic alloy. However, modeling was only achieved in a 2D 500x433 µm zone using a 2D pseudo-front tracking model, [5], with a constant cooling rate approximated by

the slope of the linear part of the recorded temperature. Additionally, the recalescence and the growth of the eutectic structure were not accounted for to estimate on the final amount of eutectic structure.

III.1.2 Segregation models

Analytical and numerical models for diffusion based segregation have been developed and a review of them could be found in ref. [1]. Based on the work of Rappaz and Thévoz [9], Wang and Beckermann have developed an analytical multiphase multiscale model for both equiaxed and columnar solidification. They succeed to predict the effect of back diffusion in the solid at low cooling rate as well as the effect of dendrite tip undercooling at high cooling rate [10, 11]. This model have been used by Martorano et al. [12] to predict the columnar-equiaxed transition based on a solutal interaction mechanism between the equiaxed and the columnar grains. However, the solute diffusion length outside the grain envelopes was oversimplified based on a steady state solution. Gandin et al extended the work of Beckermann and co-authors by taking into account the nucleation and growth of eutectic structure [8]. Their model reveals the role of the eutectic structure nucleation and recalescence. Again, the estimation of the diffusion length in the liquid outside the mushy zone was approximated by an analytical formulation based upon steady state assumption.

Heringer et al developed an isothermal numerical model for equiaxed growth and the solute diffusion outside the grain envelope was numerically calculated [6]. However back diffusion in the solid was neglected and no description of the structure was available in the model. More sophisticated approaches, such as CAFE model, have been recently proposed to predict grain structure and segregation formed during solidification processes [13]. The main extensions of Guillemot el al. compared to Rappaz and Gandin CAFE model [14, 15], concern a new coupling scheme between the Finite Element, FE, and the Cellular Automaton, CA, models. The heat and solute mass transfers at the scale of the ingot, which are generally defined at the macro-scale, are modeled using the finite element method. Additionally, physical phenomena typical of phase transformations, such as solid-liquid phase growth and grain movement, are modeled at the grain scale defined by a CA grid superimposed onto the static FE mesh. While segregation taking place at the scale of the grain structure is predicted, its application remains limited by the use of a simple lever rule approximation.

III.1.3 Objectives of the present study

For the experimental viewpoint, as a continuation of previous work [8], EML is used as an experimental technique to study the heterogeneous nucleation effect on the solidification of three spherical sample of Al- 4, 14 and 24w%Cu solidified using EML technique. For each sample, metallurgical characterizations are performed to produce distribution maps of the average composition of copper, the volume fraction of the eutectic structure and the dendrite arm spacing. Regarding modeling, development of a 2D CAFE model is presented, integrating an advanced segregation model. Diffusion in the liquid in front of the growing mushy zone is calculated through a direct numerical solution of the diffusion field by solving the average solute mass conservation

equation with a refined FE mesh. An extensive comparison of the present model with differents modeling approaches is carried out. In addition, a parametric study is achieved demonstrating the model advantages compared to previous approaches. The model is then applied to the presented solidified Al-Cu sample where nucleation is triggered and to previous experiments with spontaneous nucleation [8]. *In situ* measurements of the temperature are compared to the predictions of the model. Additionally, predicted copper, and eutectic maps are compared to the measurement over a cutting plane for the solidified Al-Cu samples. The predicted average volume fraction of the eutectic structure is also compared to the measurements for Al-Cu samples with and without triggering of the nucleation of the primary solid phase.

III.2 Experimental

Spherical Al-Cu binary alloy systems were processed containerlessly by electromagnetic levitation technique (EML). A detailed description of the EML technique can be found in ref. [16]. Samples, with typically 0.2 g in mass, were prepared from pure Al (99.9999 %) and Cu (99.999 %). Additionally compositions were selected as 4, 14 and 24wt%Cu for later comparison with previous published work [8]. The magnetic field has been used to levitate the sample under a low gas pressure of about 40–50 mbar He and maintained during all the solidification process. The levitated sample was then cooled by reducing the power of the magnetic field. For a given undercooling solidification is triggered using an alumina plate. Once solidified, the metal consists of an approximately spherical volume with a diameter close to 5.3 mm.

III.3 Modeling

A coupled finite element model, FE, designed to solve the energy and the solute equation at the macro-scale, with a cellular automaton model, CA, for the modeling of the grain structure and physical phenomena at the scale of typical dendritic grain distance, as originally proposed by Gandin and Rappaz [14, 15], is extended and applied for the simulation of the solidified droplet. The two dimensional FE model, R2Sol, developed by Bellet et al. [17] and extended by Liu [18] solves the conservation equations averaged over a representative elementary volume containing a mushy zone, i.e., a mixture of the solid and liquid phases. The CA model published recently by Guillemot et al is implemented and a detailed description of the FE and the CA models can be found in ref [13]. In this section, only extensions are presented. Extensions concern: macrosegregation at the scale of the FE model based on a remeshing technique, microsegregation at the scale of the CA cells and the coupling scheme between the macro and the micro models.

III.3.1 Extensions of the Macroscopic FE model

III.3.1.1 Energy conservation.

The solid and the liquid phases are assumed to have constant and equal densities, ρ. Hence in pure heat diffusion regime, i.e. assuming a fixed solid phase and neglecting the convection arising from the liquid flow, the average energy conservation could be written as follows:

$$\rho\frac{\partial H}{\partial t} - \nabla\cdot(\kappa\,\nabla T) = 0 \qquad (1)$$

where H is the average enthalpy per unit mass. The average thermal conductivity, κ, is taken as a constant in the following. Further assuming constant and equal values of the specific heat for the liquid and the solid phases, C_p, one can write:

$$H = C_p \left[T - T_{ref.}\right] + g^f L \qquad (2)$$

where L represents the latent heat of fusion per unit of mass and T_{ref} is a reference temperature not being used explicitly in the integration of the equations [18]. g^f is the volume fraction of the total liquid phase; i.e. the inter, d, plus the extradendritic liquid, l.

III.3.1.2 Solute conservation.
The average conservation equation of a solute element in a binary alloy writes [17]:

$$\frac{\partial \langle w \rangle}{\partial t} - \nabla \cdot \left(D^l \, g^f \, \nabla \langle w^f \rangle^f \right) = 0 \qquad (3)$$

Where $\langle w \rangle$ is the average composition of solute, $\langle w^f \rangle^f$ is the average composition of the total liquid phase and D^l is the diffusion coefficient for the solute in the liquid phase assumed to be constant in the following. The primary unknown considered in the solute conservation, Equation 3, is the average composition of solute, $\langle w \rangle$. The average composition of the total liquid phase is eliminated following the work of Prakash and Voller [19] who introduced a split operator technique with an Euler backward scheme. The CA model is used to link the average composition of solute and the temperature to the fraction of solid following a modified version of the segregation model of Wang and Beckermann [10] as it is explained later in section *solidification path*.

III.3.1.3 Mesh adaptation.
The FE mesh adaptation approach initially proposed by Fortin [20] and developed by Alauzet and Frey [21] has been integrated in the FE model. It consists of a minimization method that evaluates the mesh size required to access a given error for a chosen field of the finite element solution. The main idea is that the mesh size can be controlled by a directional error estimator based on the recovery of the second derivatives of the finite element solution for a given scalar field [20, 21, 22]. This strategy is known as the Hessian strategy. The Hessian, which is the tensor of the second spatial derivatives, can be computed for any scalar component of the FE solution. As shown, this directional information is then converted into a mesh metric field which prescribes the desired element size and orientation and hence improves the FE solution precision. A detailed description of this remeshing technique can be found in ref [22]. For the present application, the average composition was selected to track the solute field ahead of grains as well as the segregation pattern in the grain. The Gruau and Coupez [23] unstructured and anisotropic mesh generation with adaptation has been used to generate the FE mesh when required.

III.3.2 Extensions on the Microscopic CA model

III.3.2.1 Solidification path.

As proposed by Gandin and Rappaz [14, 15], Figure 1.(a) gives a schematic view of the coupled CAFE model. The continuous domain is discretized into a FE triangular mesh to solve the conservation equation at the macroscopic scale. Similarly, a square lattice of the CA is superimposed to the FE mesh. Each cell ν is uniquely defined by the coordinates of its center, $C_\nu = (x_\nu, y_\nu)$, located in a finite element mesh, F. Linear interpolation coefficients, $c_\nu^{n_i^F}$, are defined between each node, n_i^F, and a cell ν defining bidirectional exchanging ways of information from the FE nodes to the CA cells. A variable available at the nodes, such as the temperature, T_n, or the average composition, $<w_n>$, can thus be used to calculate an interpolated value at cell ν, respectively T_ν or $<w_\nu>$. Similarly, information computed at the level of the CA grid can be projected at the level of the FE nodes. The approach developed by Guillemot et al [13, 24] is implemented for the nucleation of the predicted grain structures. Thus, for a fully liquid cell, an equilateral quadrilateral surface is defined when the prescribed undercooling is reached, and the cell is then considered as mushy; i.e. formed by a mixture of the solid, s, and the interdendritic liquid, d, phases. The growth rate of each half diagonal, $\partial R_i^e/\partial t$, of the rhombus surface is calculated as a function of the local supersaturation ahead using the Ivantsov relation [25] together with the marginal stability criteria [26] until it reaches a final value, R^f. Thus, as illustrated in Figure 1.(b), the initially equilateral quadrilateral form can be deformed in one or more directions depending on the solute profile ahead each tips. The mushy zone volume fraction, g_ν^m, assigned to each cell, *v*, is defined as the sum of the volume fraction of the interdendritic liquid, g_ν^d, and the solid, g_ν^s, phases, i.e. $g_\nu^m = g_\nu^s + g_\nu^d$. The time derivative of the mushy zone volume fraction, $\partial g_\nu^m/\partial t$, is calculated as the mean of the ratio of the geometric surface tips growth rate, $\partial R_i^e/\partial t$, to the final position, R^f, as follows:

$$\frac{\partial g_\nu^m}{\partial t} = \frac{\partial (g_\nu^s + g_\nu^d)}{\partial t} = \frac{1}{4\,R^f} \sum_{i=1}^{4} \frac{\partial R_i^e}{\partial t} \qquad (4)$$

The final radius, R^f, is defined as the spatial limit for the growth of each tip of the rhombus, which is of the order of several secondary arms spacing. In the case of a dendritic structure, this limit can be easily defined as the half of the primary dendrite arms spacing; i.e. $R^f = \lambda_1/2$. This distance depends on the solidification local thermal gradient and can fluctuate during the solidification process. For the present study it will be assumed as a constant and the same strategy is chosen for the equiaxed and columnar grains.

Figure 1.(c) is a simplified schematic view of the considered assumptions for the solute exchanges between the different phases defined for a given mushy cell. Accordingly, the solid phase, s, is assumed to only exchange solute with the interdendritic liquid phase, d. While, phase d exchanges solute with the extradendritic liquid, l, and the solid, s, phases. In addition, equilibrium is assumed at the s/d interface, i.e. $w^{sd} = kw^d$ where w^{sd} is the composition of the solid phase at the s/d interface

and k is the partition ratio. Moreover, a diffusion solute profile is assumed in the solid and the extradendritic liquid phase characterized respectively by the diffusion lengths l^{sd} and l^{ld}. As proposed by Wang and Beckermann [10], correlations of the diffusion lengths are given in table 1.

The temperature, T_ν^s, the solid volume fraction, g_ν^s, the average composition of solid phase $<w_\nu^s>^s$ and the average composition of the liquid phase $<w_\nu^l>^l$ are calculated with respect to the interpolated enthalpy, H_ν, and average composition, $<w_\nu>$ using an extended microsegregation model based on the previous work of Wang and Beckermann [10]. The model could be written at the scale of a CA cell as follows:

Solute balance in the solid phase, s.

$$\frac{\partial g_\nu^s <w_\nu^s>^s}{\partial t} = \bar{w}^{sd} S^{sd} \bar{V}_n^{sd} + S^{sd} \frac{D^s}{l^{sd}} \left(\bar{w}^{sd} - <w_\nu^s>^s \right) \tag{5}$$

Thus, the solid phase exchange solute due to the solid-liquid interface motion, first right hand side (RHS) term and back diffusion in the solid phase, second RHS term. Similarly, the solute balance equations can be written for the intra- and the extra dendritic liquid phases as follows:

Solute balance in the intra-dendritic liquid phase, d.

$$\frac{\partial g_\nu^d <w_\nu^d>^d}{\partial t} = -\bar{w}^{sd} S^{sd} \bar{V}_n^{sd} - \bar{w}^{ld} S^{ld} \bar{V}_n^{ld} - S^{sd} \frac{D^s}{l^{sd}} \left(\bar{w}^{sd} - <w_\nu^s>^s \right) - S^{ld} \frac{D^l}{l^{ld}} \left(\bar{w}^{ld} - <w_\nu^l>^l \right) + g_\nu^d \dot{\varphi}^d \tag{6}$$

Solute balance in the extra-dendritic liquid phase l.

$$\frac{\partial g_\nu^l <w_\nu^l>^l}{\partial t} = \bar{w}^{ld} S^{ld} \bar{V}_n^{ld} + S^{ld} \frac{D^l}{l^{ld}} \left(\bar{w}^{ld} - <w_\nu^l>^l \right) + g_\nu^l \dot{\varphi}^l \tag{7}$$

Phase's volume fraction balance.

$$g_\nu^s + g_\nu^d + g_\nu^l = 1 \tag{8}$$

In addition, for each phase i, the time derivative of the phase volume fraction, $\partial g_\nu^i / \partial t$, can be written as a function of the interfacial area concentration, S^{ij} (given in Table 1), and the normal velocity of the ij interface, $\bar{V}_n^{ij}$, {(i,j) = (s,d), (l,d)} as follows:

$$S^{ij} \bar{V}_n^{ij} = \frac{\partial g_\nu^i}{\partial t} = - \frac{\partial g_\nu^j}{\partial t} \tag{9}$$

Compared to the Wang and Beckermann model [10, 11], the presented model, equations 5 to 9, integrates additional terms, $\dot{\varphi}^j$ with {j = d, l} to take into account the variation of the cell average composition by diffusion with the surrounding liquid phases. As defined for the solute diffusion at the macro-scale, Equation 3, the cell may only exchange solute either through the inter- or the extra-dendritic liquid phase. By summing up $g_\nu^d \dot{\varphi}^d$ and $g_\nu^l \dot{\varphi}^l$, we obtain the equivalent terms at the scale of the CA model of the solute diffusion term, $\nabla \cdot (D^l g^f \nabla <w^f>^f)$, calculated at the finite element model. The relative portions, $\dot{\varphi}^l$ and $\dot{\varphi}^d$, could be quantified by introducing a diffusion partition

ratio, ε_v, which is defined as $\varepsilon_v = \dot{\varphi}^l/\dot{\varphi}^d$. A correlation of ε_v is proposed as a function of the volume fraction of the inter- and extradendritic liquid phase as follows:

$$\varepsilon_v = \frac{g_v^l}{g_v^l + g_v^d} \tag{10}$$

The model is coupled to the heat and solute balances respectively written as follows:
Heat balance.

$$\frac{\partial <H_v>}{\partial t} = C_p \frac{\partial T_v}{\partial t} - L \frac{\partial g_v^s}{\partial t} \tag{11}$$

Solute balance.

$$\frac{\partial <w_v>}{\partial t} = \frac{\partial g_v^s <w_v^s>^s}{\partial t} + \frac{\partial g_v^d <w_v^d>^d}{\partial t} + \frac{\partial g_v^l <w_v^l>^l}{\partial t} \tag{12}$$

III.2.2.2 Coupling Scheme.

The following steps give the main lines of the implemented coupling scheme:

s(0)-Initialization; Based on the simulation parameters, fields over the FE mesh and CA grid are initialized and the linear interpolation coefficients, c_v^{nF}, are computed.

s(1)-Mesh adaptation; If required, remeshing of the FE mesh and recalculating the topological link between the FE mesh and the CA grid. Based on the position of its center, C_v, each cell, v, is assigned to the new FE, F, containing C_v. Subsequently, new linear interpolation coefficients c_v^{nF} are evaluated. Finally, all fields computed at the level of the CA are then projected from the CA grid to the FE nodes. This procedure is equivalent to a transport from the old mesh to the new one, but with the advantages to give more accuracy and to keep consistency between fields at the two different micro, CA, and macro, FE, scales.

s(2)-FE Resolution; FE solution of the energy and solute conservation equations.

s(3)-Interpolation; The calculated average enthalpy and composition fields are interpolated into the CA gird.

s(4)-CA calculation; Nucleation, growth, of the predicted dendritic structure and segregation at the scale of the CA grid are calculated.

s(5)- All Fields computed at the scale of the CA model are projected to construct their equivalent values at the scale of FE model.

s(6)-Next time step; Go to step 1 if solidification is not completed.

III.3.3 Resolution

Equation 1 and 3 are solved on the FE mesh. The average enthalpy H is taken as the primary unknown in the energy conservation, and the temperature in this equation is eliminated by a first

order of Taylor's expansion as a function of the average enthalpy. The derivatives $\partial H_v/\partial T$ are calculated in the CA model and projected onto the FE nodes during the step 5 of the coupling scheme. An extended description of the strategy used to solve the listed conservation equations as well as several validations of the implementations are given by Liu [18].

Microsegregation at the scale of each CA cell is calculated as follows: Eq 5, 6, 7 and 10 constitute a complete system of differential equations for four unknowns: T, $<w_v^l>^l$, g_v^s, $<w_v^s>^s$. The growth of the mushy zone is computed using Equation 4, where the half diagonal length variations are calculated according to the supersaturation ahead each of then as described by Guillemot et al [24]. The volume fraction of the interdendritic liquid phase and the external liquid phase are respectively defined and computed as $g_v^d = g_v^m - g_v^s$ and $g_v^l = 1 - g_v^m$. $<w_v^d>^d$ is calculated using the phase diagram, assuming a total mixture of the interdendritic liquid phase: $<w_v^d>^d = (T-T_m)/m_L$, where T_m is the melting temperature of the pure material and m_L is the liquidus slope. A splitting scheme is applied to the differential equations, Eq 5, 6, 7 and 10, together with a first order Taylor series. Diffusion lengths, geometrical relations and thermodynamic conditions are listed in tables 1 and 4. An iterative algorithm is implemented to calculate the system solution.

III.3.4 Validation

This section presents calculations that have been carried out for spherical Al-4 and 10wt%Cu alloy equiaxed dendritic grains in order to compare the present model to previous model for equiaxed solidification in metallic alloy.

III.3.4.1 Assumptions

The following approximations are considered:

va1- *Geometry.* Simulations are carried out in axisymmetric coordinates on a quarter of a spherical domain of radius R, with an external surface, A, and a volume, V.

va2- *Heat transfer*. The heat extraction from the system follows a global heat balance defined by a heat extraction rate at the limit of the domain with the external environment, $\dot{q}_{ext}$. A Fourier boundary condition is assumed, defined by constant values of the heat transfer coefficient, h_{ext}, and temperature, T_{ext}, such that $\dot{q}_{ext} = h_{ext}\,(T - T_{ext})$. A simplified global heat balance can thus be derived:

$$m\frac{dH}{dt} = -\int_A h_{ext}(T - T_{ext})dS \qquad (13)$$

where m is the mass of the system, H is the average enthalpy of the system and T is the temperature at the system boundary.

va3- *Alloy.* A linear monovariant line of the phase diagram is assumed, that separates the fully liquid region from its mixture with the primary solid s. The value of its slope, m_L, is computed

for each alloy considering the value of the eutectic temperature, T_E, the eutectic composition, w_E, the liquidus temperature of the alloy read on the phase diagram, T_L, and the nominal composition of the alloy, w_0, using $m_L=(T_E-T_L)/(w_E-w_0)$. A constant segregation coefficient, k, is also used, that links the equilibrium liquid and solid compositions within the mixture.

va4- Nucleation and growth. The nucleation temperature of the dendritic structure α is defined with respect to the liquidus temperature of the alloy, T_L, by a prescribed nucleation undercooling, ΔT_N^α, i.e. $T_N^\alpha = T_L - \Delta T_N^\alpha$. Nucleation is supposed to take place at the center of the domain. The grain is assumed to be spherical in shape and its growth rate is calculated as a function of the mushy zone front supersaturation:

$$\Omega = (w^d - w^\zeta)/((1-k)\cdot w^d) \qquad (14)$$

w^d is the average composition of the interdendritic liquid phase. In the following, w^ζ, is taken equal to the average composition of the external liquid phase, $<w_v^l>^l$, the nominal composition of the alloy, w_0, or the average composition of the cell, $<w_v>$.

va5-Eutectic. The eutectic structure is supposed to nucleate at the eutectic temperature given by the phase diagram. Isothermal eutectic transformation is assumed.

III.3.4.2 Prediction

Figure 2.(a, b , c and d) is a snapshot of the model prediction when the grain average volume fraction is about 0.64 [-]. Simulation is carried out for the solidification of a 250 μm diameter Al–10 wt%Cu droplet, typical of the impulse atomization process, with 30 K for the primary phase nucleation undercooling. The aim is to compare the present model to Heringer el al. [6] model calculations in terms of the magnitude of the segregation pattern. For the calculation of the mushy zone growth rate, w^ζ is taken equal to the initial alloy composition, w_0, in Eq. 14 as selected by Heringer et al. [6]. Details of the numerical simulation parameters are listed in table 4. The second spatial derivatives of the average composition field are used to guide the mesh size as explained earlier. The mesh adaptation is clearly distinguished from figure 2.(a). Indeed triangular elements sizes are generated as a function of the solute profile. Hence the finest elements are in the mushy zone front where the latent heat release is maximum due to the mushy zone growth, figure 2.(b), and the solute diffusion layer is settled, figure 2.(c). In addition, this zone is marked by a sharp jump from one to zero of the volume fraction of the mushy zone, figure 2.(d). The elements size increase in the zone where the solute gradient is lower and relatively coarser spatial discretization gives accurate results with regard to the fixed tolerance. As shown in Figure 2.(e), the present model successfully predicts the segregation profile predicted by Heringer et al model. Extended validation of the present model with the Heringer et al. model [27] as well as a front tracking model are presented elsewhere [28].

The model predictions for the growth of equiaxed dendritic grains of Al-4wt%Cu alloy, with three different final grain sizes, R^f = 0.1, 1 and 10 mm together with the Wang and Beckermann

model calculations [12] are presented in figure 3. Simulations are performed for zero nucleation undercooling and the solutal interactions for purely equiaxed growth are quantitatively examined. These simulations intend first to study the effect of the new method for the mushy zone calculation and to show the capabilities of the model to deal with mass exchange outside the grain envelope. Figure 3 shows the temporal evolution of the mushy zone volume fraction, g^m, and the internal solid volume fraction, g^{sm}, in the three cases.

Figure 3.c1 presents the model predictions when the external liquid average composition, $<w^l>^l$, is used to calculate the velocity of the corresponding dendrite tips where as Figure 3.c2 presents the prediction when the cell average composition is used instead as proposed by Guillemot et al[24]. From figure 3.(11) to 3.(13), one can observe that the differences between the two models decreases as the final radius of the dendritic grain increases. First, it should be noted that the average composition of the extradendritic liquid phase, $<w^l>^l$, is used in the Wang and Beckermann model to calculate the growth rate of the mushy zone. With a final radius equal to 10 mm and since the solute diffusion length, l^{ld}, is of the order of magnitude of 1.10^{-5}m, the average composition of the extradendritic liquid phase shows a little variation until the mushy zone reaches the grain boundary, figure 5, and then reach the composition of the interdendritic liquid phase. Hence, when using the cell average composition, $w^\zeta = <w_v>$, instead of the average composition of the total extradendritic liquid phase, $w^\zeta = <w^l>^l$, the model predictions show better agreement with the analytical model solution. However, when decreasing the final radius of the dendritic grain, solute interaction between the intra- and the extra- dendritic liquid phase becomes more significant, figure 5, and the model deviates from the analytical solution, Figure 3.(11) and 3.(l2). This mainly is due to the fact that the average composition of the cell at the mushy zone front deviates from the average composition of the extradendritic liquid phase. The present model recovers the Wang and Beckermann model predictions when using the average composition of the extradendritic liquid phase. This composition is calculated by integration over the fully liquid zone at the scale of the FE model of the average composition at each node.

Additional calculations have been made to estimate the effect of the primary dendrite arm spacing on the model predictions compared to the analytical model, and are presented in Figure 4. Again, when using the average composition of the extradendritic liquid phase, $<w^l>^l$, a better agreement is found with the analytical solution. However, when increasing the ratio between the primary and the secondary arm spacing, here taken arbitrarily equal to 4, better agreement is achieved when considering the cell average composition to calculate the growth rate. This is mainly due to the shift of the average composition of the external liquid phase, $<w^l>^l$, calculated with the present model, Figure 5 green curves, reducing the gap with the Wang and Beckermann model predictions, Figure 5 black curves. In addition, it should be noted that the analytical solution remains an approximation, since solute diffusion in the external liquid phase is calculated based on approximation of the diffusion boundary layer under steady state [10 and 12]. The present model predicts that the mushy zone will completely be developed until it reaches the system boundary, i.e.

g^m = 1, which is more realistic than the analytical solution where a fully eutectic ring zone is predicted.

III.4 Result

III.4.1 Experimental

All experimental measurements have been carried out following the experimental approach published recently [8]. The grey curves, in Figure 6, are the recorded temperature histories evolutions for the three Al-Cu samples solidified under electromagnetic levitation. The temperature signal is affected by noise which could be induced by the translations and rotations of the levitated samples as well as the pyrometer sensitivity. However, sudden clear changes of the cooling rates are measured at the same time when the alumina plate is put together with the sample. This is identified as the nucleation time of the primary structure, reported in figure 6 as t_N^α. For the Al-4wt%Cu sample, a change in the slope is also identified near the liquidus temperature, T_L, followed by an area of little variation, then the temperature curves retrieves approximately the same slope after the primary phase nucleation to remain almost the same for the remaining solidification time, figure 6.a. The same trend is observed for the Al- 14 and 24wt%Cu samples. Hence, two jointly effects coexist after the contact with the trigger since the nucleation has been initiated using an alumina plate. First, the cooling rate increases is due to an additional important heat extraction throughout the trigger/droplet contact surface. Thus, the measured temperature curve for the Al-4wt%Cu becomes mainly guided by the heat extraction through the alumina plate after the small plateau near the liquidus temperature. As a consequence, a fast growth of the structures is expected since all the released latent heat is evacuated. On the other hand, the sudden partial release of the enthalpy of fusion due to the nucleation of the primary phase affects the cooling rates of the system which become approximately equal to zero for the Al-4wt%Cu to positive values for the two other samples. Furthermore, small plateau near the eutectic temperature, T_E, is the marker of an additional heat release which is typical of the eutectic structure growth [26]. The nucleation and growth of the eutectic structure compensate the extracted energy from the system, (Figure 6.b and 6.c). This is clearly identified through the temperature profile that exhibits a plateau which increases in length as the initial copper composition, w_0, increases. The duration of this plateau is thus proportional to the amount of the eutectic structure measured in as solidified state, g_D^e. The times for the beginning of these changes are labeled t_N^α and t_N^E in Figure 6. Therefore, the temperatures measured at times t_N^α and t_N^E, respectively T_N^α and T_N^E, also correspond to the nucleation temperature of the dendritic and eutectic structures. Nucleation happens with an important undercooling for both the primary and the eutectic structures in the case of the Al-24wt%Cu, respectively $\Delta T_N^\alpha = T_L - T_N^\alpha$ and $\Delta T_N^E = T_E - T_N^E$ with respect to the liquidus temperature of the alloy, T_L, and the eutectic temperature, T_E, as extracted from figure 6 and listed in Table 2. Conversely, for the Al-4wt%Cu as well as for the Al-14wt%Cu, the primary and the eutectic structure nucleation undercoolings are not significant with regard to the pyrometer measurement uncertainty, and hence cannot be extracted from the measured curves. The labels t_{end} in Figure 6 define the end of the solidification by the last characteristic time at which a significant slope change is observed in the cooling curve. For the Al-4wt%Cu, the end of the

solidification is defined as the time where the recorded temperature is below the equilibrium eutectic temperature, T_E. Other measurements on each curve are the cooling rates just before and after the end of the solidification, respectively $\dot{T}(t<t_N^{\alpha})$ and $\dot{T}(t>t_{end})$ listed in Table 2. As proposed by Gandin *el al.*, cooling rates just before the primary phase nucleation, $\dot{T}(t<t_N^{\alpha})$, have been used for the adjustment of the heat extraction rate due to energy transfer with the external environment for the total free surface of the sample, i.e. $h_{ext}^{A1}(t<t_N^{\alpha}) = h_{ext}^{A2}(t<t_N^{\alpha})$. In addition, the same approach has been applied to calculate the heat transfer coefficient between the alumina plate and the fully solid droplet by neglecting heat extraction through the free droplet surface with respect to the heat extracted through the alumina plate. Detailed description of the procedure can be found in ref 8 and the used initial temperatures for the calculations are listed in table 4. The fitted, $h_{ext}^{A1}(t<t_N^{\alpha})$ and $h_{ext}^{A2}(t<t_N^{\alpha})$, values for the calculations are also listed.

Additional experimental measurements consist of the copper composition conducted on the meridian cross section of the Al-Cu droplets as distribution maps have been achieved. In addition, the 2D SEM image analysis used previously [29, 8] has been applied to calculate the eutectic volume fraction and the DAS for the same cross sections. Global averaging over the entire measurements for each sample leads to the values listed also in Table 3 as w_D, DAS_D, and g_D^e respectively for the average copper composition, eutectic volume fraction and the dendrite arm spacing. The average copper content, w_D, shows a deviation from the nominal composition, $(w_D-w_0)/w_0$, that varies from -8.37% for the 24 wt% Cu to +9.25% for the 4 wt% Cu. As explained by Gandin et al [8], these deviations are expected to result from a non-symmetric growth of the dendritic structure as well as of the segregation patterns within a symmetry plane or with a symmetry axis defined with respect to the analyzed central meridian cross sections. The average eutectic volume fraction over the entire section plane, g_D^e, is closer to the Gulliver-Scheil model prediction g_{GS}^e for a closed system with the initial composition, w_0 listed in Table 3. These results deviate from previous measurements for Al-Cu samples processed upon EML where the nucleation events happen spontaneously. This could be explained by the short solidification times for the triggered samples. Hence solute back diffusion doesn't affect the obtained final amount of eutectic structure. In addition, no important recalescence has been measured with the eutectic structure growth. Thus both back diffusion in the solid and the eutectic undercooling and growth have a minor effect on the Al-Cu sample with initiated nucleation presented here.

Column 1 in Figure 7 presents the results of the normalized measurements of the distribution maps of an average Cu content for $120\cdot10^{-6}$ m × $150\cdot10^{-6}$ m local surface. Normalization is achieved with respect to the initial composition as, $(w-w_0)/w_0$. A macro-segregation at the scale of the analyzed surface is identified by regions with negative and positive deviations with respect to the nominal.

The normalized distribution maps of the volume fraction of the eutectic structure deduced from image analyses are shown in Column 2 in Figure 7. The normalization has been achieved following the work of Sarreal and Abbaschian [30], i.e. using the value of the volume fraction of the

eutectic structure predicted by the Gulliver-Scheil for each alloy, g^{e}_{GS}, listed in Table 3. Positive deviation from the Gulliver-Scheil model prediction is predicted around the nucleation point, Figure 7.(2). This is clearer when considering the Al24%wt%Cu where also a finest structure are measured, figure (7.(3)).(c). According to what has been previously reported [8], a positive deviation from the nominal value should be also measured in the same zone. However, no direct correlation between the normalized copper and the eutectic structure volume fraction maps is evident. This could be explained by the short solidification time of the analyzed sample compared to what has been done elsewhere together with a finest structure due o the important thermal gradient [26], after the contact with the alumina plate.

The DAS is shown in Column 3 in Figure 7 with a global average value given also in Table 3. This characteristic length is found to decrease as the nominal composition increases, which has been also observed from previous similar experiments [8]. Strong correlation together with the copper and eutectic map is found for the Al4wt%Cu sample.

III.4.2 Prediction

Simulations are carried out in axisymmetric coordinates on a half of a spherical domain of radius R, with an external surface, A, and a volume, V. The external surface is divided in two parts: A1 in contact with the alumina plate and A2 the free surface of the droplet. Notations and assumptions *va3* and *va5* given in the validation section together with the following approximations are considered:

pa1- Heat transfer. The heat extraction from the system follows a global heat balance defined by a heat extraction rate at the limit of the domain with the external environment, $\dot{q}_{ext}$. A Fourier boundary condition is assumed, defined by two values of the heat transfer coefficients related to A1 and A2 external surfaces, $h^{A1}_{ext}(t)$ and $h^{A2}_{ext}(t)$, and temperature, T_{ext}, such that $\dot{q}_{ext} = h^{A1}_{ext}(t)(T|_{A1} - T_{ext}) + h^{A2}_{ext}(t)(T|_{A2} - T_{ext})$. A simplified global heat balance can thus be derived:

$$m\frac{dH}{dt} = -\int_{A1} h^{A1}_{ext}(t)(T - T_{ext})dS \; - \int_{A2} h^{A2}_{ext}(t)(T - T_{ext})dS \qquad (15)$$

where m is the mass of the droplet, H is the average specific enthalpy of the system and T is the temperature at the system boundary. $h^{A1}_{ext}(t)$ is taken equal to $h^{A2}_{ext}(t)$ before the nucleation of the primary phase.

pa2- Nucleation. A single nucleation event at the bottom of the domain is considered with the measured undercooling calculated with respect to the liquidus temperature listed in Table 4.

Table 4 summarizes all the used input numerical data for the model. In addition, Table 1 gives the correlation used for the solute diffusion length in the extradendritic liquid phase, l^{ld}, for back diffusion in the solid, l^{sd}, as well as the interfacial concentration area, S^{ld} and S^{sd}. The same

approach has been used for the adjustment of the heat transfer coefficients to simulate heat extraction through the trigger for the three Al-Cu samples. $h_{ext}^{A1}(t)$ is taken equal to $h_{ext}^{A2}(t)$ for the cooling of the fully liquid sample. When the primary solid phase measured nucleation undercooling is reached, ΔT_N^{α}, the value of the heat transfer coefficient $h_{ext}^{A1}(t)$ increases linearly to reach the final value given in Table 4, during the required time to decrease the temperature of the south pole by 1K. The same alumina plate has been used to initiate the nucleation for all samples, a single value has been used for the heat extraction coefficient $h_{ext}^{A1}(t)$.

Figure 6 presents the model prediction of the averaged temperature over the simulation domain, black curves, as well as at the north, -▲-, and at the south, -▼-, poles of the domain for the three Al-Cu samples. Sharp changes on the predicted temperature slope at the nucleation point clearly mark the effect of the implemented adjustments of the heat transfer coefficients. The model predicts a huge decrease of the temperature after the nucleation of the primary solid phase at the bottom of the system, Figure 6.(a), (b) and (c). Thus the lower zone of the system is expected to present the lower amount of eutectic in the three cases. Indeed, no clear signal of eutectic transformation is predicted in this zone. In addition, segregation based diffusion is expected to have a minor effect leading to an average composition slightly different from the nominal composition at the bottom. This is also confirmed by the final eutectic, g_D^E, and the average composition, w_D, maps. By contrast with the top of the system, an increase of the temperature is predicted; which is expected to be due to the diffused released latent heat in the front of the growing of the mushy zone in the fully undercooled liquid. For the Al-14wt%Cu, the predicted average temperature curve presents an inflection point subsequent to the nucleation of the primary solid phase. Thus more important released heat is expected. This is also predicted for the Al-24wt%Cu droplet, where the average temperature of the system show a little variation near the nucleation temperature of the primary solid phase, Figure 6.(c). Additionally, due to the high undercooling, ΔT_N^{α} = 32K, an the released heat is leads to the predicted temperature curves quite similar to the one measured at the top of the system, Figure 6.(c).

Additionally, the eutectic plateau is predicted by the model. Its effect on the average temperature of the system is very small on the Al-4wt%Cu. However, again the implemented isothermal eutectic transformation is more clear when analyzing the predicted temperature at the top of system, Figure 6.(a), where an inflection point is predicted. This effect is more significant for the Al- 14 and 24wt%Cu leading to a plateau proportional to the predicted final eutectic amount. The predicted average eutectic volume fractions, g_P^E, are listed in Table 3 together with the measured values g_D^E. These values are close to the Gulliver-Scheil model predictions g_{GS}^E. Again, this can be explained by the short solidification time and the high heat extraction rate through the trigger. However, it should be noted that for the Al-24wt%Cu system, the eutectic transformation is considered with the measured undercooling prior to the nucleation leading to the value g_P^E = 65% close to measured one g_D^E = 61.62 %. Model prediction increase up to g_P^E = 81.4 when the simulation is run with an isothermal eutectic transformation at the eutectic temperature, T_E, given by the phase.

The present model has also been applied to the EML solidification experiences with spontaneous nucleation [8]. Only the results in terms of the final amount of eutectic are reported in Table 3. The model predictions reported in Table 3, g_P^E =6.8% for the Al-4wt%Cu and g_P^E =67% for the Al-24wt%Cu and, deviate from the measured value, g_D^E. These predictions retrieve the results of the simulations presented in reference [8] when an isothermal transformation is assumed to occur at the nucleation undercooling measured for the eutectic structure. The origin of these deviations from the measurements is in fact identified to the eutectic recalescence that is measured for these samples and that can consequently not be neglected [8]. The approximation of an isothermal eutectic transformation is thus identified as a remaining limitation of the present CAFE model. These remarks are of prime importance for quantitative prediction of phase fractions in solidification processes of alloys.

Figure 8 summarizes the model predictions for the normalized average copper composition, w, and the eutectic volume fraction, g^E. The same scales used for the representation of the measured data map are chosen. The magnitude of the segregation is less than the measured for each alloy. However, it should be noted that the normalization have been achieved using the nominal composition of the sample 4, 14 and 24wt% where the measured copper average content over the cross section are respectively 4.14, 13.81 and 21.99 wt%. For the triggered Al-4%wt%Cu sample, Figure 7.(a) shows a correlation between the distribution map of copper and the eutectic fraction. This is in line with the distribution maps presented for the spontaneously nucleated samples [8]. Similar trends are observed in the simulated maps presented in Figure 8.(a). Because the eutectic transformation is modeled with no eutectic undercooling, the remaining liquid at T_E that will transform into eutectic only depends on the average local composition and the effect of diffusion in the solid. But the latter effect is small for the triggered samples. Consequently, more eutectic is found in region of lower average copper content, typical of the result know from classical microsegregation analyses. The case of Al-24%wt%Cu is more interesting. Figure 8.(c) shows a clearly a deviation from a correlation between the average Cu content and the eutectic fraction at the bottom of the sample, where more eutectic is found for less Cu. This is also predicted and could thus be analyzed into detail. The reason explaining this result is the diffusion of Cu outside the mushy zone that decreases the amount of solute there together with the quenching of the remaining interdendritic liquid into eutectic at the nucleation temperature measured. At the top of the system, more time is available for the dendritic structure to solidify because the cooling rate is smaller as discussed above. Thus less liquid is available for the eutectic transformation.

III.5 Conclusion

The experimental and numerical achievements within the present contribution could be summarized as follows:

- Al-Cu alloys systems have been solidified using EML technique with compositions 4, 14 and 24wt%Cu. Sample are approximately spherical in shape with a radius of 2.65 10^{-3}m. The nucleation of the primary phase has been initiated using an alumina plate at

the lower surface for each sample. Non-equilibrium temperature histories have been recorded using an optical pyrometer. Important heat loss is measured with the contact of the trigger with the south pole for each droplet. Rectangular spatial discretization over a central cross section has been applied. The local copper content together with the eutectic volume fraction and the dendrite arm spacing have been measured. The averaged copper content over the analyzed cross section shows a minor deviation from the nominal composition. In addition, the normalized copper maps reveal a macrosegregation at the scale of the droplet. Normalizations have been also achieved for the local eutectic structure volume fraction with respect to the eutectic amount predicted by the Gulliver-Scheil model (Table 3).The effect of cooling rate on the final eutectic maps are measured. As previously established, these data could be used to validate and guide the development of an advanced solidification numerical model.

- Advanced microsegregation model have been embedded in a 2D CAFE model together with a mesh adaptation technique. The new model could be seen as an extension of previous CAFE modeling in two main directions. First, it accounts for back diffusion in the solid phase as well as for the nucleation undercooling of the solid phase at the scale of the grain structure. In addition, at the macro-scale, the solute diffusion in front of the mushy/liquid interface is solved over an adaptive mesh depending on the local solute and heat profile. Extensive validations of the model have been conducted showing its capability to deal with solute diffusion inside and outside a growing mushy zone.

- Applications to the simulation of the solidification of the processed Al-Cu droplet have been achieved. The predicted temperature curves give a coherent explanation of the measured temperature evolutions during the solidification of the Al-Cu samples. Although the predicted magnitudes of the segregation show a deviation from the measurements, the model predicts qualitatively the local volume fraction of the eutectic structure distribution.

In view of the above results, more quantitative comparison could certainly be reached with a 3D model including the effect of convection induced by the electromagnetic field as well as the non symmetric behavior of the development of the mushy zone.

III.6 Acknowledgment

This work was conducted within a European Space Agency project of the Microgravity Applications Promotion program (contract 15236/02/NL/SH). Contributions from S. Jacomet, B. Triger and M. Repoux are acknowledged. Samples were processed using electromagnetic levitation by Th. Volkmann and D. Herlach at the Deutsches Zentrum für Luft- und Raumfahrte.V., Köln, Germany.

III.7 Reference

[1] Beckermann C., Int. Mater. Rev. 47 (2002) 243-261.

[2] Rappaz M., Int. Mater. Rev. 34 (1989) 93-123.

[3] Herlach D. M., Annual Review of Materials 1991; 21:23.

[4] Volkmann T., Herlach D. M.. Steel Research Int. 2007; 78:426.

[5] Kasperovich G., Volkmann T., Ratke L., and Herlach D. Metallurgical Transactions A 2008, 39:1183.

[6] Heringer R., Gandin Ch.-A., Lesoult G., Henein H. Acta Materialia 2006; 54:4427.

[7] Prasad A., Henein H., and Conlon K.T., Metallurgical Transactions A, v.37, n.5, 2006, pp 1589-96.

[8] Gandin Ch.-A., Mosbah S., Volkmann Th., Herlach D.M. Acta Materialia 2008; 56:3023.

[9] Rappaz M., Thévoz Ph. Acta Metallurgica 1987; 35:2929.

[10] Wang C. Y., Beckermann C. Metallurgical Transactions A 1993; 24:2787.

[11] Wang C. Y., Beckermann C. Materials Science and Engineering A 1993; 171:199.

[12] Martorano M.A., Beckermann C., Gandin Ch.-A. Metall. mater. trans. 34A (2003) 1657.

[13] Guillemot G., Gandin Ch. -A., Bellet M. Journal of Crystal Growth 2007; 303:58.

[14] Gandin Ch.-A., Rappaz M., Acta metall. 42 (1994) 2233-46.

[15] Gandin Ch.-A., Rappaz M., Acta mater. 45 (1997) 2187-95.

[16] Herlach D., Gandin Ch.-A., Garcia-Escorial A., and Henein H.. Application for continuation of the MAP-Project : A98/99-023, (2004).

[17] Bellet M., Fachinotti V.D., Gouttebroze S., Liu W., Combeau H., in *Solidification Processes and Microstructures: A Symposium in Honor of Prof. W. Kurz*, Eds M. Rappaz, C. Beckermann, R. Trivedi, TMS, Warrendale, United States of America (2004) pp. 15-26.

[18] Liu W. , *Finite element modelling of macrosegregation and thermomechanical phenomena in solidification processes*, Ph. D. Thesis, Ecole Nationale Supérieure des Mines de Paris, Paris, France (2005).

[19] Prakash C. , Voller V. , Numerical Heat Transfer 15B (1989)171-189.

[20] M. Fortin, *Estimation d'erreur a posteriori et adaptation de maillages*, Revue Européenne des Eléments Finis 9 (2000) 467-486

[21] Alauzet F., Frey P.J. Rapport de Recherche INRIA mars 2003 ; N° 4759.

[22] Hamide M., Massoni E., Bellet M., Int J. Num Meth. Eng. 2008; 73:624.

[23] Gruau C., Coupez T., Computer Methods Appl. Mech. Engrg. 2005; 194:4951.

[24] Guillemot G., *Formation de structures de grains dans des alliages à solidification dendritique – modélisation couplée automates cellulaires et eléments finis,* Ph. D. Thesis, Institut National Polytechnique de Lorraine, Nancy, France (2004).

[25] Ivantsov G. P. , Doklady Akademii Nauk SSSR 58 (1947) 567.

[26] Kurz W., Fisher D.J., *Fundamentals of Solidification*, Third edition, Trans Tech Publications, Switzerland (1992).

[27] Mosbah S., Bellet M., Gandin Ch.-A. Solidification and Gravity 2008, conference proceedings; in press. Eds. A. Roósz et al. Materials Science Forum, Trans Tech Publications Ltd.

[28] Ch.-A. Gandin, J. Blaizot, S. Mosbah, M. Bellet,G. Zimmermann, L. Sturz,D. J. Browne, c, S. McFadden,H. Jung, B. Billia, N. Mangelinck, H. Nguyen Thi, Y. Fautrelle, e, X. Wang. , conference proceedings; in press. Eds. A. Roósz et al. Materials Science Forum, Trans Tech Publications Ltd.

[29] Mosbah S., Gandin Ch.-A., Brogly J., Crozier B., Volkmann Th., Herlach D. Proceedings of the 5th Decennial International Conference on Solidification Processing 2007; 80. Ed. H. Jones. The University of Sheffield, U. K.

[30] Sarreal J. A., Abbaschian G. J. Metallurgical Transactions A 1986; 17:2063.

III.8 Figure

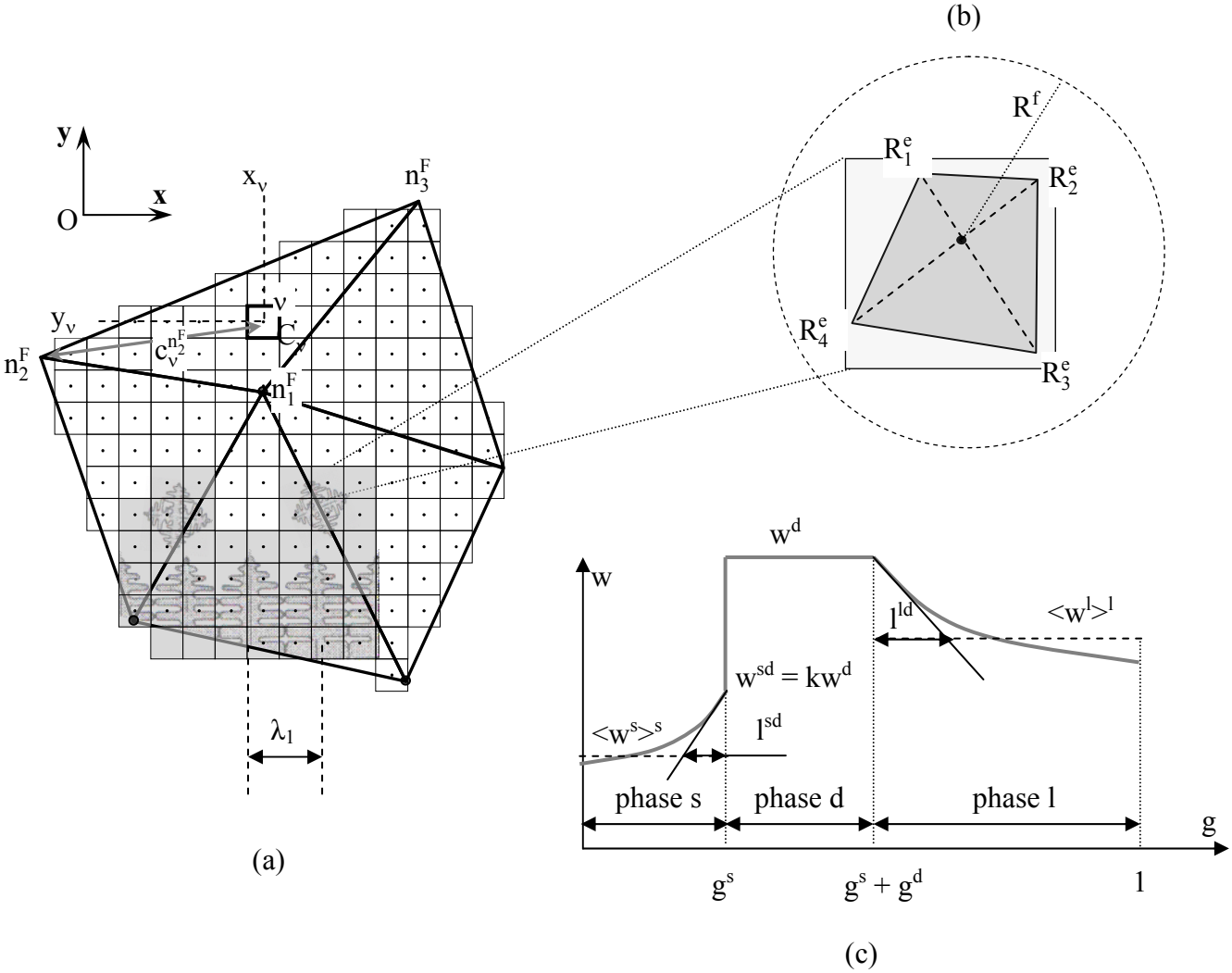

Figure 1. A Schematic view of the CA embedded microsegregation model: (a), illustration of the coupled cellular automaton−finite element model where cell painted in grey are a mushy cell, mixture between the liquid and solid phase, and give a spatial approximation of the developed dendritic structure. Typical dendritic length scale is also shown for both columnar and equiaxed grains. (b), Used model of the growth of the dendritic arms, R_i^e {i = 1, 2, 3 and 4}, up to a final position, $R^f = \lambda_1/2$. (c), is the solute profile and diffusion length in the solid phase, l^{sd}, and in the liquid phase, l^{ld}. The liquid phase, l, is assumed to exchange solute only with the intra-dendritic liquid phase. Equilibrium is assumed at the solid – interdendritic liquid phase, i.e. $w^{sd} = kw^d$.

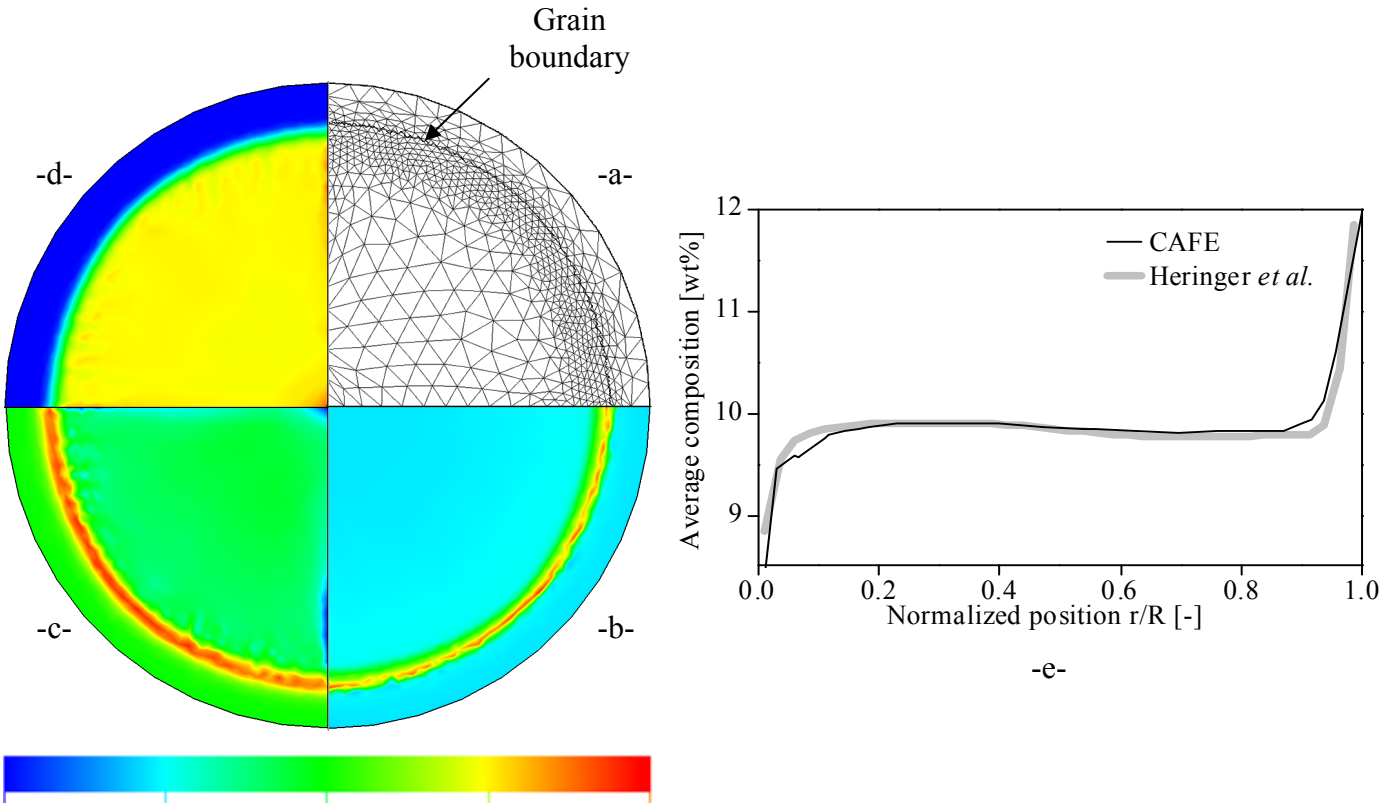

					a	FE mesh + Grain boundary
889	889.87	890.25	890.62	891	b	Temperature [K]
9	9.5	10	10.5	11	c	Average composition [wt%]
0	0.1	0.2	0.3	0.4	d	solid fraction [-]
					e	Final solute profile

Figure 2. 2D CAFE model simulation results for the solidification of an atomized Al-10wt%Cu droplet. A single nucleation event is assumed at the center of the spherical domain with 30K undercooling. Simulation is carried out for a quarter of a disk in axisymmetric coordinates with a radius equal to 125 µm. Maps are drawn when the volume fraction of the grain is about 0.64 [-] (calculated as the ratio of the grain volume over the simulation domain volume). The top left shows: (a) the finite element mesh and the CA growth front (black line), (b) the temperature, (c) the average composition, and (d) the volume fraction of solid phase. In addition, the final solute profile predicted by the CAFE model, black line, is compared to the Heringer et al model prediction, (e).

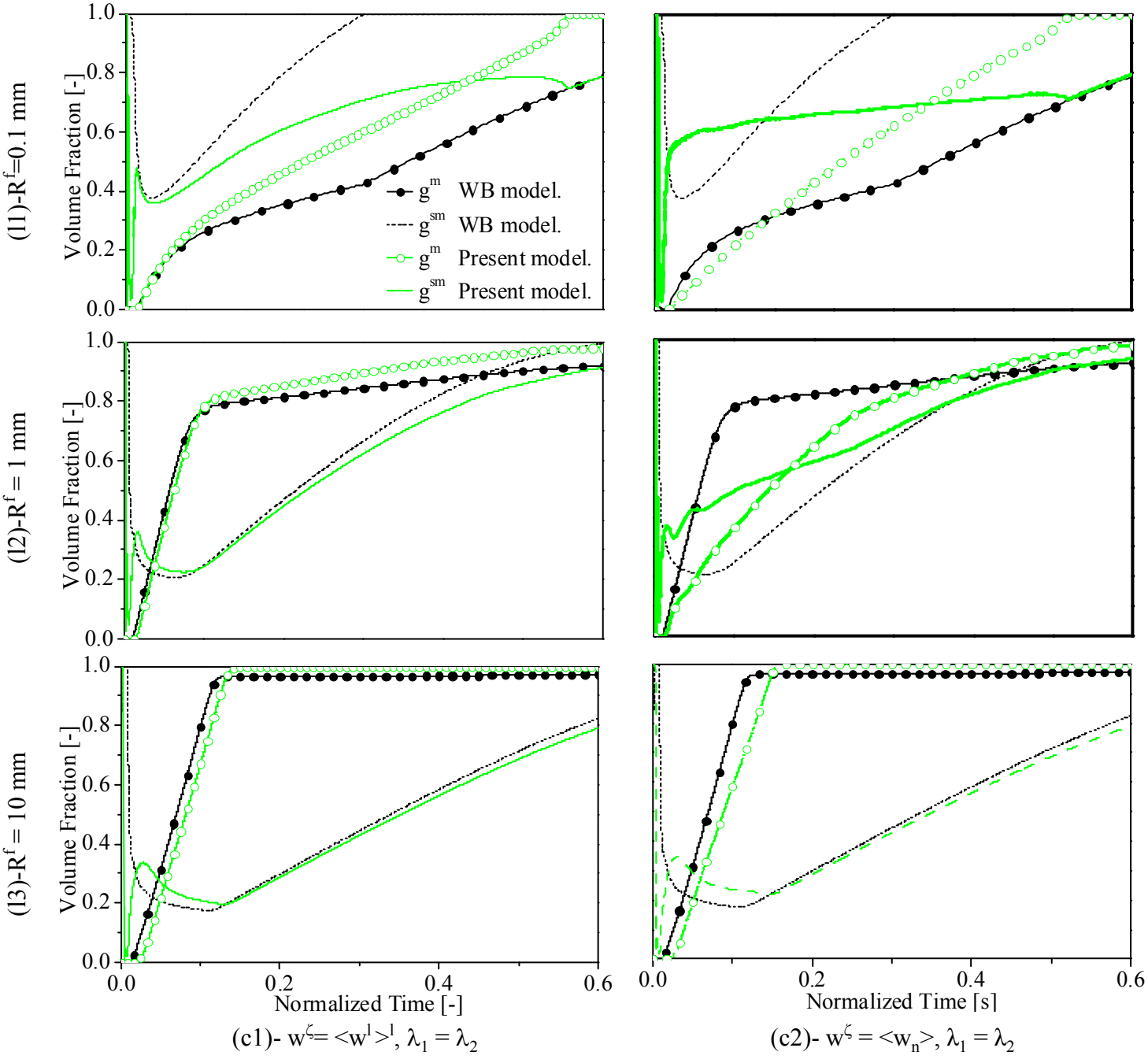

Figure 3: Present model and the Wang and Beckermann model [10] predictions of the temporal evolution of the mushy zone, g^m, and the volume fraction of the internal solid phase, g^{sm}, for three Al-4wt%Cu alloy equiaxed grains with a final radius R^f = 0.1, 1 and 10 mm. In the presented simulations, the initially liquid system exchanges heat by convection with a constant and equal heat transfer coefficient, h= 27 $Wm^{-2}K^{-1}$, with an homogenous external temperature, T_∞= 293 K, through the final grain radius, R^f. Calculations are achieved for $\lambda_1 = \lambda_2$ when the average composition of the extra-dendritic liquid phase is used, $w^\zeta = \langle w_v^l \rangle^l$, and when the average composition of the CA defining the mushy zone front is used, $w^\zeta = \langle w_v \rangle$, for the calculation of growth rate. The solidification time, t_s, used for normalization are 3, 40 and 300 [s] for respectively R^f = 0.1, 1 and 10 mm.

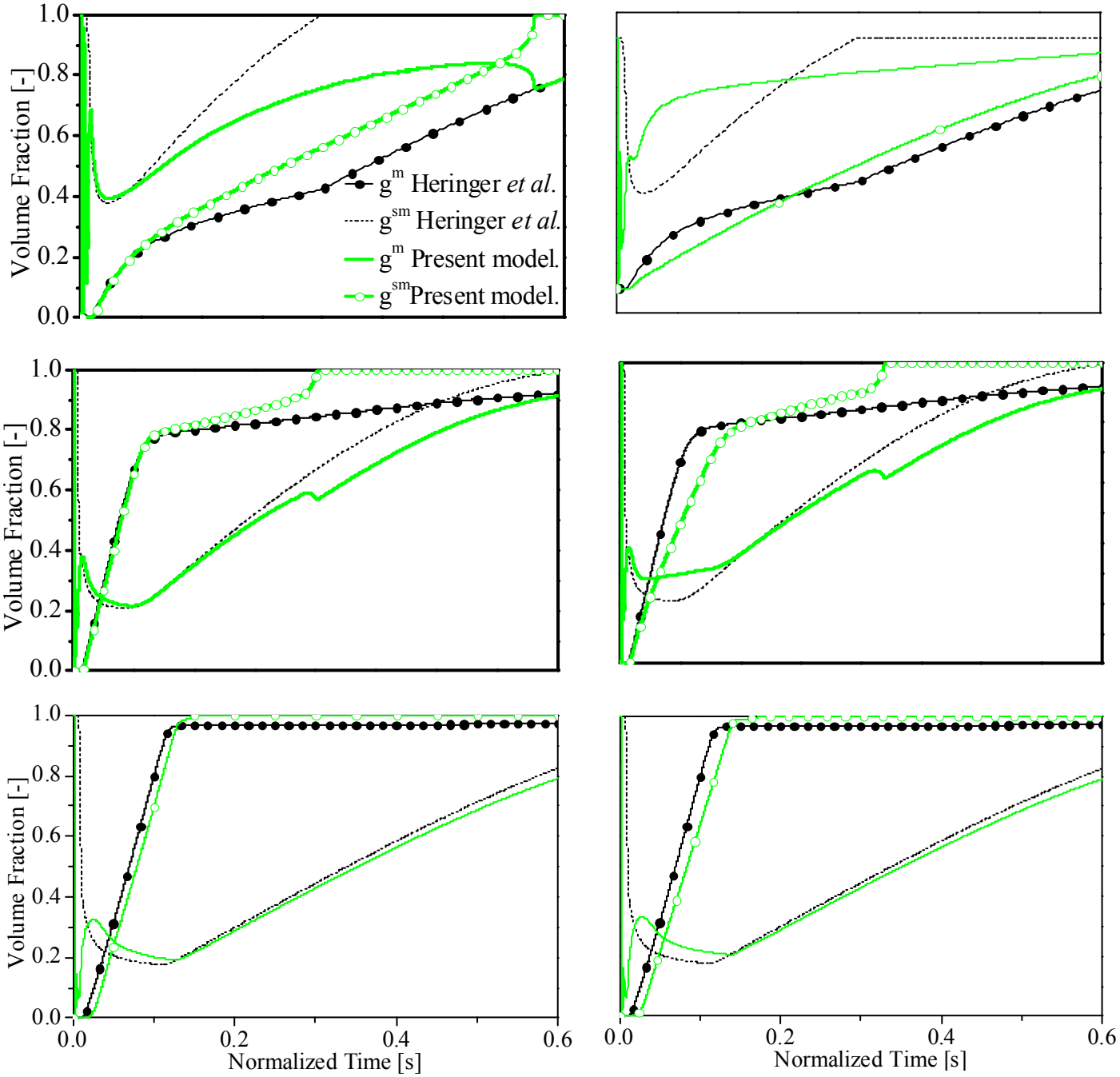

(c1)- $w^{\zeta} = \langle w^{l} \rangle^{l}$, $\lambda_1 = 4\lambda_2$ (c2)- $w^{\zeta} = \langle w_n \rangle$, $\lambda_1 = 4\lambda_2$

Figure 4: The same as Figure 3 with the analysis of the effect of the primary dendrite arm spacing on the model predictions, green curves, compared to the Wang and Beckermann [10] model, black curves.

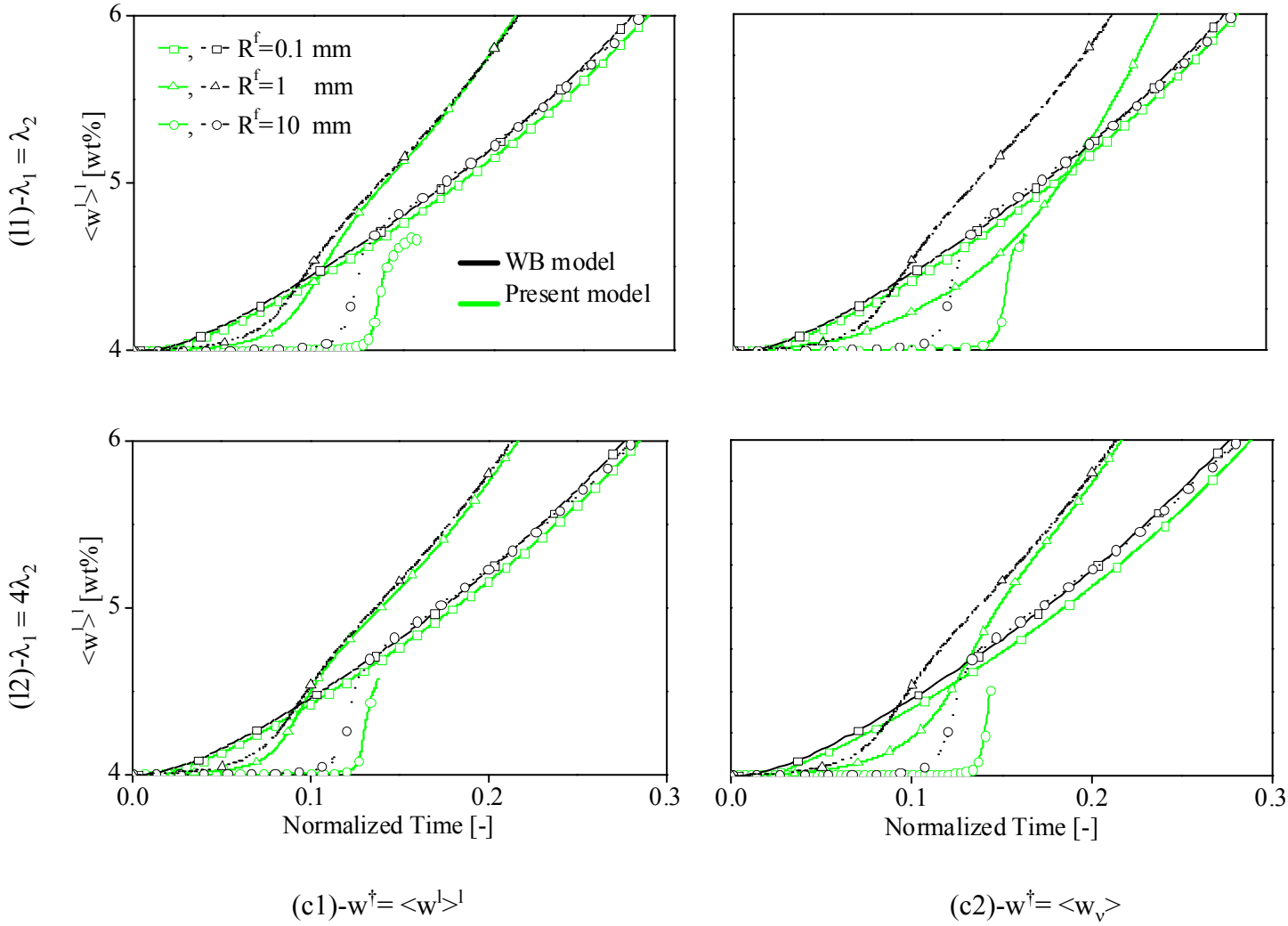

Figure 5: Effect of the primary dendrite arm spacing, λ_1, as well as the calculation approach of the growth rate, effect of $w^{\dagger}$, on the solute diffusion in the extra-dendritic liquid phase. Present model, green curves, and the Wang and Beckermann [10] model, black curves, prediction of the temporal evolution of the average composition of the extra-dendritic liquid, for three equiaxed grains with a final radius of 0.1, 1 and 10 mm. the equivalent spherical shape of the grain is simulated of an Al4wt%Cu alloy. Grains exchange heat by convection with a constant and equal heat transfer coefficient, h=27 W m^{-2} K^{-1}, with a homogenous external temperature, T_{∞}= 293 K, through its final radius, R_f. The effect of the primary dendrite arms spacing is analyzed, comparing line 1 and 2, as well as the calculation of the growth rate, comparing column 1 and 2. Curves are drawn until the mushy zone reach the boundary limit, i.e. g^m = 1. The solidification time, t_s, used for normalization are 3, 40 and 300 [s] for respectively R^f = 0.1, 1 and 10 mm.

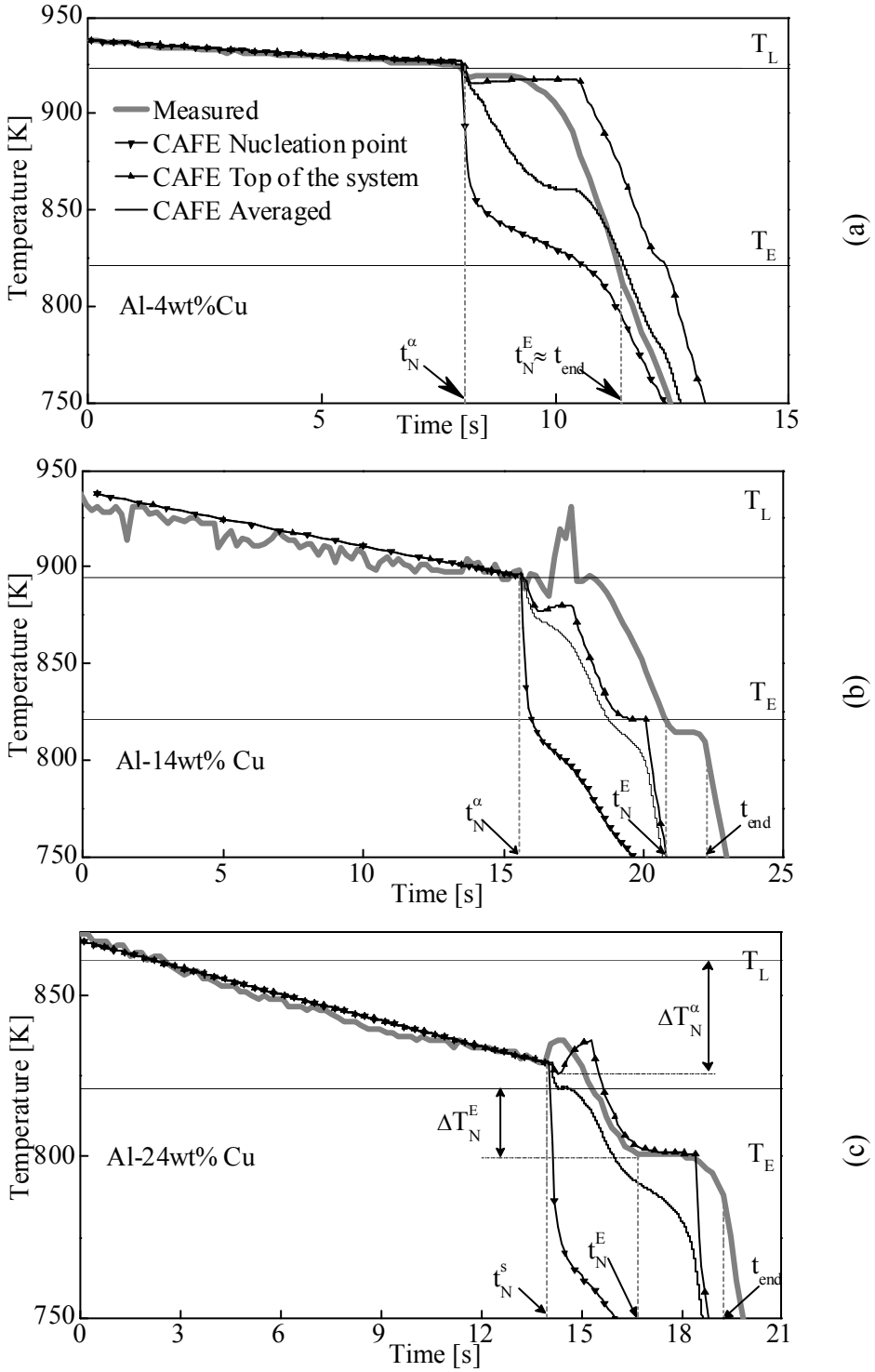

Figure 6: Measured temperature, thick grey curves, for the Al- 4, 14 and 24wt%Cu droplets with triggered nucleation together with the predicted averaged system temperature by the present model, black curves. The predicted temperature at the bottom, -▼-, and at the top, -▲-, of the simulation domain are also drawn. Measurements have been achieved using an optical pyrometer at the top of the system. For the Al-24wtCu, nucleation undercooling for the primary solid phase, ΔT_N^α = 32 K, as well as for the eutectic structure, ΔT_N^E =20 K, have been measured. No undercooling is considered for the Al-4 and 14wt%Cu droplets. Isothermal eutectic transformation is assumed at the measured nucleation temperature for all samples.

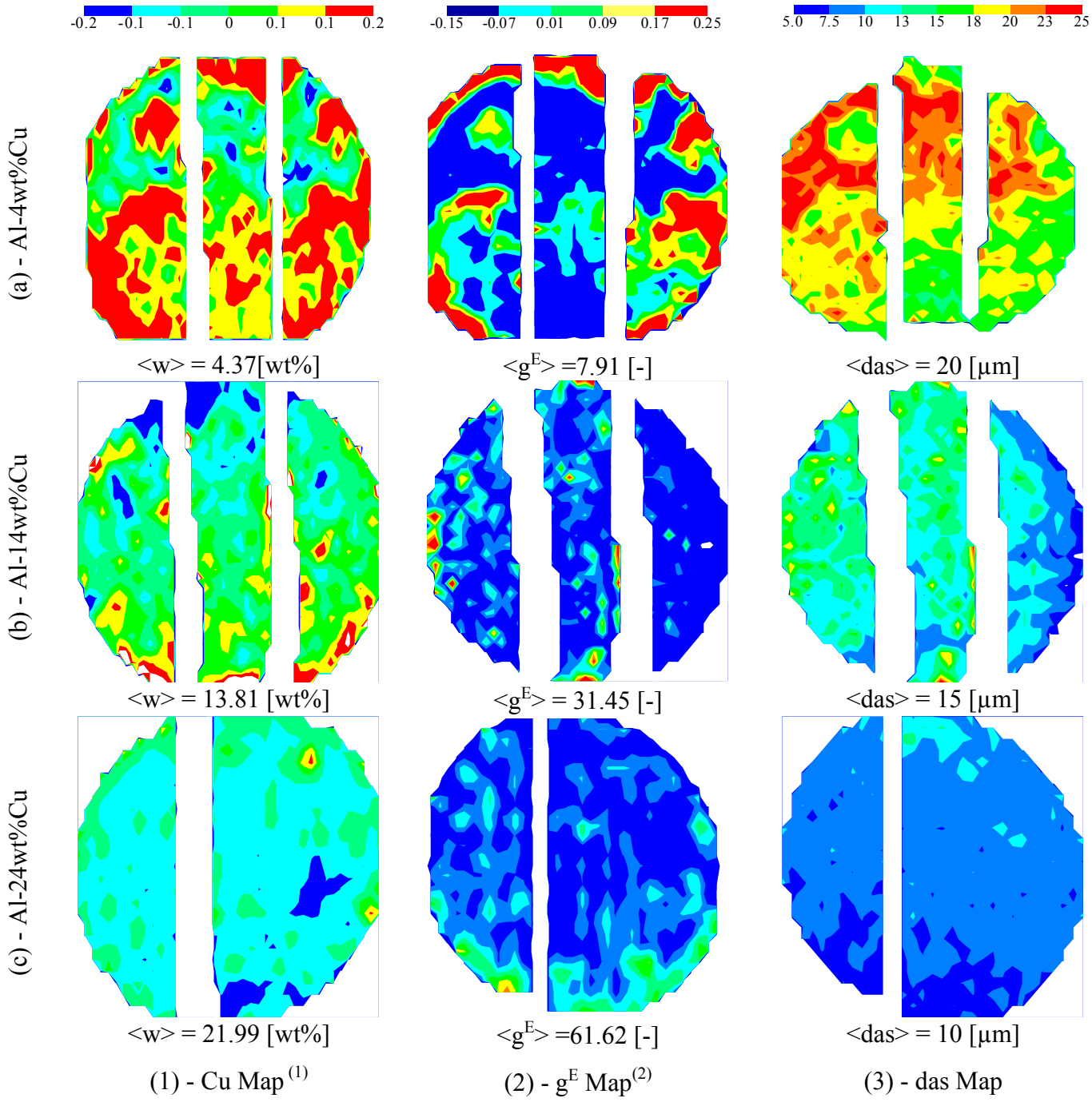

Figure 7: Characterization of a central meridian cross section of aluminum-copper samples processed by electromagnetic levitation with triggered nucleation for the Al- 4 , (a), 14 , (b), and 24wt%Cu, (c), droplet. (a). Distribution of (1) the normalized average copper content, $(w-w_0)/w_0$ [-], (2) the normalized average eutectic fraction, $(g^e-g^e_{GS})/g^e_{GS}$ [-] and (3) the dendrite arm spacing, DAS [µm]. (1) Measurements of the average copper content, w, is averaged over $120\cdot10^{-6}$ m × $150\cdot10^{-6}$ m surface areas. (2) Measurements of the volume fraction of the eutectic structure, g^e, is average over $150\cdot10^{-6}$ m × $150\cdot10^{-6}$ m surface areas.

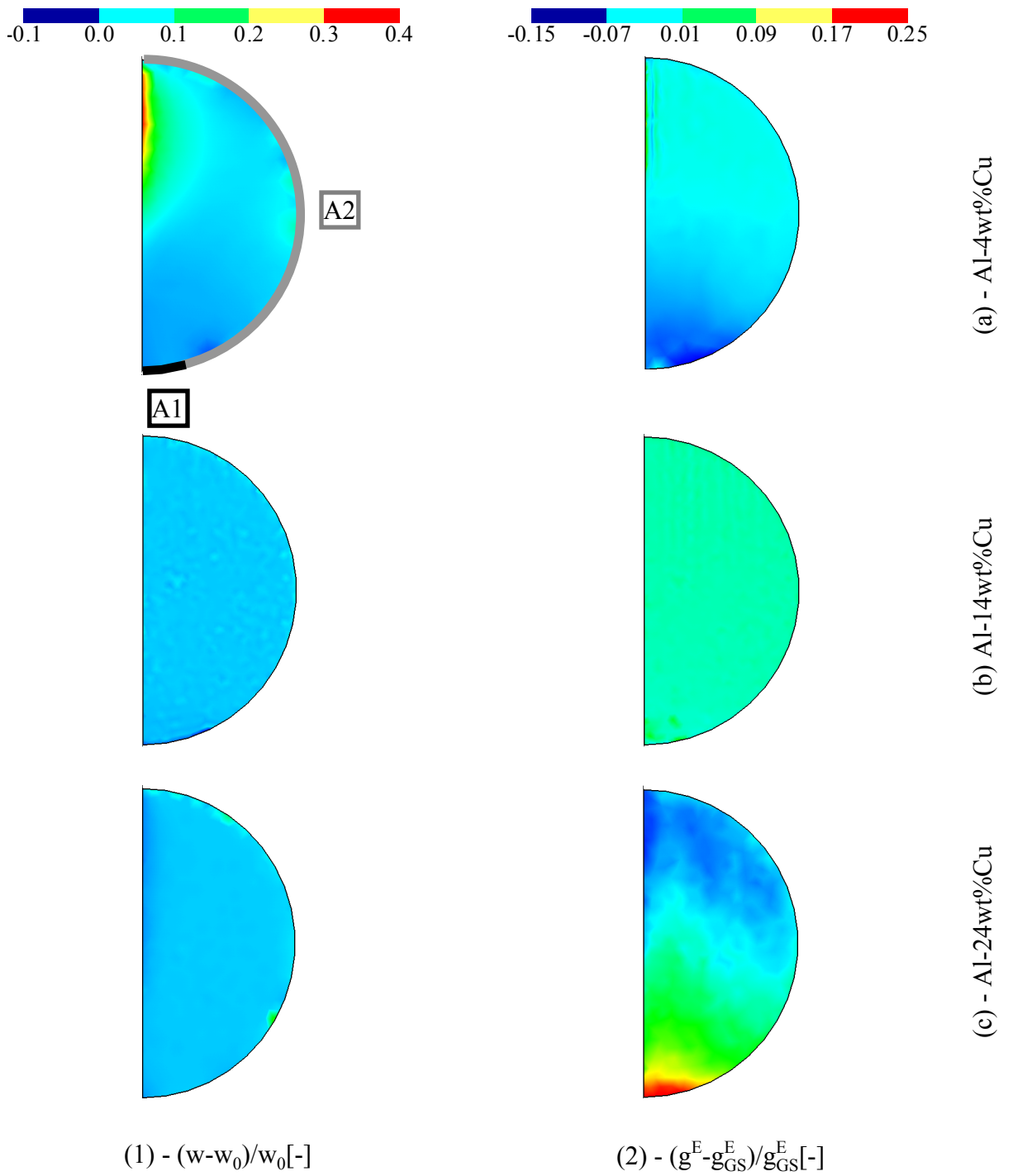

Figure 8: Prediction of the present model for the Al-Cu samples processed by electromagnetic levitation. Maps present, (1) the distribution of the normalized average copper content, $(w-w_0)/w_0$ [-], and (2) the eutectic volume fraction, $(g^E-g^E_{GS})/g^E_{GS}$, [-] when solidification is completed. g^e_{GS} is the volume fraction of the eutectic phase predicted by the Gulliver – Scheil model for the nominal composition, w_0, given in Table 2. Thick black curvature indicates the contact area of the alumina plate at the bottom of the droplet surface simulated with the model as a constant surface, A1. Heat is also extracted through the droplet free surface, thick grey line, A2, as explained in the *Prediction* section.

III.9 Table

l^{sd}	$\lambda_2/6 \cdot \frac{g_v^s}{g_v^m}$
S^{sd}	$\lambda_2/2$
l^{ld}	$\frac{R^{e^3}}{R^{f^2} - R^{e^2}} \times \left(\frac{R^{f^2}}{R^{e^2}} E_1(P_e - E_1\left(P_e \frac{R^f}{R^e}\right)\exp(P_e) - \frac{P_e + 1}{P_e^2} + \exp\left(P_e\left(1-\frac{R^f}{R^e}\right)\right)\left(\frac{R^f}{P_e R^e} + \frac{1}{P_e^2}\right)\right)$
S^{ld}	$3R^{e\,2}/R^{f\,3}$

Table 1: Mathematical expressions used for the diffusion layer lengths, l^{sd} and l^{ld}, as well as for the interfacial concentration, S^{sd} and S^{ld}, entering equations 5, 6 and 7.

.

w_0[wt%]	Nucleation	ΔT_N^{α}[°C]	ΔT_N^{E}[°C]	Solidification time[s]	$\dot{T}(t<t_N^{\alpha})$	$\dot{T}(t>t_{end})$
4	Triggered	-	-	3.2	-1.5	-64.
	spontaneous(1)	35	20	41.5	-6.6	-
14	Triggered	-	-	5.1	-3.24	-74.
	spontaneous(1)	15	20	63.7	-6.9	-
24	Triggered	32.	20.	3.0	-3.51	-71.
	spontaneous(1)	25	45	88.2	-4.5	-

Table 2: Summary of the measurements deduced from the recorded cooling curves for the six Al-Cu samples processed using electromagnetic levitation. Composition, w_0, cooling rates, $\dot{T}(t<t_N^{\alpha})$ and $\dot{T}(t>t_{end})$, nucleation undercooling of the dendritic and eutectic structures, ΔT_N^{α} and ΔT_N^{E}, solidification times measured from nucleation of the dendritic structures, t_N^{α}, up to completion of the solidification, t_{end}.

w_0 [wt%]	Nucleation	w_D [wt%]	DAS_D [μm]	g_D^E [%]	g_{Gan}^E [%]	g_P^E [%]	$g_{GS}^{E\ (1)}$ [%]
4	Triggered	4.37	20	7.91	-	7.36	7.81
	spontaneous	4.14	30	5.6	5.62	6.8	
14	Triggered	13.81	15	31.45	-	34.6	35.33
	spontaneous	12.74	25	29	32.15	33.48	
24	Triggered	21.99	10	61.62	-	65.	67.64
	spontaneous	20.7	15	57.2	57.5	67.	

Table 3: Summary of measurements deduced from composition measurements (SEM-EDS) and image analyses and present model predictions, g_P^E, and Gandin et al [8] model predictions g_{Gan}^E. (1) Calculated with w_0 and the data of the phase diagram given in Table 2).

Volumetric enthalpy of fusion, L [J m^{-3}]	10^9	Domain radius, R [m]	$2.65 \cdot 10^{-3}$
Volumetric heat capacity, C_p [J m^{-3} K^{-1}]	$3. \cdot 10^6$	External temperature, T_{ext} [K]	293.
Eutectic temperature, T_E [K]	821	Droplet contact surface with the trigger, A1 [m^2]	4.5 10^{-6}
Eutectic composition, w_E [wt%]	33.2	Free droplet surface, A2 [m^2]	83.75 10^{-6}
Segregation coefficient, k [-]	0.17	Cell size [µm]	10
		Imposed minimum FE mesh size [µm]	30
Diffusion of Cu in solid Al, D^s [m^2 s^{-1}]	$5 \cdot 10^{-13}$	Imposed maximum FE mesh size [µm]	200
Diffusion of Cu in liquid Al, D^l [m^2 s^{-1}]	4.376 10^{-9}	Objective relative error used for FE mesh adaptation on [-]	10^{-4}

Sample	Liquidus temperature, T_L [K]	Heat transfer coefficient, h(t) [W m^{-2} K^{-1}]				Initial temperature, T(t=0s) [K]
		$h(t<t_N^{\alpha})^{(1)}$		$h(t>t_N^{\alpha})^{(2)}$		
		A1	A2	A1	A2	
14wt%Cu	923.	6.4		10000	6.4	938
14wt%Cu	895.	12			12	938
24wt%Cu	861.	13			13	867

Table 4: Values for the properties for the Al-Cu alloys samples, size, initial and boundary conditions for the simulations. [(1)] Adjusted to fit measured T_N^s at t_N^s (Figure 6). [(2)] Adjusted to fit measured cooling rate at t_{end} (Figure 6).

Résumé en Français :

Chapitre IV Modeling of Macrosegregation and Macrostructure upon Solidification of an Sn-Pb Alloy in a Rectangular Cavity

Le modèle couplant automate cellulaire et éléments finis présenté au chapitre III est appliqué à un cas test de référence. Le cas test considéré est une expérience de solidification d'une cavité rectangulaire d'alliage étain–plomb de composition 10pds% plomb. Le modèle et la procédure expérimentale sont d'abord présentés suivis d'une description du modèle numérique développé.

Les équations de conservation d'énergie, de composition et de quantité de mouvement sont résolues par la méthode des éléments finis. Le couplage avec l'automate cellulaire permet de tenir compte des phénomènes à l'échelle des structures de grains. La méthode d'adaptation de maillage est décrite plus en détails. Le modèle permet de prédire les cartes de composition, de température au cours du temps et la structure de grains finale.

Un ajustement des coefficients d'expansion thermique, de la chaleur latente de fusion ainsi que de la masse volumique permet une prédiction plus quantitative des cartes de températures mesurées. Ces ajustements permettent de réduire la convection d'origine thermique résultant d'une composition non uniforme en plomb du domaine initialement totalement liquide dans l'expérience.

Chapter IV Modeling of Macrosegregation and Macrostructure upon Solidification of an Sn-Pb Alloy in a Rectangular Cavity

Abstract

A two dimensional (2D) cellular automaton (CA) – finite element (FE) model for the prediction of macrostructure and macrosegregation is applied to a benchmark experiment. The experiment consists of a Sn-10wt%Pb alloy solidified in a 6 cm height × 10 cm width × 1 cm thick rectangular cavity. The global temperature history of the cavity is achieved by a precise control of the heating/cooling rates applied to two lateral heat exchangers in contact with the 6 cm × 1 cm vertical surfaces. The temperature difference between the two heat exchangers also defines the global horizontal temperature gradient imposed through the 10 cm width cavity. All other surfaces are made adiabatic. *In-situ* temperature measurements during solidification are conducted with 50 thermocouples embedded in the crucible defining one of the 6 cm × 10 cm surfaces. The thermocouples are distributed onto a two-dimensional array defined by 5 lines × 10 columns regularly spaced by 1 cm in both the vertical and horizontal directions. The thermocouples give access to a sequence of instantaneous temperature maps. The as-cast state is also characterized at the location defined by each thermocouple by the measurement of the average copper composition using inductively coupled plasma spectrometry; as well as by etchings to reveal the metallographic features. Simulation with the 2D CAFE model is performed with the goal to achieve direct comparisons with maps of temperature, macrosegregation and grain structure. A satisfying overall agreement is reached providing an adjustment of unknown material parameters. Deviations between the predictions and the measurements could be overcome with the integration of grain movement, not available in the present model.

Keywords

Solidification, Modeling, Segregation, Structure, Benchmark, Finite element, Cellular Automaton

IV.1 Introduction

Macrosegregation in casting is defined by the variation of the average chemical composition with respect to the nominal alloy composition. It is a considered as a defect of cast ingots because the alloy composition is mainly optimized to reach desired mechanical properties upon subsequent forming processes and/or thermomechanical heat treatments [1, 2]. Variations of composition are thus detrimental for the control of the distribution of the final properties in cast parts.

Extensive works have been developed to model macrosegregation. The first models are based on a numerical solution of the conservation equations assuming no transport of the solid phase and a simple lever rule approximation; i.e. full equilibrium between the solid and liquid mixture during solidification [3, 4]. More sophisticated approaches are yet necessary when solidifying alloys. Dedicated microsegregation models based on volume averaging and approximate solutal diffusion lengths have thus been developed for primary dendritic [5-9] and eutectic [10] solidification, considering a prescribed columnar or equiaxed grain morphology. Some validation could recently be achieved with a numerical solution developed for equiaxed growth [11]. Coupling was achieved for advanced modeling of macrosegregation with some success [12-14]. However, attempts to compare model predictions with experimental observations remain limited and always partly achieved [15-17]. The main limitations could be seen as the underestimated efforts necessary to achieve such comparisons. Not only a very well defined experiment is required, including a precise control of the boundary conditions and casting parameters, but also as much as possible measurements must be collected, during and after the solidification experiment, using in-situ and post-mortem characterizations. The alloy also needs to be well known with respect to the material parameters entering a casting simulation. Finally, because transition from columnar-to-equiaxed grain structure is a very common casting feature, models must be sufficiently advanced to handle it.

Recent experimental analyses make use of in-situ visualization of the development of the grain structure by X-ray radioscopic imaging –radiography– of metallic systems or by direct optical observation of solidifying transparent analogues [18-21]. It is directly suitable to follow the development of the dendritic grain structure and can give an evaluation of the melt composition based on image analysis of the grey levels. The long acquisition time required between two images yet limits its application to low solidifying rates in order to build a time sequence of the development of the structure. Optical observation of solidifying transparent analogues does not suffer from the later drawback [22]. While a composition map is not yet possible to deduce from the observation, particle image velocimetry can be performed for the determination of the liquid flow and to track the velocity of the equiaxed crystals. Recently, X-ray imaging experiments by Yin and Koster of a solidifying gallium – 5 wt% indium alloy in a 3.5 cm height × 5 cm large × 0.2 cm thick rectangular cavity was made available in the literature. Comparison of a simulation with a two dimensional (2D) cellular automaton (CA) – finite element (FE) model [23] could be achieved considering the time sequence of the development of the single grain structure together with indium macrosegregation in the liquid [24]. The progression and shape of the pure gallium solid phase was

found closely correlated to the segregation of indium into the liquid, also explaining the shape of the growth front. It is to be noted that, because solubility of indium in the primary solid gallium phase is nil, the microsegregation model simply reduces to lever rule approximation for an open system, which is the simplest possible solidification path to be used for modeling of macrosegregation. Although quantitative agreement was reached, this was only possible by fitting the growth kinetics of the gallium solid phase.

While comparison of casting simulations with experiments has long been based on comparing solely cooling curves measured by thermocouples, little progress is seen in the literature on applying concurrent measurement techniques such as infrared camera. The advantage would be to directly access time evolution of temperature maps. For this reason, as well as because the rectangular cavity experiment studied by Yin and Koster was inspired from the Sn–Pb alloys casting configuration proposed by Hebditch and Hunt more than 3 decades ago [25, 26], a new experimental set-up has been recently proposed by Wang et al [27]. It is based on detailed measurements of temperature maps and throughout post-mortem characterizations of casting and will be presented hereafter. In parallel, a microsegregation model accounting for solute diffusions in the solid and in the liquid phases has been implemented into the CA model [28, 29]. It is integrated into a 2D FE model that permits mesh adaptation based on the average composition field and the liquid velocity. Comparison of the 2D CAFE simulation of the new experiment of a Sn - 10 wt% Pb alloy solidification in a 6 cm height × 10 cm large × 1 cm thick rectangular cavity is presented in this contribution.

IV.2 Experiment

IV.2.1 Experimental apparatus.

A set-up has been designed to study macrosegregation induced by thermosolutal buoyancy forces. It is heavily inspired by the Hebditch and Hunt experimental configuration [25, 26]. As schematized in Figure 1, a parallelepiped casting geometry -rectangular cavity- is used with dimensions 6 cm height × 10 cm width × 1 cm thick. The largest vertical surfaces of the casting, 6 cm × 10 cm, are enclosed by 0.5 mm thick steel sheets that serve as crucible walls. The bottom and top horizontal surfaces of the casting, 10 cm × 1 cm, are made of insulating materials with the objective to reach adiabatic conditions. Such conditions are also targeted for the largest vertical surfaces using a Kirchhoff box to compensate heat losses by radiation while natural convection by air is suppressed by installing the entire set-up in a chamber with a vacuum pressure of the order of 10^3 Pa. The smallest vertical surfaces of the casting, 6 cm × 1 cm, are in contact with heat exchangers made of copper.

IV.2.2 In-situ measurements.

The temperature histories of the left-hand-side and right-hand-side heat exchangers are precisely controlled and measured with several thermocouples in order to achieve a desired heating or cooling history of the smallest vertical casting surfaces. The thermocouples used in the present study are labeled as TL and TR in Figure 1. Constant heating rate or cooling rates, as well as simple holding temperature, can be imposed. A total of 50 K-type thermocouples are welded with one of the steel sheet for *in-situ* temperature measurements during the experiment. The thermocouples are distributed onto a two-dimensional array defined by 5 lines × 10 columns regularly spaced by 1 cm in both the vertical and horizontal directions, as schematized by dots in Figure 1. Labeling in Figure 1 is only provided for the thermocouples located in the first and last columns. Other thermocouples are welded on the opposite steel sheet so as to verify the uniformity of the temperature during the experiment.

IV.2.3 Alloying.

The system chosen for the study of solidification is a tin – 10 wt% lead alloy; i.e. the nominal lead composition is $w_0 = 10$ wt%. It is first prepared from a mixture of pure tin and pure lead melted and homogenized in a quartz crucible using an electromagnetic field. The casting geometry is then provided by a simple pouring procedure in a water cooled cooper mold with final dimensions given above, i.e. 6 cm height × 10 cm width × 1 cm thick. Properties of the alloy are summarized in Table 1. The liquidus and eutectic temperature are $T_L = 219$ °C and $T_E = 183$ °C, respectively. A discussion on the values will be provided later.

IV.2.4 Experimental procedure.

The solid ingot integrated into the experimental apparatus is first melted and maintained in a liquid state during 1000 s. Sufficient time is thus allowed for temperature homogenization at a prescribed temperature of 250 °C as can be checked with the numerous thermocouples. A temperature gradient of 200 °C m^{-1} is then imposed through the liquid by increasing the temperature of the right-hand-side heat exchanger, measured at TR, up to 270 °C with a heating rate of 0.02 °C s^{-1}. After a holding period of about 500 s, a cooling rate of -0.03 °C s^{-1} is imposed on both heat exchangers, measured at TL and TR, while maintaining the initial 20 °C temperature difference, thus leading to solidification of the alloy and a global temperature gradient of 200 °C m^{-1} within the 10 cm width ingot.

IV.2.5 Post-mortem analyses.

In addition to the in-situ measurement of the temperature maps, a chemical etching of the surfaces of the ingot is performed to reveal the grain structure. Average dendrite arm spacing over the entire domain is also reported in Table 1. The average composition map of lead in the as-solidified ingot is provided using the same array of 50 measurement points schematized in Figure 1. For that purpose, metallic particles are produced by drilling holes. The samples are then analyzed using inductively coupled plasma spectrometry to give access to lead compositions.

A more complete description of the experimental apparatus is provided elsewhere [27].

IV.3 Modeling

A finite element (FE) method solving average conservation equations is coupled with a cellular automaton (CA) method to simulate the development of the dendritic grain structure [16, 23, 24]. Recent achievements concern the integration of an advanced microsegregation model to convert average enthalpy and composition into phase fractions, phase compositions and temperature. Such conversion is applied at the scale of each CA cell and accounts for diffusion in both the solid and liquid phases. However, these new developments were only applied to diffusion-based segregation so far [28, 29]. Hereafter, we first give a short summary of the FE model [4] prior to present its extension to integrate a mesh adaptation method for the computation of segregation induced by both solute diffusion and thermosolutal buoyancy forces at the origin of liquid flow during mushy zone solidification. The model is fully based on the approximation of constant and equal densities of the solid and liquid phases as well as a fixed solid phase. In addition, a Cartesian two dimensional representation of the casting domain is considered. Such an approximation is valid considering the careful design of the experimental apparatus with respect to heat flow and was justified in a similar casting configuration despite the existence of a liquid velocity profile throughout the thickness of the ingot [30, 31].

IV.3.1 Total mass conservation.

In the following, $\mathbf{v} = g^s \mathbf{v}^s + g^l \mathbf{v}^l$ is the average macroscopic flow velocity. Furthermore assuming a fixed solid phase, i.e. a zero velocity of the solid phase, $\mathbf{v}^s = 0$, leads to $\mathbf{v} = g^l \mathbf{v}^l$ where g^l is the volumetric fraction of the liquid phase and $\mathbf{v}^l$ is the average velocity of the liquid phase. Only two phases are supposed to coexist in a mushy zone so that the liquid phase is progressively transformed into a solid phase of fraction g^l with $g^s + g^l = 1$. Hence, the average total mass conservation writes:

$$\nabla \cdot \mathbf{v} = 0 \tag{1}$$

IV.3.2 Momentum conservation.

The average momentum conservation writes:

$$\rho_0 \frac{\partial \mathbf{v}}{\partial t} + \frac{\rho_0}{g^l} \nabla \cdot (\mathbf{v} \times \mathbf{v}) = \nabla \cdot (\mu \nabla \mathbf{v}) - g^l \nabla p + g^l \rho \mathbf{g} - \frac{\mu}{K} g^l \mathbf{v} \tag{2}$$

where μ is the dynamic viscosity, p is the intrinsic pressure in the liquid, $\mathbf{g}$ is the gravity vector, K is the permeability and t is the time. The permeability is calculated thanks to the Carman-Kozeny relation [3] considering an isotropic mushy zone domain: $K = (g^{l\,3} \lambda_2^{\,2}) / (180\,(1-g^l)^2)$, where λ_2 is the dendrite arm spacing.

The buoyancy forces are integrated in the FE model as proposed Bellet et al [4]. The Boussinesq approximation is introduced to compute the fluid flow induced macrosegregation. Hence, the liquid density is constant and equal to ρ_0 in all terms of the momentum equation, except for the gravity term where it is replaced by a function of the local solute composition in the liquid phase, w^l, and the local temperature, T, as follows:

$$\rho = \rho_0 \left[1 - \beta_T (T - T_0) - \beta_w (w^l - w_0^l)\right] \quad (3)$$

where β_T and β_w are the thermal and solutal expansion coefficients, respectively. References used to define the variations of the liquid density with the local solute composition in the liquid phase and the local temperature are T_0 and w_0^l, respectively.

IV.3.3 Energy conservation.

The average energy conservation writes:

$$\rho_0 \left(\frac{\partial H}{\partial t} + \mathbf{v}\cdot\nabla H^l\right) - \nabla\cdot\left(\kappa\,\nabla T\right) = 0 \quad (4)$$

where H is the average enthalpy per unit mass and H^l is the average enthalpy of the liquid phase per unit mass. Additionally assuming constant and equal values of the specific heat for the liquid and solid phases, C_p, one can write: $H = C_p\,[T - T_{ref.}] + g^l\,\Delta_s^l H_f$ and $H^l = C_p\,[T - T_{ref.}] + \Delta_s^l H_f$, where $\Delta_s^l H_f$ denotes the latent heat of fusion per unit mass and $T_{ref.}$ is a reference temperature, the later not being used explicitly in the integration of the equations. An average thermal conductivity, κ, is also considered. In the present model, however, it is only dependent of the temperature, only linear interpolation being applied between tabulated values.

IV.3.4 Solute conservation.

The average conservation of the mass of a solute element in a binary alloy writes:

$$\frac{\partial w}{\partial t} + \mathbf{v}\cdot\nabla w^l - \nabla\cdot\left(D^l\,g^l\,\nabla w^l\right) = 0 \quad (5)$$

where w is the average composition of solute and w^l is the average composition of solute in the liquid phase. D^l is the diffusion coefficient of the solute element in the liquid phase.

IV.3.5 Mesh adaptation.

The Prandtl number, $Pr = \nu/\alpha$, and the Schmidt number, $Sc = \nu/D$, characterize the ratios of the kinematics viscosity, $\nu = \mu/\rho_0$, over the thermal diffusivity, $\alpha = \kappa/(\rho_0 c_p)$, and chemical diffusion, D. The ratio of these two quantities is known as the Lewis number, $Le = Sc/Pr = \alpha/D$. Values of these non-dimensional numbers can be derived for the liquid state from the data listed in Table 1. As is usual in metallic alloys, solute diffusion is found limited compared to heat diffusion (large value of the Lewis number). The diffusion length characterizing solute transport in the liquid is thus expected much smaller than for heat transport. Interaction of the fluid flow with the solute flow also takes place on a smaller scale compared to heat flow (Sc much larger than Pr). Consequently, while choosing the strategy to keep a single FE mesh to solve all above conservation equations, an adaptation of the mesh size is required where the gradient of solute and the gradient of the liquid velocity are enhanced during solidification. This is particularly true ahead of growing mushy zones where the liquid velocity field can abruptly change and solute layers can built up due to segregation. Because the adaptation of such a fixed mesh size would drastically increase the required computer

memory and the computation time, an optimization of the FE mesh is implemented in the model, which is explained hereafter.

The FE mesh adaptation approach developed by Alauzet and Frey [32] has been adopted. It consists of a minimization method that evaluates the mesh size required to access a given error for a chosen field to be computed onto the FE nodes. Let's denote u the exact solution of a scalar field, we consider it's approximation, u_h, and the matrix of second spatial derivative of u, $G_u(x)$, at a point x inside the triangular element F. Using the Cea's lemma [32], the error, $E_u = ||u-u_h||$, is estimated based on the interpolation error:

$$||u-u_h|| < c\ ||u-\Pi_h u|| \tag{6}$$

where, Π_h, is the linear interpolation of u on the mesh and c is a constant independent of the FE mesh. In case of a 2D FE formulation, Alauzet and Frey [32] demonstrate that the interpolation error, $E_u = ||u-u_h||$, in a given element is banded as follows:

$$E_u \leq 2/9 \max_{x\in F} \max_{e\in E_F} <e,|G_u(x)|e> \tag{7}$$

where E_F is the set of the edges of the triangle F. The main idea is to calculate a metric tensor M(F) for a given FE so that for any vector $e \in E_F$:

$$\max_{x\in F} <e,|G_u(x)|e> \leq <e,M(F)e> \tag{8}$$

Using the linearity of the Hessian over the triangular element, the tensor metric, M(F), is given by:

$$M(F)= \max_{p\in N_F} |G_u(p)| \tag{9}$$

where N_F is the set of the three nodes of element F. Hence, the mesh size can be controlled by a directional error estimator based on the recovery of the second derivatives of the FE solution. This strategy is known as the Hessian strategy. A given fixed objective error, E_u^{obj}, can be obtained over the simulation domain by considering the last right term in equation 8 together with equation 9 and generating the mesh such as:

$$\forall\ F,\ \forall e\in E_F,\ E_u^{obj} = c<e,M(F)e> \tag{10}$$

The Hessian matrix G_u of a given P1 field u, i.e. its gradient is constant on each F element, is calculated as proposed by Hamide et al [33], i.e. the second derivatives of the field u, at each node n, is reconstructed in two steps by using the computed solution from the patch S of all elements surrounding node n. In a first step we recover the gradient at node n by taking the volume weighted average of the gradients on the elements in the adjacent patch S:

$$\Pi_h(\nabla u_h) = \frac{1}{\sum_{F\in S}|F|}\left(\sum_{F\in S}|F|\ (\nabla u_h)_{|F}\right) \tag{11}$$

In a second step, the same procedure is applied to the P1 field, $\Pi_h(\nabla u_h)$, to recover the Hessian matrix:

$$(G_u)_{ij}(n) = \frac{1}{\sum_{F \in S} |F|} \sum_{F \in S} |F| \left(\frac{\partial}{\partial x_j} \left(\prod_h \frac{\partial u_h}{\partial x_i} \right) \right) \quad (12)$$

For the present application, a combination of the average composition and the norm of the average fluid flow vector are selected. As shown, equation 10, this directional information can be converted into a mesh metric field which prescribes the desired element size and orientation. To combine various variables together to construct metric tensor, the relative bound on the error is considered and the metric tensor is given by an intersection of different metric resulting from the calculation of the Hessian for the different fields [32]. The Gruau and Coupez [34] unstructured and anisotropic mesh generation with adaptation has been used to generate the FE mesh. Additional parameters for this generation are the minimum and maximum mesh size, $l_{F,min}$ and $l_{F,max}$, respectively.

IV.3.6 Resolution.

A complete description of the strategy used to solve the conservation equations with the FE model is given by Bellet et al [4]. The average enthalpy, H, is taken as the primary unknown in the energy conservation (Equation 4). For that purpose, H^l is replaced by its expression as a function of the temperature. The temperature is then eliminated by a first order Taylor's expansion as a function of the average enthalpy. The primary unknown considered in the solute conservation (Equation 5) is the average composition of solute, w. The average liquid composition is eliminated by the introduction a split operator technique with an Euler backward scheme, i.e. the value of w^l is estimated using the value deduced from the previous time step and calculated over the embedded CA microsegregation model [24, 28, 29]. Finally, a combination of the momentum conservation and the total mass conservation offers a set of equations to solve simultaneously the pressure and the average velocity fields.

The computational domain is first created, consisting of a triangular FE mesh with a uniform size. A fixed grid of square CA cells is superimposed on top of the FE mesh. Details of the algorithms built in the CA model and its coupling with the FE model are given elsewhere [29]. Several validations of the coupled CAFE model in purely diffusive regimes for solute and heat have also already been presented [28, 29]. Because the CA model can be seen as an advanced segregation model required for handling mushy zone solidification, it is shortly described hereafter.

IV.3.7 Segregation.

As proposed by Guillemot et al [24], two time–stepping loops are performed. A fixed macro-time step, Δt, is considered to solve the energy, the solute and the momentum equations over the finite element mesh together with a micro time step, δt, adjusted for the CA model calculations. The grid of square cells, with size l_{CA}, is used as the finest spatial discretization to simulate the nucleation, growth, and segregation at the scale of the grains. Among the cells of the CA grid, some are attributed potential nucleation site and a prescribed nucleation undercooling. If one of these cells is still liquid and becomes sufficiently undercooled, i.e. if its undercooling becomes larger than that of its prescribed nucleation site, a new grain can form and grow. A Gaussian distribution is used that characterizes the total density of nuclei, n_{max}, the average nucleation undercooling, ΔT_N, and its standard deviation, ΔT_σ, so as to randomly distribute the nucleation site over the CA grid. A rhombus surface is defined at each cell delimiting its mushy zone. The growth rate of each half diagonal, $\dot{R}^i$ ($1 \leq i \leq 4$), of this quadrilateral surface is calculated as a function of the local supersaturation ahead, $\Omega = (w^{l\,s/l} - w^v)/((1-k)\cdot w^{l\,s/l})$, until they reach a final value, $R^f = \lambda_1/2$, where w^v is the average composition of the cell v. The compositions of the liquid at the dendrite tip solid/liquid interface, $w^{l\,s/l}$, is calculated based on the phase diagram of the binary alloy accounting for the Gibbs-Thomson effect as follows:

$$T_v = T_M + m_L\, w^{l\,s/l} - \frac{2\,\Gamma}{r} \qquad (13)$$

where Γ is the Gibbs–Thomson coefficient defined with respect to the solid phase, r is the radius of curvature at the dendrite tip and T^v is the cell temperature. T_M and m_L are respectively the melting temperature and the liquidus slope defined hereafter. Complete description of the used approach to calculate the growth velocity is given in reference [35].

Upon growth, the grains propagate to neighboring cells as described into details elsewhere [16, 23, 24, 29, 35], each cell being seen as a portion of mushy zone with independent variables to follow the evolution of its fraction of solid and phase compositions.

Because the undercooling associated to the nucleation and growth procedures do modify the solidification path, and because diffusion in the solid and liquid phases needs to be accounted for, an adapted segregation model has been implemented in the CA cell [29]. At each macro time step, Δt, the calculated variation of the energy, ΔH^{n_i}, and composition, Δw^{n_i}, at the nodes of the meshed domain, are interpolated over each cell, ΔH^v and Δw^v. These values are then converted into temperature, T^v, solid volume fraction, $g^{s\,v}$, liquid and solid phases average compositions, $w^{s\,v}$ and $w^{f\,v}$, using a modified version of the microsegregation model developed by Wang and Beckermann [6]. At the scale of each cell, both diffusion in the extradendritic liquid phase and back diffusion in the solid phase are considered, characterized by the diffusion coefficients of lead in liquid and in solid tin, respectively D^l_{Pb} and D^s_{Pb}. The implemented microsegregation model integrates constant value of the primary dendrite arm spacing, λ_1, and the secondary dendrite arm spacing, λ_2.

A linear binary phase diagram is assumed. The value of the liquidus slope, m_L, is computed as function of the value of the eutectic temperature, T_E, the eutectic composition, w_E, the liquidus temperature, T_L, and the nominal lead composition, w_0, using $m_L = (T_E - T_L)/(w_E - w_0)$. Furthermore, the melting temperature, T_M, is calculated using $T_M = T_E - m_L w_E$. In addition, a constant segregation coefficient, k, is assumed. Used values as well as additional required parameters for the CA model are listed in Table 1. Finally, isothermal eutectic transformation is assumed at the eutectic temperature, T_E. Additional description of the coupling approach between the FE and the CA models is given in ref. [29].

IV.4 Results

A 2D Cartesian CAFE simulation has been performed using the parameters listed in Table 1. The temperature histories measured on the two heat exchangers are recorded at positions labeled TL and TR in Figure 1. To account for the heat transfer between the heat exchangers and the smallest vertical surfaces of the alloy, a boundary condition for convective transport between two connected domains are utilized, characterized by a coefficient h. This condition is similar to a heat link with a constant resistance between the alloy and the heat exchangers. The initial simulation time is chosen to correspond to a homogenous isothermal state of the liquid melt, so that the melting process is not modeled. The recorded data shows that the temperature plateau of all thermocouples reaches 1 °C less compared to the holding temperature prescribed after remelting by the experimental procedure, i.e. 250 °C. Consequently, the initial temperature of the domain was set to $T_0 = 249$ °C.

Figure 2 presents the measured and predicted temperature history for the positions defined as T1 to T4 in Figure 1. The temperatures recorded in the heat exchangers are also shown. In Figure 2a the heating step of the right-hand-side heat exchanger is clearly visible. Upon installing the desired global temperature gradient, temperature at T1 to T4 progressively increases while remaining within the range of temperature defined by the heat exchangers. The right-hand-side heat exchanger is then held at around 270 °C and the equidistant thermocouples stabilize to almost equal temperature differences. At 1300 s, cooling of the two heat exchangers starts and the temperature first linearly decrease prior to solidification as shown in Figure 2a. It is only upon solidification, when the temperature becomes lower than the liquidus temperature, $T_L = 219$ °C, that cooling rates start to deviate from that imposed to the heat exchangers. This is made visible in Figure 2b.

In order to retrieve the measured temperatures of the melt during the heating and cooling procedures prior to solidification, values of the heat transfer coefficient, h, thermal conductivity, κ, heat capacity, C_p, and thermal expansion coefficient, β_T, have to be correct. Because all the above listed values are not well assessed by appropriate measurements, some adjustments are necessary. The simulated results shown in Figure 2a and 3a make use of the values listed in Table 1. Figure 2a reveals a very good agreement between the simulated and measured temperature history recorded at thermocouples T1 to T4. It means that the recorded heating, holding and cooling in the fully liquid state are almost perfectly simulated by these thermocouples. Figure 3a shows the temperature distribution map 1000 s after the start of the simulation, i.e. when the left-hand-side and

right-hand-side heat exchangers are hold at a constant temperature above the liquidus of the alloy. The temperature distribution in the 9 cm × 4 cm domain delimited by the thermocouples (black dots in Figure 1) is very well retrieved by the calculation. It is worth noting that, at 1000 s, isotherms are almost vertical. Only a slight inclination in a direction that is typical of a counter clockwise convection loop is measured and simulated. This means that intensity of convection induced by the temperature gradient throughout the entire domain is not sufficient to induce a current that would significantly transport the heat and bend the isotherms as is usual in conventional cavity tests designed for the study of natural convection [36]. However, while this is truly measured by the experimental map shown in Figure 3a, the thermal expansion coefficient has been chosen very small to retrieve this result. The value is rather unreasonable compared with available data in the literature [37]. The reasons for this little effect could either be due to the 2D approximation since convective flow is decreased close to the crucible walls. However, 3D calculations do not support this hypothesis [30, 31]. The other reason could be the existence of an inhomogeneous composition of the melt. In case of layering in the molten state, the average solute composition could be higher at the bottom of the melt, leading to an increase of the melt density from the top to the bottom of the liquid. This would indeed correspond to a stabilizing configuration requiring a stronger convection to mix the bottom high solute layers with the top low solute layers in the fully molten state. No experimental data is yet available to verify such a hypothesis.

Upon further cooling, solidification starts from the left-hand-side of the rectangular cavity. This is clear from Figure 2b since thermocouple T1, only distant by 5 mm from the left-hand-side exchanger, first reaches the liquidus temperature. Upon solidification, sufficient heat is released from the left-hand-side of the ingot to decrease the initially uniform cooling rate imposed to the liquid as can be red on T2 and T3 in Figure 2b. The temperature maps drawn at 2751 s in Figure 3b also reveal that the heat flow is no longer one-dimensional. Instead, the isotherms are inclined as a result of the transport of heat and isotherms are no longer uniformly distributed. The right hand side of the ingot, where convection is expected larger, presents a smaller temperature gradient. Figure 4a presents a map of the average composition and the liquid flow at a similar time. Upon solidification, the liquid is enriched with Pb and generate a buoyancy force caused by the density variation with composition, offering similarities with previous analyses [16, 24, 37]. A 20% variation of the average composition is found with respect to the nominal composition, demonstrating the formation of a severe macrosegregation since the onset of solidification. The liquid flow that forms immediately ahead of the growth front and create a characteristic snake flow in the liquid at the bottom of the rectangular cavity. This means that the liquid flow forms a large “S” form, traveling back and forth from the left-hand-side to the right-hand-side and propagating upward into the melt. Thanks to the small value of the thermal expansion coefficient used in the simulation, it is clear that the natural convection and macrosegregation are mainly induced by the solutal buoyancy forces (β_w is much larger than β_T). It is also of interest in Figure 4a to observe the distribution of the mesh size when a large molten zone remains. As expected, the size of the mesh is not only kept small in the

mushy zone and immediately ahead of the mushy zone where large solutal gradients form, but also follow the liquid velocity field.

The right-hand-side cavity reaches the liquidus temperature and solidification also starts to proceed in its vicinity close to thermocouple T4 at around 3000 s. This takes place prior thermocouples T3 could reach the liquidus temperature. Because T4 is close to the right-hand-side heat exchanger, it cools down more easily than T3 and the cooling curves of the 2 thermocouples consequently cross while still above T_L. Maps in Figure 3c at time 3451 s also reveals this observation. In Figure 4b one can track the development of the macrosegregation associated to the growth of the structure from the right-hand-side of the cavity. The remaining central region of the casting is still liquid. It experiences lead layering. As a consequence, only the top part of the liquid is undercooled and nucleation of new equiaxed grains takes place there. The spots of lower composition isolated into the liquid are indeed the result of the nucleation and growth of solid crystals. Upon solidification, these crystals exchange heat and solute with the free liquid. They consequently contribute to the creation of buoyancy forces in their neighborhood. Again, one can observe the refined mesh surrounding the grains. The mesh oppositely becomes coarser in the left top zone of the mushy zone where no composition gradient exist and the liquid flow is almost nil, as well as in the bottom part of the molten liquid where convection is lower due to a stabilizing layering effect. Freckles are also observed to form on the bottom left part of the ingot, justifying a fine mesh to transport and keep memory of the variations of the average lead composition.

While Figure 2b shows that overall agreement is reached up to about 3600 s, comparison of predictions with the recorded cooling histories reveals large deviations when more solid forms, i.e. when approaching the eutectic temperature, T_E = 183 °C. The temperatures of the predicted cooling curves exhibit a small gradient compared to the recorded data. This is also seen in the temperature map drawn at 4000 s in Figure 3d. The first reason that one could infer to explain the differences is the constant value of the heat transfer coefficient used. Shrinkage takes place upon solidification as the consequence of the density variation between the liquid and the solid state. A gap can then form on each side of the ingot between the solidified layer and the heat exchanger. The formation of this gap is known to drastically decrease the heat transfer, which could be modeled with adequate thermomechanical modeling [38]. This effect is not accounted for in the present model. In addition, the eutectic transformation is assumed isothermal as is clearly seen by the simulated plateaus in Figure 2b at locations T3 and T4. While this is a very common approximation of the segregation models, such plateaus are rarely recorded by thermocouples, except in situation of very low temperature gradient. In fact, extension of a microsegregation model has been proposed by Gandin et al [10] to circumvent this limitation. Its implementation in the CA model is yet not obvious since it would require tracking the nucleation and growth of an undercooled eutectic front.

The measured and predicted final composition map is presented in Figure 5. It is obtained with a spatial resolution using the network of thermocouples schematized in Figure 1. For that purpose, a final unrefinement procedure is applied at the end of the simulation with a prescribed

mesh size equal to 1 cm. The detailed variations of the average compositions that are predicted in Figure 4c are thus rubbed out by the representation in Figure 5. For instance, while freckles are predicted in the final average composition map, they disappear in Figure 5. However, this permits comparison of the predicted segregation map with the experimental one. A pick of positive macrosegregation that reaches 14 wt% lead is well reproduced by the simulation in the bottom part at about one-third of the ingot width from its right-hand-side limit. Comparatively, the intensity of the negative segregation is less but more distributed in the top left part of the ingot. The snapshot at time 3600 s presented in Figure 4c helps to understand the origin of this segregation feature. Upon solidification from the two smallest vertical surfaces, solute accumulates into the liquid in the bottom part of the ingot, forming layers of lead. Because a global temperature gradient is maintained during the entire cooling procedure, the dynamics of the development of the mushy zone from the two smallest vertical surfaces is not symmetric, solidification being delayed from the right-hand-side. In fact, other experiments have showed that the segregation map is perfectly symmetric when the same experiment is conducted with no temperature gradient. The shape of the iso-compositions in Figure 5 yet presents differences between simulation and experiment. The general hill shape is more pronounced in the simulation, the 10 wt% lead iso-composition defining a vertical separation of the ingot, while the negative segregation in the experimental map extends along the entire width at the top of the ingot. The main reason for this difference is believed to be due to the absence of grain sedimentation. In the simulated grain structure, after nucleation in the undercooled liquid, grains remain fixed in space and can only grow. This was already shown in the past as a main limitation if one wishes to compare together grain structure and segregation [16]. However the possibility to handle grain movement is not available in the present model. This explanation is also supported by comparing the simulated grain structure with the experimental macrograph in Figure 6. Simulated grains are very coarse compared to the observations. Modification of the nucleation parameters of the CA model could not significantly decrease the grain size while keeping a columnar zone. This is due to the heat and solute rejected by the grains which prevent activation of available nuclei present into the liquid melt. It is worth noting the orientation of the grains in the last solidified zone of the casting, i.e. the lead rich part of the ingot. Grains grow from the inside of the casting toward the bottom crucible wall, thus forming “V” shape. This shape is also seen on the experimental map. Upon observation of such a grain structure map, one could have thought about columnar grains nucleated at the bottom of the casting and growing inward as is usual for elongated grains. The simulation shows that the opposite actually takes place, explained by the high solute content that delay solidification by drastically changing the supersaturation. In other words, because of solute accumulation, the local liquidus temperature is significantly decreased and further heat extraction is required to solidify the last liquid.

Figure 7 presents the eutectic volume fraction map after complete solidification of the rectangular cavity. This map is strongly correlated to the average lead composition map showed in figure 5. Similar observations have been reported earlier for aluminum copper binary alloy system [10].

IV.5 Conclusions

Achievements within the present contribution are summarized hereafter:

- A solidification experiment of a tin – 10 wt% lead alloy is presented in a rectangular cavity [27]. In-situ temperature measurement is conducted together with composition analyses. The grain structure is also revealed by etching the solidified ingot. Maps of temperature, composition and grain structure are thus available as a benchmark for comparison with simulation.

- A 2D CAFE simulation is presented. Extension of the FE model consists of a refined triangular mesh leading to accurate coupling with the CA model. The CA model integrate a microsegregation treatment that permits to calculate solid and liquid diffusion [28, 29].

- Comparison of the 2D CAFE simulation with the experimental observations is carried out. The predicted temperature curves at regular spatial positions are found to be in good agreement with the measurements up to final development of the mushy zone (Figure 2). Simulation then departs from the measurement, which is expected to be due to inadequate heat transfer in the presence of thermomechanical deformation in the solid state and oversimplified treatment of the eutectic reaction.

- Improvement of both the segregation map and the gain structure map require implementation in the CAFE model of the grain sedimentation. While this was shown to be possible [16], it is not yet compatible with the present microsegregation model built in the CA model. This limitation needs to be overcome.

IV.6 Acknowledgments

This work has been conducted under contracts 15236/02/NL/SH (NEQUISOL) and 14313/01/NL/SH (CETSOL) of the European Space Agency (ESA) Microgravity Applications Promotion (MAP) program. Contribution from J. Blaizot is acknowledged.

IV.7 Reference

[1] Beckermann C. Int. Mater. Rev. 2002; 47:243.

[2] Gandin Ch.-A., Bréchet Y., Rappaz M., Canova G., Ashby M., Shercliff H. Acta Mater. 2002; 50:901.

[3] Ahmad N., Combeau H., Desbiolles J.-L., Jalanti T., Lesoult G., Rappaz J., Rappaz M., Stomp C. Metall. Mater. Trans. A 1998; 29:617.

[4] Bellet M., Fachinotti V.D., Gouttebroze S., Liu W., Combeau H. In *Solidification Processes and Microstructures: A Symposium in Honor of Prof. W. Kurz*, Eds Rappaz M., Beckermann C., Trivedi R. TMS, Warrendale (USA) 2004; 15.

[5] Rappaz M. Int. Mater. Rev. 1989; 34:93.

[6] Wang C. Y., Beckermann C. Metall. Trans. A 1993; 24:2787.

[7] Grong Ø., Dahle A. K., Onsøien M. I., Arnberg L. Acta Mater. 1998; 46:5045.

[8] Nielsen O., Appolaire B., Combeau H., Mo A. Metall. Mater. Trans. A 2001; 32:2049.

[9] Appolaire B., Combeau H., Lesoult G. Mater. Sci. Eng. A 2008; 487:33.

[10] Gandin Ch.-A., Mosbah S., Volkmann Th., Herlach D.M. Acta Mater. 2008; 56:3023.

[11] Heringer R., Gandin Ch.-A., Lesoult G., Henein H. Acta Mater. 2006; 54:4427.

[12] Wang C. Y., Beckermann C. Metall. Mater. Trans. A 1996; 27:2754.

[13] Ludwig A., Wu M. Mater. Sci. Eng. A 2005; 413:109.

[14] A. Ciobanas. Ph. D. Thesis, Institut National Polytechnique de Grenoble (F) 2006.

[15] Martorano M. A., Beckermann C., Gandin Ch.-A. Metall. Mater. Trans. A 2003; 34:1657, 2004; 35:1915.

[16] Guillemot G., Gandin Ch.-A., Combeau H. ISIJ Int. 2006; 46:880.

[17] Combeau H., Zaloznik M., Hans. S., Richy P. E. Metall. Mater. Trans. B 2008; in press.

[18] Yin H., Koster J. N., J. Crystal Growth 1999; 205:590.

[19] Yin H., Koster J. N., J. Alloy Compd. 2003; 352:197.

[20] Mathiesen R. H., Arnberg L. Acta Mater. 2005; 53:947.

[21] Nguyen-Thi H., Reinhart G., Mangelinck-Noël N., Jung H., Billia B., Schenk T., Gastaldi J., Härtwig J., Baruchel J. Metall. Mater. Trans. A 2007; 38:1458.

[22] Könözsy L., Eck S., Kharicha M., Wu M., Ludwig A. In *Solidification and Gravity* 2008; in press.

[23] Gandin Ch.-A., Rappaz M. Acta metall. 1994; 42:2233.

[24] Guillemot G., Gandin Ch. -A., Bellet M. J. Crystal Growth 2007; 303:58.

[25] Hebditch D. J., Hunt J. D. Metall. Trans. 5 (1974) 1557.

[26] Hebditch D. J. Ph. D. Thesis, University of Oxford (U.K.) 1973.

[27] Wang X. D., Petitpas P., Garnier C., Paulin J. P., Fautrelle Y. In *Modeling of Casting, Welding and Advanced Solidification Processes XI*. TMS, Warrendale (USA) 2006; 391.

[28] Mosbah S., Bellet M., Gandin Ch.-A. In *Solidification and Gravity* 2008; in press.

[29] Mosbah S., Gandin. Ch.-A., Bellet. M., Experimental and Numerical Modeling of Segregation in Metallic Alloys, *in preparation*.

[30] Desbiolles J.-L., Thévoz Ph., Rappaz M. In *Modeling of Casting, Welding and Advanced Solidification Processes X*. TMS, Warrendale (USA) 2003; 245.
[31] Gouttebroze S., Bellet M., Combeau H. C. R. Mecanique 2007; 335:269.
[32] Alauzet F., Frey P.J. Institut National de Recherche en Informatique et en Automatique, Research Report 2003; 4759.
[33] Hamide M., Massoni E., Bellet M., Int J. Num. Meth. Eng. 2008; 73:624.
[34] Gruau C., Coupez T., Comp. Meth. Appl. Mech. Eng. 2005; 194:4951.
[35] Ch.-A. Gandin, G. Guillemot, B. Appolaire, N. T. Niane, Mater. Sci. Engng A342 (2003); 44:50.
[36] De Vahl Davis G. Int. J. Num. Meth. in Fluids 3 (1983); 249:255.
[37] Quillet G., Ciobanas A., Lehmann P., Fautrelle Y. Int. J. Heat Mass Trans. 2007; 50:654.
[38] M. Bellet, O. Jaouen, I. Poitrault. Int. J. Num. Meth. Heat Fluid Flow 15 (2005); 120:142.

IV.8 Figures

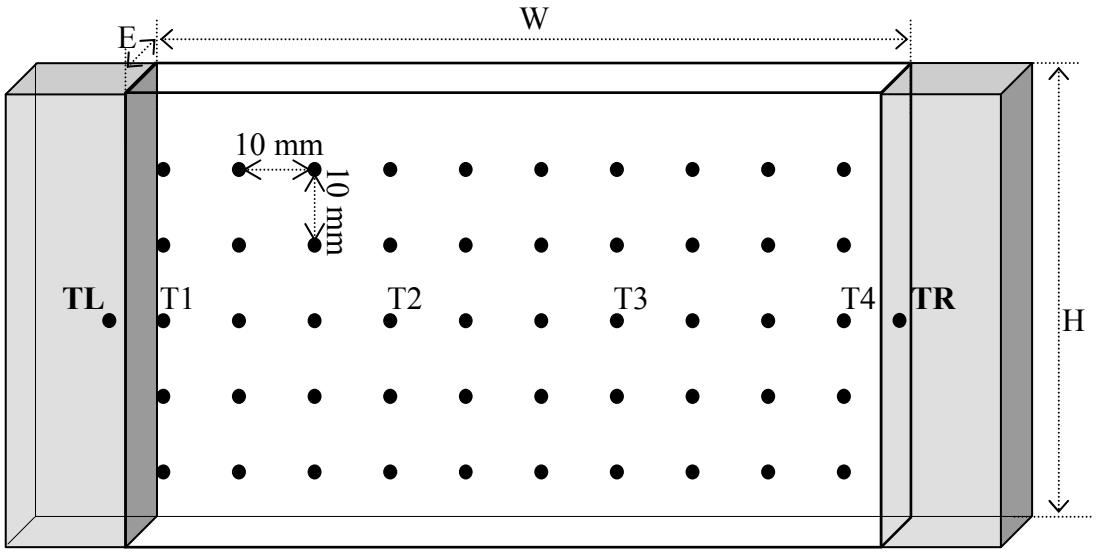

Figure 1 Schematic view of the casting geometry. A tin - 10 wt% lead alloy is solidified in a H = 6 cm height × W = 10 cm width × E = 1 cm thick rectangular cavity. The cooling /heating of the ingot is controlled by two heat exchangers are placed in contact with the two opposite smallest vertical surfaces. Fifty thermocouples, marked by black dots, are embedded in the crucible to record the temperature during the experiment. Each one is distant from its neighbor by 10 mm in both the vertical and horizontal directions, thus enabling the construction of instantaneous temperature maps. Temperatures are also recorded in the left-hand-side and right-hand-side heat exchangers at positions labeled TL and TR, respectively.

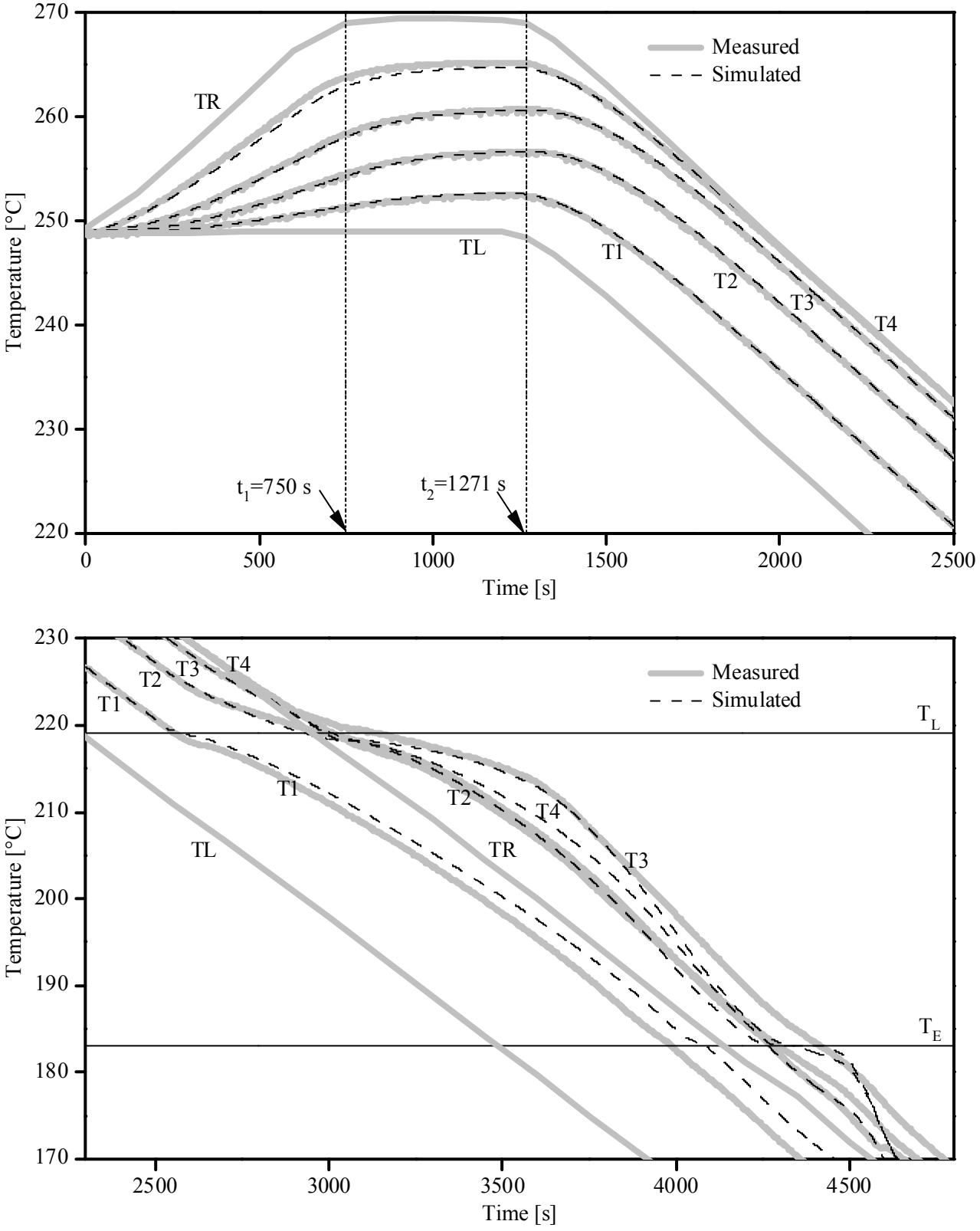

Figure 2 Measured (grey) and predicted (black) temperature histories at positions T1 to T4 and temperature histories TL and TR of the heat exchangers (positions showed in Figure 1). From an isothermal liquid state (249 °C), the right-hand-side part of the system is first heated (0.02 °C s^{-1}) to settle a 200 °C m^{-1} temperature gradient. A constant cooling rate (-0.03 °C s^{-1}) of the heat exchangers is then prescribed from 1300 s up to completion of the solidification of the tin - 10 wt% lead alloy.

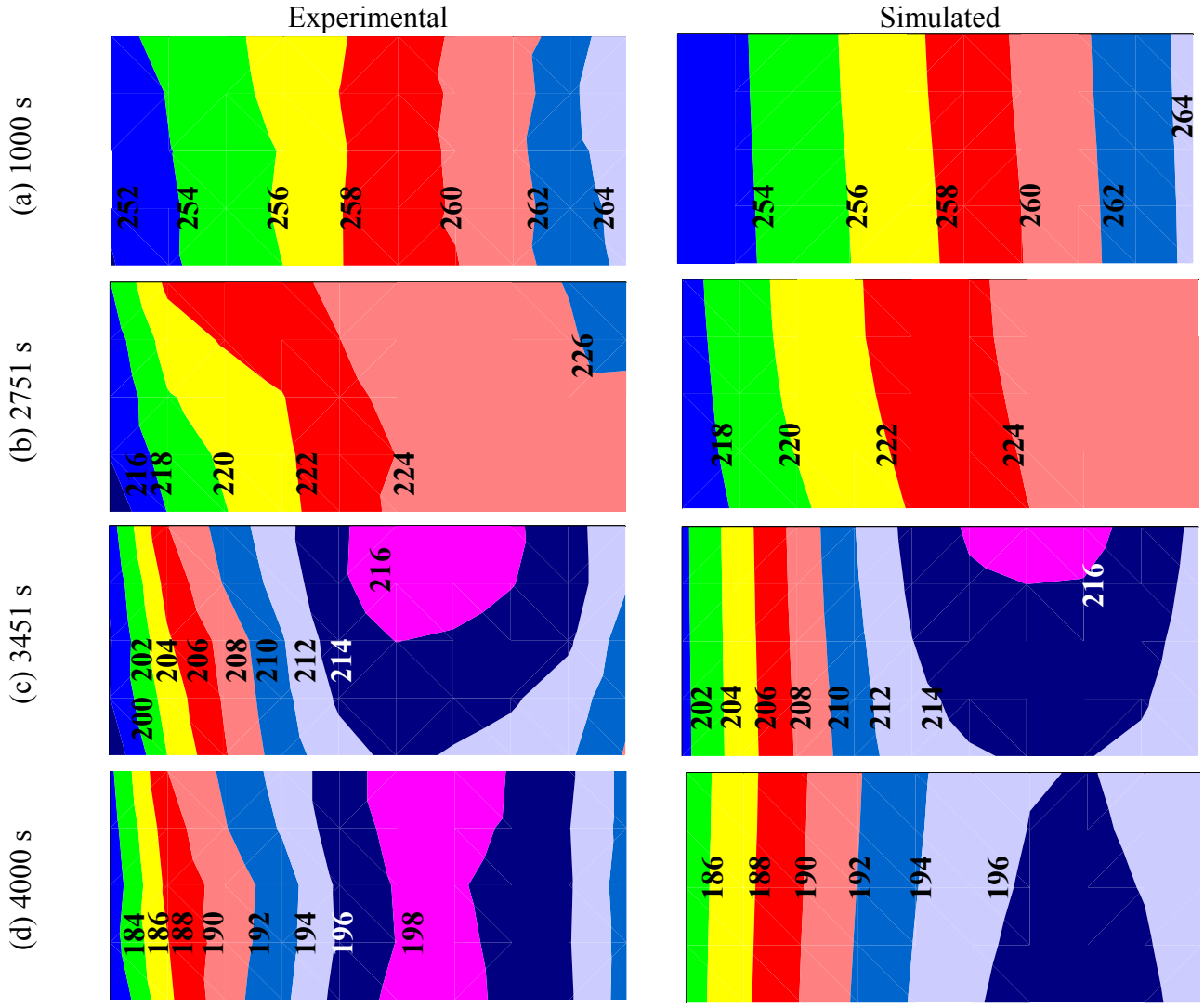

Figure 3. (left) measured and (right) simulated temperature maps at time (a) 1000s, (b) 2751 s, (c) 3451 s and (d) 4000 s during the experiment of a tin - 10 wt% lead alloy. The size of the rectangular domain is only 9 cm × 4 cm, i.e. the size of the grid of thermocouples schematized in Figure 1. Labels unit is in °C.

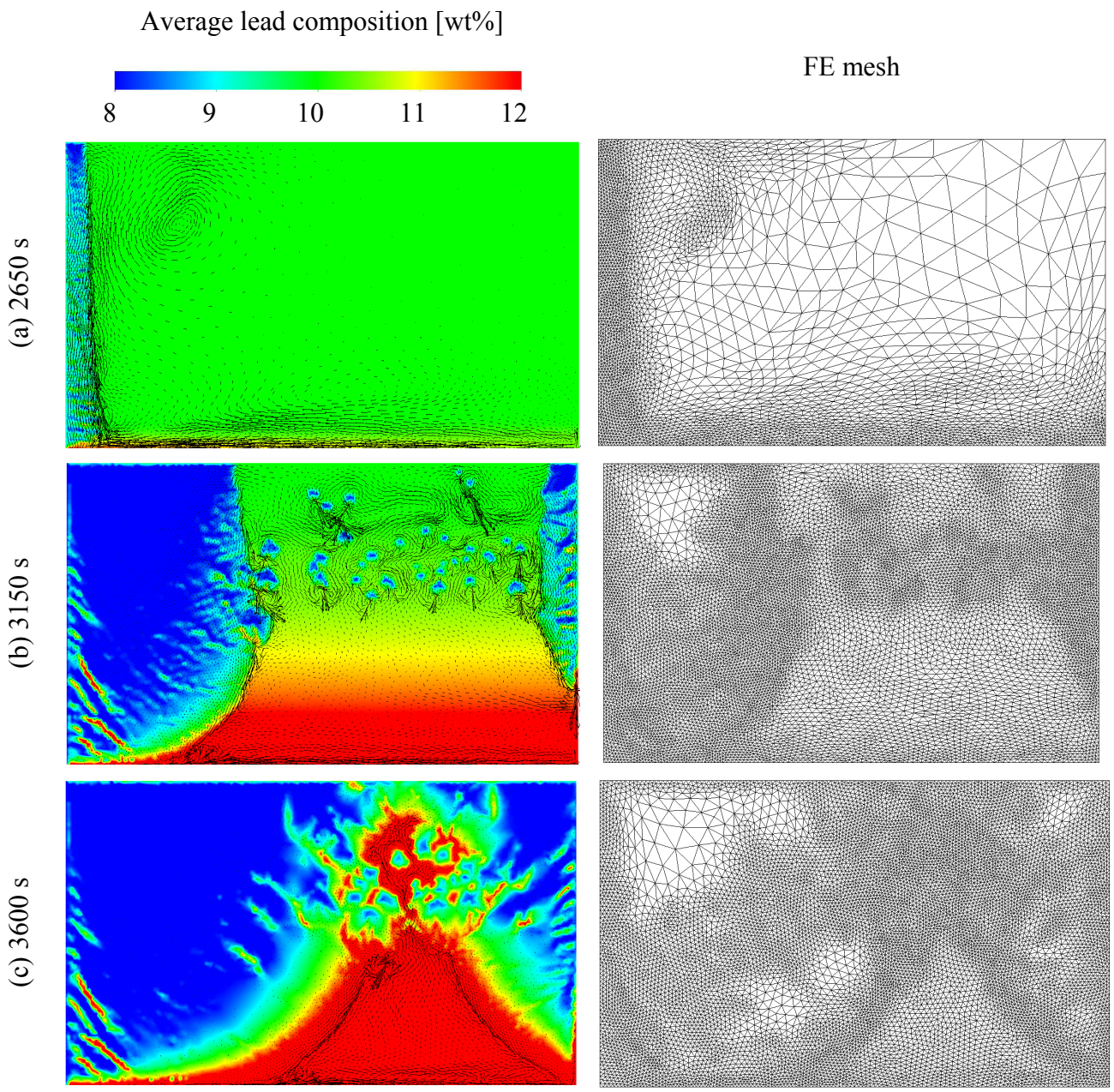

Figure 4 Prediction of the 2D CAFE model for the rectangular cavity tin - 10 wt% lead alloy solidification experiment. The average lead composition is drawn on the left-hand-side together with the fluid flow velocity vectors at times (a) 2650 s, (b) 3150 s and (c) 3600 s.

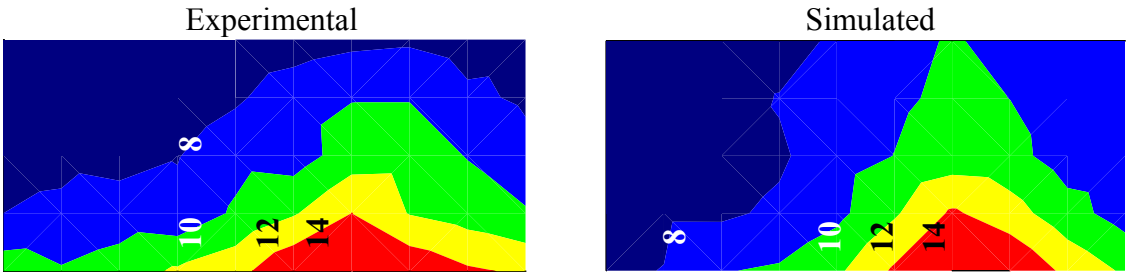

Figure 5. Final average lead composition (left) measured and (right) simulated in the tin - 10 wt% lead alloy experiment. Measurements are conducted at the same location as the thermocouples shown in Figure 1. The size of the above rectangular domain is consequently 9 cm × 4 cm. Labels unit is in wt% lead.

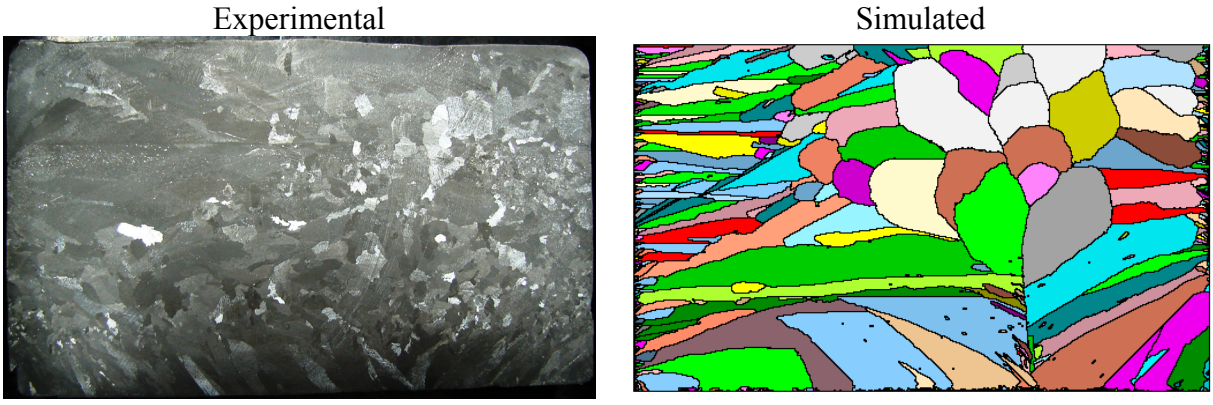

Figure 6. Solidification grain structure of the tin - 10 wt% lead alloy experiment (left) as observed at the surface of the casting and (right) simulated. The rectangular cavity casting is 6 cm height × 10 cm width.

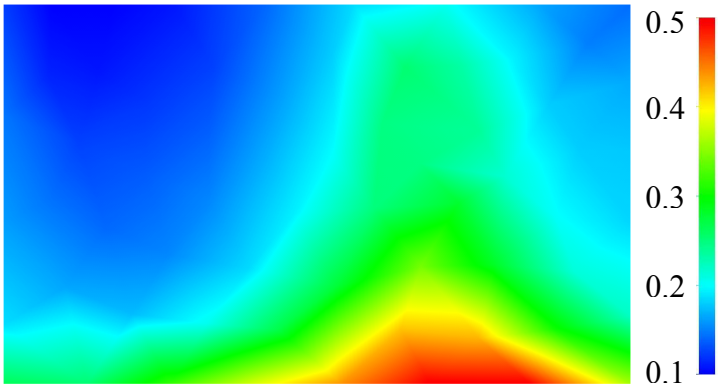

Figure 7. Predicted volume fraction of eutectic after completion of the solidification leading to the grain structure presented in Figure 6.

IV. 9 Table

Material properties of the tin – 10 wt% lead alloy		
Latent heat of fusion, $\Delta_s^l H_f$	J kg^{-1}	$3 \cdot 10^4$
Heat capacity, C_p	J kg^{-1} °C^{-1}	260
Temperature dependent conductivity, T, κ	°C, W m^{-1} °C^{-1}	183, 50
		219, 20
Nominal lead composition, w_0	wt%	10
Melting temperature, T_M	°C	232
Eutectic temperature, T_E	°C	183
Liquidus slope of the, m_L	°C $wt\%^{-1}$	-1.294
Segregation coefficient, k	-	0.09
Eutectic composition, w_E	wt%	37.87
Density, ρ_0	kg m^{-3}	7371
Thermal expansion coefficient, β_T	°C^{-1}	$8\ 10^{-9}$
Solute expansion coefficient, β_w	$wt\%^{-1}$	$-5 \cdot 10^{-3}$
Dynamic viscosity, μ	Pa s	10^{-3}
Primary dendrite arm spacing, λ_1	m	$1.5 \cdot 10^{-3}$
Secondary dendrite arm spacing, λ_2	m	10^{-4}
Diffusion coeff. (lead in liquid tin), D_{Pb}^l	m^2 s^{-1}	$4.5 \cdot 10^{-9}$
Diffusion coeff. (lead in solid tin), D_{Pb}^s	m^2 s^{-1}	$5 \cdot 10^{-13}$
Gibbs-Thomson coefficient, Γ	°C m	$5.68\ 10^{-8}$
Gaussian parameters for nucleation		
Average nucleation undercooling, ΔT_m	°C	1.2
Standard deviation of the nucleation undercooling, ΔT_σ	°C	0.2
Total density of nuclei, n_{max}	m^{-3}	$5 \cdot 10^8$
Simulation parameters		
Initial temperature, T_0	°C	249
Heat transfer coefficient, h	W m^{-2} °C^{-1}	820.
Time step, Δt	s	0.5
Error on lead composition, E_w	-	$2 \cdot 10^{-4}$
Error on the norm of the flow velocity, E_v	-	$5 \cdot 10^{-4}$
Minimum mesh size, $l_{F,min}$	m	$5 \cdot 10^{-4}$
Maximum mesh size, $l_{F,max}$	m	10^{-2}
Cell size, l_{CA}	m	$2 \cdot 10^{-4}$

Table 1: Value of material properties and simulation parameters.

General conclusion and perspective

The presented achievements could be classified into two complementary parts which have been developed jointly: experimental and advanced numerical models for the study of solidification in metallic alloys. The numerical models have been developed, validated and applied in this contribution. The results could be summarized as follows:

- ***Experimental achievements***

The containerless electromagnetic levitation technique developed by Herlach et al. [Herl93, Herl04] for the study of solidification structures and induced segregation has been successfully applied. Al-Cu alloy spherical systems with typically 2.6510^{-3} m radius have been processed. Three copper compositions have been selected, 4, 14 and 24wt%. For each composition, samples, maintained upon electromagnetic levitation, have been solidified with and without initiating the nucleation of the primary solid phase. To trigger the nucleation of the primary solid phase, an alumina plate has been used. The non equilibrium temperature has been recorded using an optical pyrometer during all the solidification time. In addition, characterization consisting in the average composition, the eutectic volume fraction and the dendrite arm spacing maps have been processed over a cutting meridian plan for all the samples. Strong correlations have been found between the composition, the eutectic and the dendrite arm spacing maps for samples where nucleation was spontaneous. Besides, important nucleation undercooling for the primary and the eutectic structure have been measured. Spatial averaging has been used to calculate the composition, the volumetric amount of eutectic and the dendrite arm spacing averaged values over a cutting meridian plan. Deviations from the nominal composition are found and explained as due to the non symmetric growth of the grain structures. In addition, the averaged eutectic volume fractions were found to be lower than the Gulliver-Scheil [Kur98] model prediction when increasing the eutectic structure undercooling. For the triggered samples, the recorded cooling curves showed an important increase of the cooling rate and a shorter solidification time. Moreover, the copper maps exhibit less deviation from the nominal value than for samples with spontaneous nucleation. Finest structure is measured around the nucleation point where the highest amount of eutectic is also measured. The two experimental approaches, with and without triggering of the primary phase nucleation, offer a good reference base for further modeling validations.

- ***Numerical achievements***

Volume averaging technique has been used to develop a semi–analytical model for the prediction of both the primary and the eutectic structures growth and final phase's volume fraction for the equiaxed and the columnar structure. This model has been applied to simulate the solidification of the Al-Cu alloy samples where the nucleation occurs spontaneously upon electromagnetic levitation. Parametric study of the model predictions as a function of the primary and the eutectic

structures as well as back diffusion in the solid phase has been conducted. The eutectic recalescence has been found to be the most important parameter controlling phase's volume fractions in the presence of high eutectic structure nucleation undercooling.

A coupled Cellular Automaton (CA) – Finite Element (FE) model has been developed with the following improvements:

- ✓ Advanced microsegregation modeling embedded for each CA cell. The model is an extension of the Wang and Beckermann work [Wan93.1, Wan93.2]. It takes into account both the mushy zone front undercooling and back diffusion in the solid phase. Interpolated average enthalpy and composition variations from the finite element mesh are used to calculate the temperature, solid volume fraction and composition of the solid and the liquid phases.

- ✓ Mesh adaptation technique based on a geometrical error estimator. This technique is implemented in the finite element model and allows calculating at each time step the required mesh orientation and size to solve the macroscopic conservation equations with enhanced accuracy. In addition, it allows the tracking of the mushy zone front and the solute and thermal profiles created ahead.

- ✓ New coupling scheme between the finite element and the cellular automaton models is implemented to allow the adaptation of the finite element mesh. In addition, a new method for the calculation of the mushy zone growth is developed. This method is an extension of the approach proposed by Guillemot et al. [Gui04] with the advantage of the integration of dendritic structure characteristic dimensions.

These numerical models have been validated and applied for the experiments described earlier. The CAFE model has been also applied for the prediction of the temperature field, macrosegregation and fluid flow in the Wang et al. experiments [Wang06]. The main drawback of this work is the identification of a new physical parameter, which is the eutectic recalescence, as a key parameter in the prediction of final phase's volume fractions. This has been conducted using the new multiscale analytical model and completed with the present CAFE model. In addition, the new CAFE model has been successfully proven as an efficient tool for the study of segregation at the scale of grain structures, meso and microsegregation, as well as at the typical ingot scale, macrosegregation.

Finally, the presented experimental setup would provide additional and accurate experimental data with the following specification added to their scope statements:

For the electromagnetic levitation setup:

- Using advanced temperature measurement technology to increase the accuracy for the whole spherical sample using infrared high speed cameras. A 3D temperature field over the sample could be then extracted from the measurement by stereoscopy technique. This also could be used to identify the nucleation point and track the mushy zone front growth. Such experimental data is of a great importance for further modeling and validation.

- Applying the same approach to process metallic binary alloys system in reduced gravity condition. As demonstrated elsewhere [Beck02], natural convection plays an important role in the final segregation pattern and the growth of the dendritic structure. Comparison between 1g and micro-gravity conditions would provide excellent means to quantitatively investigate the effect of fluid flow driven by buoyancy convection forces on the solidified microstructure.

For the rectangular cavity setup:

- In situ X-ray analysis over the largest lateral section of the rectangular sample to track the nucleation and the growth of the grain structure. This technique completed with advanced image analysis could also be used to have the time variation of the average composition of the solute as well as to track the mushy zone front and the grains movements.

Although the presented numerical model takes into account important physical parameters, several phenomena are not yet included and thus this contribution could be completed by:

- Taking into consideration the grain movements coupled with fluid flow. This has been already integrated in the CAFE model developed by Guillemot et al. [Gui04]. Detailed description of the strategy used to simulate the movement of the grain structure is presented in [Gui04]. However, the approach has to deal with incomplete diffusion in the solid and the liquid phases.

- Thermo-mechanical calculations. Thermal contraction and solidification shrinkage as well as median cat deformation are usually observed in industrial casting process [Fle67]. These phenomena have been neglected based on constant and equal densities of the solid and the liquid phases. Volume contraction has been observed in as-cast state for the rectangular Sn-10wt%Pb sample processed using the rectangular cavity

setup. This could be one of the main reasons for the deviation of the model predictions from the experimental measurements as explained in chapter III.

- Physical properties. Taking into consideration the variations of the heat capacity, real phase diagram, and other thermodynamics properties of the simulated materials. In this contribution, we have assumed constant value for the thermodynamic properties as well as constant values for the liquidus slope, partition ratio, etc. Coupling the developed models with calculation of these variables as function of the temperature, local composition, etc., is expected to improve the model predictions.

- Integrating additional structures within the CA model. The eutectic and the peritectic grains growth could be simulated using an equivalent approach to that used for the prediction of the dendritic grain structure. The non-equilibrium growth could thus be considered in the CAFE model. Hence with the integration of the nucleation, undercooling and growth of each structure, consequences on grains shape, competitions and evolutions could be numerically studied and compared to the available experimental data.

- 3D modeling. Resolution of the solute and thermal field in 3D would provide more realistic solutions via the finite element approach and hence best approximation of the grain structure using a 3D cellular automaton. Advanced memory management algorithm together with the presented mesh adaptation technique could be used to reduce the required memory and computational resources.

References

[App07] B. Appolaire, H. Combeau, G. Lessoult. Modeling of equiaxed growth in multicomponent alloys accounting for convection and for the globular/dendritic morphological transition. Material Science and Engineering, A 487, 2008;33–45.

[Ana91] R. Ananth, W.N. Gill. Self-consistent theory of dendritic growth with convection. J. Cryst. Growth, Vol. 108, 1991;173–189, cited by [Gui04].

[Badi07.1] A. Badillo, D. Ceynar, C. Beckermann. Growth of equiaxed dendritic crystals settling in an undercooled melt, Part 1: Tip kinetics. Journal of Crystal Growth, 309, 2007;197–215.

[Badi07.2] A. Badillo, D. Ceynar, C. Beckermann. Growth of equiaxed dendritic crystals settling in an undercooled melt, Internal solid fraction. Journal of Crystal Growth 309 (2007) 216–224.

[Beck02] C. Beckermann. Modelling of Macrosegregation: Applications and Future Needs, Int. Mater. Rev., 47, 2002; 243–261.

[Bro66] H.D. Brody and M.C. Flemings. Solute Redistribution in Dendritic Solidification, Trans. Metall. Soc. AIME, Vol. 236, 1966; 615.

[Dav83] De Vahl Davis G. Natural convection of air in a square cavity: a bench mark numerical solution. Int. J. Num. Meth. in Fluids 3, 1983; 249–255.

[Fle67] M. C. Flemings and G. E. Nereo. Macrosegregation: Part I. Transaction of the metallurgical society of Aime, 239, 1967; 1449–1461.

[Gan94] Ch.-A. Gandin and M. Rappaz. A Coupled Finite Element–Cellular Automaton Model for the Prediction of Dendritic Grain Structures in Solidification Processes. Acta Metall. Mater., Vol. 42, N° 7, 1994; 2233–2246.

[Gan95] Ch.-A. Gandin. Modélisation stochastique de la solidification: formation de structures de grains dendritiques. Thèse N° 1322, Ecole Polytechnique Fédérale de Lausanne, Suisse, 1995.

[Gan00.1] Ch.-A. Gandin. From Constrained to Unconstrained Growth During Directional Solidification. Acta Mater., Vol. 48, N°10, 2000; 2483–2501

[Gan00.2] Ch.-A. Gandin. Experimental Study of the Transition from Constrained to Unconstrained Growth during Directional Solidification. ISIJ Int., Vol. 40, N°10, 2000; 971–979

[Gan03] Ch. A. Gandin. G. Guillemot, B. Appolaire, N. T. Niane. Boundary layer correlation for dendrite tip growth with fluid flow. Material Science and Engineering, A342, 2003; 44–50.

[Gan08] Ch.-A Gandin, Mosbah S., Th. Volkmann, D.M. Herlach. Experimental and numerical modeling of equiaxed solidification in metallic alloys. Acta Materialia, 56, 2008; 3023–3035.

[Ger02] S. Gérardin. Etude expérimentale de la croissance libre de cristaux équiaxes en mouvement. Thèse de doctorat de l'INPL, 2002.

[Gui03] G. Guillemot, Ch.-A. Gandin, H. Combeau et R. Heringer, New Coupling Scheme for a Heat Flow Cellular Automaton - Finite Element Model Applied to Alloy Solidification, Proceedings of the 2003 International Symposium on Liquid Metal Processing and Casting, Nancy, France, 2003.

[Gui04] G. Guillemot. Rapport de Thèse. Formation des structures de grains dans les alliages a solidification dendritique-Modélisation couplée automates cellulaires et éléments finis. Institut national polytechnique de lorraine, Nancy, FR, 2004.

[Gui06] G. Guillemot, Ch.-A. Gandin, H. Combeau. Modeling of macrosegregation and solidification grain structures with a coupled cellular automaton - Finite element model. ISIJ International 46, 2006;880–895.

[Her02] R. Heringer, Ch-A. Gandin, and G. Lesoult. Modélisation numérique de la solidification de gouttelettes métalliques surfondues. Matériaux, 2002.

[Her04] R. Heringer. , Ph. D. Thesis, Institut national polytechnique de lorraine, Nancy, FR, 2004.

[Her06] R. Heringer, Ch-A. Gandin, G. Lesoult, and H. Henein. Atomized droplet solidification as an equiaxed growth model. Acta Metall, 54, 2006;4427–4440.

[Herl93] D. M. Herlach, R. F. Cochrane, I. Egry, H. J. Fecht and A. L. Greer. Containerless Processing in the Study of Metallic Melts and Their Solidification. Int. Mater. Rev., 38, 1993; 273–347.

[Herl04] Herlach D., Gandin Ch.-A., Garcia-Escorial A., and Henein H.. Application for continuation of the MAP-Project : A98/99-023, 2004.

[Kar98] A. Karma. Model of grain refinement in solidification of undercooled melts. International Journal of Non-Equilibrium Processing, 11, 1998; 201–233.

[Kas08] G. Kasperovich, T. Volkmann, L. Ratke, and D. Herlach. Microsegregation during Solidification of an Al-Cu Binary Alloy at Largely Different Cooling Rates (0.01 to 20,000 K/s):Modeling and Experimental Study. Metallurigical And Material Transactions , 39A, 2008;1183–1191.

[Kur98] W. Kurz and D.J. Fisher. Fundamentals of solidification. Trans Tech Publications Ltd, Zurich, CH 1998.

[Lan77] J.S. Langer et H. Müller-Krumbhaar. Stability effects in dendritic crystal growth, J.Cryst. Growth, Vol. 42, 1977; 11–14.

[Les86] G. Lesoult, Cristallisation et microstructures, Solidification, Techniques de l'ingénieur, M 58, 1986, pp. 1–28

[Lev82.1] C. G. Levi and R. Mehrabian. Microstructures of rapidly solidified aluminium alloy submicron powders. Metallurgical transactions, 13A, 1982; 13–23.

[Lev82.2] C. G. Levi and R. Mehrabian. Heat Flow during Rapid Solidification of Undercooled Metal Droplets. Metallurgical transactionn, 13A, 1982; 221–234.

[Liu05] W. Liu, Finite element modelling of macrosegregation and thermomechanical phenomena in solidification processes, Ph. D. Thesis, Ecole Nationale Supérieure des Mines de Paris, Paris, France (2005).

[Mar03] M.A. Martorano, C. Beckermann, and Ch.-A. Gandin, A Solutal-Interaction Mechanism for the Columnar-to-Equiaxed Transition in Alloy Solidification, Metall. Mater. Trans. A, Vol. 34A, 2003; 1657–1674.

[Mik69] E.S. Miksch, Solidification of Ice Dendrites in Flowing Supercooled Water, Trans. Metall. Soc. AIME, Vol. 245, 1969; 2069–2072, cited by [Gui04].

[Old66] W. Oldfield, A Quantitative Approach to Casting Solidification : Freezing of Cast Iron, Transactions of the ASM, Vol. 59, 1966; 945–961.

[Pap35] A. Papapetrou, Zeitschrift für Kristallographie 92, 1935; 89 cited by [Kur98].

[Pra] A. Prasad, H. Henein, E. Maire, and Ch-A. Gandin. Understanding the rapid solidification of Al-4.3Cu and Al-17Cu using X-Ray tomography. Metallurgical and Materials transaction, A. *in press*.

[Pra05] A. Prasad, H. Henein, and Ch-A. Gandin. Microsegregation modelling of rapidly solidified Al-Cu droplet. 2005. Communication personnelle.

[Rap87.1] M. Rappaz and PH. Thévoz. Solute diffusion model for equiaxed dendritic growth. Acta Metall 35, N° 7, 1987; 1487–1497.

[Rap87.2] M. Rappaz and PH. Thévoz. Solute diffusion model for equiaxed dendritic growth: analytical Solution. Acta Metall, 35, N°12, 1987; 2929–2933.

[Rap89] M. Rappaz. Modelling of microstructure formation in solidification processes, Int. Mater. Rev., 34, 1989;2193–123.

[Sar86] J. A. Sarreal. G. J. Abbaschian, Metallurgical Transactions A, 1986;17–2063.

[Soh97] H. Y. Sohn. R&D in the metallurgical industry toward the 21st century. Journal of the Minerals, Metals and Materials Society, 49, 1997; 33–37

[Spi06] J. A. Spittle. Columnar to equiaxed grain transition in as solidified alloys. Int. Mat. Reviews, Volume 51, Number 4, August 2006; 247–269.

[Wan93.1] C. Y. Wang, C. Beckermann. A unified solute diffusion model for columnar and equiaxed dendritic alloy solidification. Materials Science and Engineering, A171, 1993; 199–211.

[Wan93.2] C. Y. Wang, C. Beckermann. A multiphase solute diffusion model for dendritic alloy solidification. Metallurigical transactions ,24A, 1993; 2787–2802.

[Wan96.1] C.Y. Wang, C. Beckermann, Equiaxed dendritic Solidification with Convection : Part I.Multiscale / Multiphase Modeling, Metall. Mater. Trans., Vol. 27 A, 1996; 2754–2764

[Wan96.2] C.Y. Wang, C. Beckermann, Equiaxed dendritic Solidification with Convection :Part II. Numerical Simulations for an Al-4 Wt Pct Cu Alloy, Metall. Mater. Trans.,Vol. 27 A, 1996; 2765–2783

[Wang06] Wang X. D., Petitpas P., Garnier C., Paulin J. P., Fautrelle Y., in Modeling of Casting, Welding and Advanced Solidification Processes XI, TMS, Warrendale, PA, USA (2006).

Abstract

This work first presents a new multi-scale modeling approach of grain structures solidification and its associated segregation pattern in the as-cast state. It is based upon a semi-analytical description of the chemical length scales built in the solid and outside the envelope of the grains. Originality lies in the account of both the primary and the eutectic structure nucleation undercooling. The model has been applied for Al–Cu sample with spontaneous nucleation processed by the Electromagnetic Levitation (EML) technique. The EML technique is used as an experimental model to process Aluminum–Copper spherical samples with different copper compositions. For each sample, nucleation has been either spontaneous or triggered using an alumina plate. Various degrees of undercooling have been measured prior to the primary and the eutectic structure nucleation events. Extensive metallurgical characterizations have been performed over a median cutting plane for each sample using a scanning electron microscope (SEM) equipped with energy–dispersive X-ray spectrometry and analyses of SEM images. A complete set of data has been elaborated consisting of the distribution maps drawn for the average copper composition, the volume fraction of the eutectic structure, the dendrite arm spacing and their averaged values over the same cutting plane. Segregation has been measured and found to be strongly correlated with the eutectic and the dendrite arm spacing maps. Application of the model shows that the nucleation undercooling of the eutectic structure is a key parameter for a quantitative prediction of the fraction of phases in the solidified samples.

In addition, a two-dimensional Cellular Automaton–Finite Element (2D CAFE) model is developed to investigate the segregation maps and the non-equilibrium temperature evolution for samples with spontaneous and triggered nucleation. The model integrates the microsegregation model in each CA cell taking into account the primary phase nucleation undercooling and back diffusion in the solid phase. Additional microstructural features considered are the primary and the secondary dendrite arm spacing. Heat, mass and momentum conservation equations over the simulation domain are solved using the finite element model. A new coupling scheme between the finite element and the cellular automaton model is developed allowing finite element mesh adaptation. A geometrical error estimator has been integrated in the finite element model to control the mesh size and orientation in order to increase the accuracy of the finite element solution. New interpretations of the experimental observations are accessible thanks to the new 2D CAFE model.

The 2D CAFE model is also successfully applied to a benchmark solidification test developed recently for a rectangular cavity experiment. Comparisons with maps of temperature, macrosegregation and grains structures have been performed demonstrating the model capabilities to deal with heat and mass exchanges at micro and macro scales.

Keywords: solidification, segregation, EML, dendritic growth, eutectic growth, structure, equiaxed, columnar, heterogeneous nucleation, modeling, cellular automaton, finite element, CAFE, remeshing.

Résumé

Ce travail présente deux approches pour la modélisation des structures de grains et de la ségrégation chimique associée à l'état de fonderie après solidification.

La première approche est de développer un modèle basé sur une description semi analytique des couches de diffusion chimique dans la phase solide et à l'extérieur des enveloppes des grains. L'originalité de ce modèle réside dans la prise en compte de la surfusion de germination des structures dendritique et eutectique. Nous avons appliqué le modèle développé aux gouttes solidifiées par lévitation électromagnétique (EML) et dont la germination de la structure primaire s'est produite spontanément. La technique EML est utilisée comme modèle expérimental pour produire des échantillons sphériques d'alliage aluminium–cuivre (Al–Cu) à différentes compositions nominales de cuivre. Pour chaque échantillon, nous avons étudié le cas d'une germination spontanée et le cas d'une germination déclenchée. Plusieurs degrés de surfusion ont été mesurés avant la germination des structures dendritique et eutectique. Des investigations expérimentales ont été menées pour caractériser une section centrale de chaque échantillon. Un microscope électronique à balayage (MEB), équipé d'un capteur rayon X, a été utilise pour l'analyse dispersive en énergie. Un ensemble complet de données a été généré pour chaque échantillon a travers des cartes de distribution du cuivre, de la structure eutectique et de l'espacement interdendritique secondaire. Le modèle permet une prédiction quantitative de la fraction de structure eutectique en accord avec les mesures effectuées et cela grâce à la prise en compte de la surfusion de germination eutectique. L'accord avec les mesures expérimentales est dû à la prise en compte de l'effet de la surfusion et de la recalescence eutectique.

Dans la seconde approche, un modèle numérique 2D couplant Automate Cellulaire (CA) – Eléments Finis (FE) est développé pour la prédiction de la variation de la température et des cartes de ségrégation mesurées pour les échantillons Al–Cu. Un modèle de microségrégation a été intégré dans chaque cellule de l'automate. Ce modèle permet de prendre en compte la surfusion de la germination de la phase primaire ainsi que la diffusion du soluté dans la phase solide. Les longueurs caractéristiques de diffusion ont été exprimées en fonction des espacements interdendritiques primaires et secondaires. Les équations de conservation d'énergie, de masse et de quantité de mouvement sont résolues par la méthode des éléments finis. Un nouveau schéma de couplage entre l'automate cellulaire et les éléments finis a été développé pour permettre l'adaptation du maillage. Un estimateur d'erreur géométrique a été intégré pour le contrôle de la taille et l'orientation des mailles afin d'optimiser la résolution par la méthode des éléments finis. L'application du modèle 2D CAFE a permis une compréhension avancée des résultats expérimentaux. Ce modèle a aussi été appliqué à la solidification d'une cavité rectangulaire d'un alliage étain−plomb.

Les capacités du modèle pour l'étude des transferts d'énergie et de masse aux échelles micro et macro ont été mise en évidence par le bon accord entre ces perditions et les mesures expérimentales (des cartes de température, de la macroségrégation et des structures de grains).

Mots clés : solidification, ségrégation, EML, croissance dendritique, croissance eutectique, structure, équiaxe, colonnaire, germination hétérogène, modélisation, automates cellulaires, éléments finis, CAFE, remaillage.